NONLINEAR INTERFACIAL WAVES IN TWO-PHASE FLOW

BY

BEVERLEY ANNE NASH

WOLFSON COLLEGE

Thesis submitted for the Degree of
Doctor of Philosophy at Oxford University

September 1980

CONTENTS

Page

NONLINEAR INTERFACIAL WAVES IN TWO-PHASE FLOW

by

BEVERLEY ANNE NASH, WOLFSON COLLEGE

Thesis submitted for the Degree of Doctor of Philosophy at Oxford University, Trinity Term 1980

ABSTRACT

Large amplitude interfacial waves are an important feature of annular gas-liquid two-phase flow. They act as a source of entrainment for liquid droplets. They occur for liquid flow rates above a critical value which depends on the gas flow rate.

This thesis examines the formulation of a mathematical model to describe the behaviour of these nonlinear waves. Attention is focussed on the case of vertical upwards flow with reference to the experimental conditions for the rig at AERE Harwell.

A comprehensive account is given of the limitations and similarities of mathematical models proposed by earlier research workers and their applicability to vertical two-phase flow. The most suitable approaches are found to be kinematic wave theory and an integral method.

Experiments have been carried out at AERE Harwell to determine the relationship between liquid flux and film thickness required by kinematic wave theory and also to test some of the theory's predictions.

There is a discussion of the difficulties involved in modelling the stresses exerted by the turbulent gas core on disturbance waves. The applicability of Benjamin's 'quasi-laminar' theory is considered.

A linear stability analysis indicates that the interface is always unstable. The linear theory cannot provide a criterion for disturbance wave inception. Alternative explanations for wave inception are suggested.

The SMAC (Simplified Marker And Cell) numerical method has been developed to model the time dependent behaviour of large amplitude waves in vertical annular two-phase flow.

Finally, it is proposed that any realistic mathematical model for disturbance waves should be based upon kinematic wave theory and should take account of wave-breaking.

Acknowledgements

I should like to thank my supervisor, Dr. J. Rae, for his help and encouragement.

I am also very grateful to members of Engineering Sciences Division, AERE Harwell, especially Miss G. Freeman, for their help with the experiments.

Financial support was provided in the form of a CASE studentship by the Science Research Council in conjunction with the United Kingdom Atomic Energy Authority.

Finally I should also like to thank Mrs. Joan Lyon for typing this thesis with such care and patience.

CHAPTER 1. Introduction

Gas-liquid two-phase flow exists in a large range of industrial plant including evaporators, boilers, distillation towers, chemical reactors, condensers and turbines. Despite its technological importance, the state of knowledge of two-phase flow is not well advanced. The very complex nature of the gas-liquid interface means that a mathematical description of a general flow would be impossibly complicated. However, the problem can be simplified by considering only a particular class of interface distribution or 'flow regime'.

The most common regime in industrial systems is annular flow in which there is a liquid continuum adjacent to the channel wall with a central gas core. The two phases are separated by a reasonably well defined interface. There can be gas entrainment within the liquid layer or liquid drop entrainment in the gas core.

The importance of acquiring a fundamental understanding of the phenomena, particularly entrainment, occurring in annular two-phase flow can be illustrated by the following examples.

In vertical tube boilers and liquid cooled nuclear reactors it is desirable to have annular flow occurring in as much of the tube length as possible. This is due to the high rate of heat transfer to the liquid resulting from the thinness of the mean film and the high mean velocity. If, however, the film fails to wet part of the inside wall there is a very large reduction in the heat transfer coefficient in the dry area. This causes a rapid increase in the temperature of the wall which is often accompanied by tube fracture. This is called 'burn out'. The maximum rate of heat transfer is obtained by operating as close to the burn out condition as possible without any risk of the phenomenon actually occurring.

An inert liquid film is used to protect walls of rocket exhausts. The maximum effect is obtained if all the liquid remains in the protective film. Thus entrainment of the liquid film must be suppressed as much as possible.

Both of the above examples involve heat and mass transfer. However the fluid dynamics of the system are of primary importance and must be understood before further complications can be included.

A characteristic feature of annular flow is the occurrence of a complex pattern of waves on the interface between the two fluids. Although experimental results tend to be rather subjective, two types of waves have been identified (see Hewitt and Hall-Taylor (1970)). For low liquid rates the surface is covered by small capillary waves. These act as a surface roughness leading to an increased pressure drop. If the liquid flow-rate is then increased keeping the gas flow-rate constant, a reproducible critical flow-rate is reached. Above this critical flow-rate large disturbance waves occur. These waves are regions of highly disturbed interface and have amplitudes of several times the mean film thickness. They form a complete ring around the channel and have a continuous existence over long distances.

High speed photography of two-phase flow, both stratified horizontal (Woodmansee and Hanratty (1969)) and vertical (Whalley et al.(1977)), has indicated that entrainment occurs by the tearing away of filaments which break up from the surface of the waves. Also the presence of disturbance waves is a necessary, but not sufficient, criterion for the occurrence of entrainment. Thus it is important to study the behaviour of disturbance waves as part of a programme aimed at understanding and quantifying entrainment.

There are many difficulties associated with any attempt to produce a mathematical model for disturbance waves. The problem is of the 'free-boundary' type, which always tends to be difficult. Since the waves have amplitudes of several times the film thickness, they are certainly non-linear and linear solution methods are inappropriate. The gas stream is definitely turbulent (the gas Reynolds number is about 10^4) and it is not obvious how its effect should be modelled. The low liquid Reynolds number (about 50) means that the effect of viscosity is important in the liquid phase. The effect of the finite thickness of the film must also be taken into account. Finally, the film flow may also be turbulent due to the effect of the turbulent gas stream on the interface.

The problem is considerably more difficult than that of the generation and behaviour of ocean waves, in which the liquid phase can be treated as inviscid and semi-infinite. This simpler problem has still not been solved satisfactorily.

In the following chapters, the author examines the many mathematical models which have been proposed for disturbance waves. Their limitations and similarities are discussed together with their appropriateness for the particular case of upward vertical two-phase flow. Attention is focussed on the kinematic wave theory model and the 'integral method'. There is a discussion of the problem of modelling the effect of the turbulent gas phase and also of the connection between wave inception and the results of a linear stability analysis. Finally a numerical model, based on the SMAC (Simplified Marker And Cell) method, is developed which is capable of following the time dependent behaviour of large amplitude waves.

In this thesis the author aims to provide a clear and comprehensive account of the problems involved in the mathematical modelling of disturbance waves in vertical annular two-phase flow and the methods available to tackle them. She hopes that it will aid considerably future research workers. In addition, the SMAC numerical method is introduced as a useful research tool in this area.

CHAPTER 2. Mathematical Models for Disturbance Waves

2.1 Experimental Data

During the last twenty years there has been much research into disturbance wave phenomena in vertical annular two-phase flow. Hewitt and Hall-Taylor (1970) provide a summary of work carried out before 1970. However, most experimental data have been obtained for a narrow range of experimental conditions. Mainly air-water flows have been studied, at near atmospheric pressure and for a limited range of channel cross sections. Some experimental results are contradictory and there are few sets of consistent data. Considerable experimental difficulties are involved. Early experiments relied on observation and tended to be subjective. More accurate techniques, however, are continually being developed.

Film thickness data for various gas and liquid flow rates have been obtained using a conductance probe by Gill and Hewitt (1963) and Whalley et al.(1973). Hewitt and Nichols (1969) obtained profiles of individual waves using a fluorescence spectrometer. A continuous spectrum of heights was found with an average of about 5.3 times the mean film thickness. The ratio of maximum height to mean film thickness decreased with increasing gas flow rate. The maximum wave slope was only a few per cent.

Axial view photography (Whalley et al.(1977)) has shown disturbance waves to be highly non-uniform around their peripheries and to act as a source of entrainment.

Azzopardi (1979) made accurate and systematic measurements of disturbance wave velocities in upward annular two-phase flow using a cross-correlation technique. He found that they increased with increasing gas and liquid flow rates and were about 2-3 times the average film velocity. Gill et al.(1969) found that there was a small increase in wave velocity along the tube but that a steady state was soon reached. Wave velocities appear to depend linearly on the wave heights. Pashniak (1969) showed this to be approximately correct for individual waves. The mean value results of Pashniak and Hewitt and Nichols (1969) also show the same trend.

The wave spacing decreases with increasing liquid flow rate and tends to an asymptotic value. This minimum value decreases linearly with increasing gas flow rate. Azzopardi (1979) proposed an explanation for this behaviour based on a probabilistic analysis of wave coalescence.

Azzopardi et al.(1979) created disturbance waves by injecting a small volume of liquid into a film flowing at the critical rate for disturbance wave formation. The waves so formed were found to be equivalent to those occurring naturally at higher liquid flow rates. They also found evidence to suggest that waves do not always carry the same liquid with them and that the film is turbulent even between waves. Except at low flow rates, the volume of liquid associated with each wave depended on the gas and liquid flow rates. The entrained volume of liquid per wave depended linearly on the liquid flow rate but was largely independent of gas flow rate.

Finally, Shearer and Nedderman (1965) found that the onset of disturbance waves corresponded to a rapid increase in pressure drop along the tube.

Typical magnitudes of physical parameters for the experimental rig at AERE Harwell, used for example by Whalley et al.(1973), are

film thickness	h_0	10^{-4}m
tube radius	R_0	1.59×10^{-2}m
liquid Reynolds number	Re_L	10^2
gas Reynolds number	Re_G	10^4

2.2 Model Assumptions

Consider the upward vertical co-current flow of air and water in a circular pipe of radius R_0 (see Fig. 2.1). The following assumptions will be made in most of the mathematical models described in this thesis.

1. The viscosities and densities of both phases remain constant. This implies that the velocity of the air is much less than that of sound and that conditions are isothermal.

2. Either no entrainment is occurring or the rate of entrainment is equal to that of deposition. This implies that the system has reached equilibrium. Experimental results of Brown (1978) indicate that provided the porous sinter injection device is used, an approximation to equilibrium is attained within 140 diameters.

In horizontal flow it is possible to have large disturbance waves without entrainment. However, in vertical flow, there is nearly always entrainment associated with the passage of a disturbance wave.

3. The flow is axisymmetric. This assumption is not strictly true as shown by Whalley et al.(1977).

4. The flow in the liquid film is laminar. There is conflicting evidence regarding this assumption. In the ripple region, Re_L is in the range 50-100 and thus the flow would be expected to be laminar. Support for the assumption is also given in a paper by Jepson, Crosser and Perry (1966). Finally the assumption of a laminar velocity profile in the film together with the triangular relationship (Hewitt and Hall-Taylor (1970)) has been shown to give reasonable agreement with experimental results.

In contrast, experiments conducted by Azzopardi et al.(1979) on the dispersion of concentrated solution in a vertical annular film indicate that the experimental traces of time varying concentration at a fixed distance from the injector more closely resemble the theoretical predictions for turbulent film flow.

2.3 The Triangular Relationship

The simplest mathematical model for vertical wavy flow is the 'triangular relationship' of Hewitt and Hall-Taylor (1970). In this model, the following assumptions are also made:

1. The interface is flat except for small ripples whose effect is to present to the gas a moving rough wall. For turbulent gas flow this results in an increased friction factor.

2. A steady state with respect to time and distance has been reached.

With reference to Fig. 2.1, a force balance on a cylindrical element of the tube bounded by the interface gives

$$2\pi r_i \; \delta z \tau_i = \pi r_i^2 \left[p_G - (p_G + \frac{\partial p_G}{\partial z} \delta z)\right] - \int_0^{r_i} 2\pi r \frac{\partial}{\partial z} (G_G U_G) \; \delta z dr$$

$$- \int_0^{r_i} \int_0^{\delta z} 2\pi r \; \rho_G \; g \; drdz$$

where G_G is the gas mass flux per unit area tube cross-section and τ_i is the interfacial shear stress.

Using assumption 2, this reduces to

$$- \frac{dp_G}{dz} = \frac{2}{r_i} \tau_i + \rho_G g \tag{2.1}$$

For steady laminar flow in the liquid film $\underline{u}_L = (0, 0, u_z(r))$ and the equations of motion reduce to

$$\frac{dp_L}{dz} = \frac{\mu_L}{r} \frac{d}{dr} (r \frac{du_z}{dr}) - \rho_L g \tag{2.2}$$

$$p_G = p_L + \frac{\sigma}{R_o - h} \qquad r = R_o - h \tag{2.3}$$

$$\mu_L \frac{du_z}{dr} = \tau_i \qquad r = R_o - h \tag{2.4}$$

$$u_z = 0 \qquad r = R_o \tag{2.5}$$

From (2.2) - (2.5)

$$u_z = - \tau_i \frac{(R_o - h)}{\mu_L} \ln \frac{r}{R_o} - \left\{ \frac{g}{2\nu_L} (1 - \rho^*) - \frac{\tau_i}{\mu_L (R_o - h)} \right\}$$

$$\times \left\{ \frac{R_o^2 - r^2}{2} + (R_o - h)^2 \ln \frac{r}{R_o} \right\} \tag{2.6}$$

The total film flow rate W_{LF} is given by

$$W_{LF} = \int_{R_o - h}^{R_o} 2\pi \rho_L r u_z \, dr$$

$$= \frac{2\pi\rho_L}{\mu_L} \left\{ \left[\tau_i (R_o - h) + \frac{1}{2} (\rho_L g (1 - \rho^*) - \frac{2\tau_i}{(R_o - h)}) (R_o - h)^2 \right] \right.$$

$$\times \left[\frac{1}{4} (R_o^2 - (R_o - h)^2) - \frac{1}{2} (R_o - h)^2 \ln \frac{R_o}{R_o - h} \right]$$

$$\left. - \frac{1}{16} (\rho_L g (1 - \rho^*) - \frac{2\tau_i}{(R_o - h)} (R_o^2 - (R_o - h)^2)^2 \right\} \tag{2.7}$$

Equation (2.7) is known as the 'triangular relationship' and connects the three unknowns h, τ_i, W_{LF}. The simplest models for wavy annular flow specify a correlation between two of these variables (taking h, τ_i to be the average film thickness and interfacial stress respectively) and use

(2.7) as a relationship between the other two. Examples of correlations are given by Hewitt and Hall-Taylor (1970).

Nondimensional variables can be defined by

$$u_z = u_o \bar{u}_z$$

$$\tau_i = \rho_L u_o^2 \bar{\tau}$$

$$r = R_o - h\ (1 + y)$$

Substituting into (2.6), expanding for $\frac{h}{R_o} << 1$ and neglecting $\rho^* = \frac{\rho_G}{\rho_L} << 1$, the lowest order terms give

$$\bar{u}_z = (T - \frac{G}{2}) + Ty + \frac{G}{2} y^2 \tag{2.8}$$

where $T = Re_L \bar{\tau}$ $\qquad G = \frac{gh^2}{u_o \nu_L}$

and $Re_L = \frac{u_o h}{\nu_L}$

2.4 Equations of Motion for a Perturbed Interface

In this section, the problem of a perturbed interface will be considered. The assumptions 1-4 outlined in section 2.2 will be made. Since $^h/R_o \sim 10^{-2}$ for vertical annular flow, as a first approximation it is sufficient to use two dimensional rectilinear equations of motion rather than their equivalents in cylindrical co-ordinates. This leads to a considerable simplification in the analysis.

For the case of laminar flow in both phases, it is possible to solve simultaneously the equations of motion for each phase together with the coupling interfacial conditions. However, particularly for the case of turbulent gas flow, it is often easier to consider the problem in two stages. First the normal and tangential stresses exerted by the gas on an arbitrary film surface perturbation are calculated. These expressions are then substituted into the perturbation equations for the liquid phase. Since $Re_G \sim 10^4$ for the experimental conditions being studied, the gas flow is almost certainly turbulent. Consequently the second approach will be used.

Consider the slightly more general problem of the two-dimensional flow of a liquid film down a plane $y = -h_0$ inclined at an angle β to the horizontal (see Fig. 2.2). Let the surface be given by $y = \eta\,(x, t)$ and the liquid be acted on by surface stresses $N_s(x)$, $\tau_s(x)$.

The equations of motion are:

$$u_t + uu_x + vu_y = g\sin\beta - \frac{1}{\rho_L}\,p_{Lx} + \nu_L\,(u_{xx} + u_{yy}) \tag{2.9}$$

$$v_t + uv_x + vv_y = -g\cos\beta - \frac{1}{\rho_L}\,p_{Ly} + \nu_L\,(v_{xx} + v_{yy}) \tag{2.10}$$

$$u_x + v_y = 0 \tag{2.11}$$

The appropriate boundary conditions are:

$u = v = 0$ $\qquad$ $y = -h_0$ no-slip condition $\qquad$ (2.12)

$v = \eta_t + u\eta_x$ $\qquad$ $y = \eta$ kinematic boundary condition (2.13)

$$-p_L + 2\mu_L\left[\frac{u_x\,\eta_x^2 - (u_y + v_x)\,\eta_x + v_y}{1 + \eta_x^2}\right] + \frac{\sigma\,\eta_{xx}}{(1 + \eta_x^2)^{3/2}} = N_s$$

$y = \eta$ $\qquad$ continuity of normal stress $\qquad$ (2.14)

$$2\,\mu_L\,(v_y - u_x)\eta_x + \mu_L\,(v_x + u_y)\,(1-\eta_x{}^2) = \tau_s \qquad y=\eta$$

continuity of tangential stress (2.15)

Introduce non-dimensional variables

$$x = L\bar{x} \quad y = h_o\bar{y} \quad \eta = \eta_o\bar{\eta} \quad u = u_o\bar{u} \quad t = \frac{L}{u_o}\,\bar{t}$$

Non-dimensionalise the pressure and surface stresses with respect to $\rho_L u_o{}^2$.

From (2.11) $v = \delta u_o\bar{v}$ where $\delta = \frac{h_o}{L}$

Substituting into equations (2.9) - (2.15) gives (dropping bars):

$$\left.\begin{aligned}
&u_t + uu_x + vu_y = \frac{1}{\delta F^2}\sin\beta - p_{Lx} + \frac{1}{Re_L}\left(\delta u_{xx} + \frac{1}{\delta}u_{yy}\right)\\
&\delta\,(v_t + uv_x + vv_y) = -\frac{1}{\delta F^2}\cos\beta - \frac{1}{\delta}\,p_{Ly} + \frac{1}{Re_L}\,(\delta^2 v_{xx} + v_{yy})\\
&u_x + v_y = 0\\
&u = v = 0 \qquad y = -1\\
&v = \eta_t + u\eta_x \qquad y = \varepsilon\eta\\
&-p_L + \frac{2}{Re_L}\left\{\frac{\delta^3\varepsilon^2 u_x\eta_x{}^2 - \eta_x(u_y + \delta^2 v_x)\,\delta\varepsilon + v_y\delta}{1 + \varepsilon^2\delta^2\eta_x{}^2}\right\}\\
&+ W\delta^2\eta_{xx} = N_s \qquad y = \varepsilon\eta\\
&2\delta^2\,(v_y - u_x)\varepsilon\eta_x + (\delta^2 v_x + u_y)\,(1-\delta^2\varepsilon^2 h_x{}^2) = Re_L\tau_s\\
&\qquad y = \varepsilon\eta
\end{aligned}\right\} \quad (2.16)$$

The following non-dimensional parameters have been introduced:

Reynolds number $\quad Re_L = \dfrac{u_o h_o}{\nu_L}$

Froude number $\quad F = \dfrac{u_o}{\sqrt{g h_o}}$

(Weber number)$^{-1}$ $\quad W = \dfrac{\sigma}{\rho_L u_o^2 h_o}$

$\delta = \dfrac{h_o}{L}$ - the 'shallow water' parameter.

$\varepsilon = \dfrac{\eta_o}{h_o}$ - a measure of the amplitude of the disturbance.

The primary film flow, with $\varepsilon = 0$, is given by $(U(y),0)$ where

$$U(y) = (T-\frac{G'}{2}) + Ty + \frac{G'y^2}{2}$$

where $T = Re_L \, \bar{\tau}_s$

$$G' = Re_L \left\{ \delta p_{Gx} - \frac{1}{F^2} \sin\beta \right\}$$

and $\quad \bar{p} = p_G(x) - \dfrac{1}{F^2} \cos \beta y$

Further progress requires the knowledge of the relative magnitudes of the parameters ε, δ, Re_L. The limit $Re_L \to \infty$, ε and δ fixed, gives the inviscid equations. These are considered by Nash (1978). In the following sections other simplifying choices of parameter size are discussed, together with their relevance to a disturbance wave model.

2.5 The Linearised Problem (ε<<1)

Consider an infinitesimal perturbation about the primary film flow $U(y)$. If the flow variables are expanded in terms of the parameter ε, assumed small, the linearised forms of the equations of motion become

$$
\left.
\begin{aligned}
& u'_t + Uu'_x + U'V = -p_L{}'_x + \frac{1}{Re_L}\left\{\delta u'_{xx} + \frac{1}{\delta}u'_{yy}\right\} \\
& \delta\,(v'_t + Uv'_x) = -\frac{1}{\delta}\,p'_{Ly} + \frac{1}{Re_L}\left\{\delta^2 v'_{xx} + v'_{yy}\right\} \\
& u'_x + v'_y = 0 \\
& u' = v' = 0 \qquad\qquad y = -1 \\
& v' = \eta_t + u\eta_x \qquad\qquad y = 0 \\
& -\bar{p}_{Ly}\eta - p'_L + \frac{2}{Re_L}\left\{U_y\eta_x + v'_y\,\delta\right\} + W\delta^2\eta_{xx} = N'_s \qquad y = 0 \\
& \delta^2 v_x + u'_y + U_{yy}\,\eta = Re_L\,\tau'_s \qquad\qquad y = 0
\end{aligned}
\right\} \quad (2.17)
$$

where ' refers to perturbation quantities.

These equations can be reduced to the Orr-Somerfeld equation together with boundary conditions. Further details are given in Chapter 4.

If δ, Re_L are chosen to satisfy $\delta \ll 1$, $Re_L \gg 1$ and $\delta^2 Re_L \gg 1$, and $\frac{1}{F^2}\cos\beta$ is taken equal to unity, then the limit $\varepsilon \to 0$, $\delta \to 0$ reduces the equations to those studied by Burns (1953). This paper examined the propagation of small disturbances on a general (inviscid) shear flow. The appropriate equations are:

$$
\left.\begin{array}{ll}
u'_t + Uu'_x + U_y v' + p'_{Lx} = 0 & \\
p'_{Ly} = 0 & \\
u'_x + v'_y = 0 & \\
v' = 0 & y = -1 \\
v' = \eta_t + U\eta_x & y = 0 \\
p'_L = \eta \frac{1}{F^2} \cos\beta = \eta & y = 0 \\
u'_y + U_{yy}\eta = 0 & y = 0
\end{array}\right\} \quad (2.18)
$$

Seeking a steady wave solution of (2.18) gives directly

$$\eta = \eta \quad (x - ct)$$

$$u' = -\eta \frac{d}{dy} (\tilde{W} I_2)$$

$$I_n = \int_{-1}^{y} \frac{dy}{\tilde{W}^n}$$

$$\tilde{W} = U(y) - c$$

c is the constant wave speed given by the integral relation

$$\int_0^1 \frac{dy}{(U-c)^2} = 1$$

The analysis breaks down for the case of vertical flow, $\cos\beta = 0$. It is also not appropriate for modelling disturbance waves with amplitudes several times the film thickness, for which $\varepsilon = O(1)$.

2.6 Soliton Type Theories

A considerable amount of research has been conducted in recent years into the theory of 'solitons' (see e.g. Miura (1976), Miles (1980)). Solitons are solitary waves; that is they are isolated travelling waves of fixed shape propagated with constant speed. In addition, they possess at least one of the following two properties:

1. Two or more solutions of different speeds (and hence different amplitudes) pass through each other in a complicated interaction to emerge undistorted except for a phase shift.

2. A general profile breaks up, after a long time, into a train of solutions separated by or from a disturbance which disperses and decays with time and is called the 'radiation'.

The equation with soliton solutions most frequently studied is the Korteweg-de-Vries equation:

$$\eta_t + \frac{3}{2}\eta\eta_x + \alpha\eta_{xxx} = 0 \tag{2.19}$$

This has the soliton solution

$$\eta = a\ \mathrm{sech}^2\left[\left(\frac{a}{8\alpha}\right)^{\frac{1}{2}}(x - ct)\right] \tag{2.20}$$

where a = 2c

Soliton theory is a 'finite amplitude' rather than an infinitesimal theory. It is known to be relevant to one phase channel flow (see e.g. Miles (1980)). In this context, equation (2.19) denotes a balance between the linear tidal term η_t, the nonlinear shallow water term $\eta\eta_x$ and the dispersion term η_{xxx}.

Certain experimental evidence has encouraged research workers to seek to apply soliton theory to the modelling of disturbance waves in two-phase flow. Experimental data for both horizontal flow (Miya et al. (1971)) and vertical flow (Azzopardi (1978)) indicate that, at a fixed gas flow rate, the velocities of disturbance waves are (almost) linearly related to their peak heights. This linear behaviour is also true of solitons. Results of Telles (1968) for vertical flow suggest that the waves are symmetrical and reasonably fitted by a sech^2 profile. Finally, disturbance waves are known to persist over distances of several metres.

Rae (1975) considered the two dimensional horizontal irrotational flow of two inviscid incompressible fluids. Turbulence in the lower fluid was neglected. Turbulence in the upper fluid was modelled by a normal Reynolds stress $\bar{\tilde{V}}^2$ incorporated into the interfacial normal stress condition. Motion in the two phases was treated simultaneously. The equations of motion reduced to a form of the Korteweg-de-Vries equation with modified coefficients. The resulting relationship between wave amplitude and speed agreed well with the results of Telles (1968) and Zanelli and Hanratty (1971).

Nash (1978) studied a similar problem but ignored all effect of turbulence. She showed that the problem reduced to one of three equations depending on the ratio of the thicknesses of the two phases. All three are special cases of the Whitham (1974) general wave equation

$$\eta_t + \frac{3}{2}\eta\eta_x + \int_{-\infty}^{\infty} K\,(x-x')\eta_{x'}\,(x',t)\,dx' = 0 \tag{2.21}$$

where $$K(x) = \frac{1}{2\pi}\int_{-\infty}^{\infty}[c(k)-c_0]\,e^{-ikx}\,dk$$

and $c(k)$ is the dispersion relation for the linearised system.

The important parameters are $v = \dfrac{V}{\sqrt{gh_0}}$, $d = \dfrac{\rho_2}{\rho_1}$ and $\xi = \dfrac{h_0}{H_p}$ (see Fig. 2.3). When these parameters are all $O(1)$, the dispersion relation takes the form

$$c(k) = c_0\,(1-\gamma k^2)$$

leading to the KdV equation (2.19) and solitary wave solutions of the form

(2.20). When $\frac{1}{V}$, $\sqrt{d}$ and ξ are all $O(\delta)$, the dispersion relation has the form

$$c(k) = c_0\ (1 - \alpha k \coth k) \tag{2.22}$$

leading to the 'BOJ' equation (see Joseph (1977)) with solitary wave solution

$$\eta = \frac{\frac{4}{3}\, c_0\ \alpha \sin \delta}{\cosh {}^{\delta}/D\ s + \cos\delta} \qquad 0<\delta<\pi$$

where $s = x - c_0\ \alpha \cos\delta\ t$.

In the limit $\xi \to 0$, corresponding to a semi-infinite upper fluid,

$$c(k) = c_0\ (1 - \beta|k|) \tag{2.23}$$

leading to the 'BO' equation (see Benjamin (1967))

$$\eta_t + \frac{3}{2}\eta\eta_x + \frac{1}{2}\beta \frac{\partial^2}{\partial x^2} \mathcal{H}(x) = 0$$

where $$\mathcal{H}(x) = P\, \frac{1}{\pi} \int_{-\infty}^{\infty} \frac{\eta(s,t)}{x-s}\, ds$$

with solitary wave solution

$$\eta = \frac{\frac{8}{3}\frac{\beta}{b}}{1 + {}^{s^2}/b^2}$$

where $s = x - \frac{\beta}{b} t$

Equation (2.23) or that corresponding to (2.22) would be expected to be the more relevant for application to interfacial waves in two-phase flow since $\frac{h}{R_0} \sim 10^{-2}$.

The models of Rae and Nash neglect the effect of turbulence or viscosity in the lower fluid. James (1978) attempted to account partially for viscosity and turbulence by allowing the mean gas and liquid flow to have arbitrary velocity profiles. The fluids were then treated as being inviscid. Like Rae, he modelled the effect of normal Reynolds stresses by a $\bar{\tilde{V}}^2$ term. However, in James' analysis the term occurred in the momentum equation in the y direction for the two phases. His analysis is similar to that of Freeman and Johnson (1970) for single-phase flow and leads to the KdV equation once the assumption $\varepsilon = \delta^2 << 1$ has been made.

Study of the soliton theories has provided the author with the following evidence against their application to disturbance wave modelling in vertical two-phase flow.

The soliton theories all depend upon the assumption that the parameter ε is small. The derivation of the KdV equation requires $\varepsilon = \delta^2 << 1$ while (2.23), (2.22) require $\varepsilon = \delta << 1$. Thus they cannot be expected to be valid for disturbance waves, the amplitudes of which are several times the film thickness.

Disturbance waves are also observed to coalesce in contrast to the behaviour of solitons.

The analysis leading to (2.21) is invalid if the dispersion relation for the linearised system gives a complex value for c(k), corresponding to an unstable wave. If Rae's analysis is applied to vertical flow,there is no stabilising gravitational force and c is only prevented from becoming complex by the inclusion of the term $\bar{\tilde{V}}^2$. Similarly, without the inclusion of the Reynolds stress term, James' analysis breaks down in the manner of the linear Burns solution for one phase flow described in section 2.5.

Thus the specification of the rather speculative term $\bar{\tilde{V}}^2$ is crucial. In Chapter 3 evidence will be given for suggesting that the effect of the random turbulent stresses exerted by the gas on the liquid film is negligible compared with other interfacial stresses neglected in both of these models. In Chapter 4, when the full linear stability analysis for vertical annular flow is considered, it will be shown that the interface is always unstable and thus the dispersion relation gives complex values of c for suitable values of k.

Taking all the above factors into consideration, it appears to the author that soliton theory is not applicable to the modelling of disturbance waves in vertical annular two-phase flow.

2.7 The Long Wave Approximation ($\delta \ll 1$)

Representative of this approach is the work of Benney (1966), Mei (1966), Lin (1969), Krantz and Goren (1970) and Gjevik (1970) for the case of one-phase flow, $N_s = \tau_s = 0$. The stream function ψ is introduced such that

$$u = \psi_y \qquad v = -\psi_x$$

ψ is then expanded in terms of δ

$$\psi = \psi_0 + \delta\psi_1 + \delta^2 \psi_2 + \ldots$$

and substituted into the equations of motion. By equating powers of δ, ψ_i can be calculated in terms of η. Approaches to date have generally only included the first two terms of the series. The resulting expressions for ψ_i are substituted into the kinematic boundary condition. This leads to a partial differential equation in η of fourth order and seventh degree

$$\bar{f}\,(\eta,\, x,\, t,\, Re_L,\, W,\, F,\, \beta,\, \delta) = 0$$

or equivalently

$$f\,(\eta,\, x,\, t,\, Re_L,\, W,\, F,\, \beta,\, h_0\alpha) = 0 \qquad (2.24)$$

where α = wave number $= \frac{2\,\pi}{L} = \frac{k}{h_0}$

One path to a solution of (2.24), adopted by Krantz and Goren (1970), is to assume the existence of permanent waves of constant shape and speed of propagation c. A new variable $z = x - ct$ is introduced and the equation reduced to an ordinary differential equation for η as a function of z. This equation can be integrated once to produce an equation of the third order, seventh degree. In order to solve this for the wave amplitude k and c have to be specified. Goren used linear stability theory to find k, c for the most highly amplified wave and assumed that these would be the dominant values for conditions of larger amplitude waves and higher values of Re_L. A difficult non-linear differential equation still remains to be solved.

Gjevik (1970) followed the original work of Benney (1966). He assumed η to be a periodic function of x and approximated its shape by the first three harmonics in a Fourier series.

$$\eta = \sum_{1}^{3} (A_N(t) \cos Nkx + B_N(t) \sin Nkx)$$

Substituting into (2.24) and equating harmonics produces a set of non-linear first order equations for $A_N(t)$, $B_N(t)$. The study of the growth of an initially linear disturbance shows that a stationary solution exists only for values of k, Re_L near conditions of linear neutral stability. For higher values of Re_L, a relatively rapid build up of the higher harmonics is anticipated.

The long wave approximation approach can be used for annular two phase flow. The equation corresponding to (2.24) derived by the author is given in Appendix 1. It depends critically on the forms assumed for the surface stresses $N_S(x,t)$, $\tau_S(x,t)$. If the integral expressions, to be derived in Chapter 3, are assumed, (A.1) becomes an extremely complicated non-linear integro-differential equation. The validity of the analysis also depends on the assumption that Re_L is O(1). For the more physically realistic case,

$Re_L = O(\frac{1}{\delta})$, the equations for ψ_i become insoluble non-linear partial differential equations and the method breaks down.

In his method of solution of (2.24), Goren assumed that the speed of the large amplitude wave was given by the linear stability analysis. It will be shown in Chapter 4 that, for vertical annular flow, this speed can be less than that of the film surface. Experimental measurements have shown that the speed of disturbance waves can be several times that of the film surface.

It will also be shown in Chapter 4 that the interface is always unstable. Thus it is unlikely the method of Gjevik will produce a stationary solution.

Taking account of all the above factors leads the author to the conclusion that the methods described in this section are not suitable for modelling disturbance waves in vertical annular two-phase flow.

2.8 The Integral Approach

Consider the equations of motion (2.16). Assume $\delta \ll 1$, corresponding to long waves and that $Re_L = O(\frac{1}{\delta})$, $\varepsilon = 1$. These assumptions are reasonable for the case of waves in annular two-phase flow. A wave with a maximum slope of a few per cent corresponds to $\delta \sim 10^{-2}$ while the second condition corresponds to $Re_L \sim 10^2$. Neglecting $O(\delta^2)$ the equations (2.16) reduce to (now taking bottom to be at $y = 0$ and the surface to be at $y = h$):

$$u_t + uu_x + vu_y = \frac{1}{\delta F^2}\sin\beta - p_{Lx} + \frac{1}{Re_L\delta}u_{yy} \tag{2.17}$$

$$0 = \frac{1}{F^2}\cos\beta - p_{Ly} \tag{2.18}$$

$$u_x + v_y = 0 \tag{2.19}$$

$$u = v = 0 \qquad y = 0 \tag{2.20}$$

$$v = h_t + uh_x \qquad y = h \tag{2.21}$$

$$u_y = Re_L \tau_s \qquad y = h \qquad (2.22)$$

$$- p_L + W\delta^2 h_{xx} = N_s \qquad y = h \qquad (2.23)$$

Also $\quad u_y = Re_L \tau_w \qquad y = 0$

From (2.19) $\quad v = - \int_o^y u_x \, dy$

Substituting into (2.21) gives

$$h_t + u_s h_x + \int_o^h u_x \, dy = 0 \qquad (2.24)$$

where $\quad u_s = u(h)$

Define $\quad u_a = \frac{1}{h} \int_o^h u \, dy$

u_a is the liquid velocity down the plane, averaged over the film thickness. Then from (2.24)

$$h_t + (u_a h)_x = 0 \qquad (2.25)$$

From (2.18), (2.23)

$$p_L = - \frac{1}{F^2} \cos\beta \, (y-h) + W\delta^2 \, h_{xx} - N_s$$

Substituting for p_{Lx} in (2.17) and integrating over (0,h) gives finally

$$(u_a h)_t + (h u_a{}^2 \Gamma)_x = \frac{1}{\delta} (\tau_s - \tau_w) + \frac{1}{F^2 \delta} \sin\beta \, h - \frac{1}{F^2} \cos\beta \, h h_x$$

$$- h W \delta^2 h_{xx} + N_{sx} h \qquad (2.26)$$

where the 'shape factor' Γ is defined by

$$\Gamma = \frac{1}{hu_a^2} \int_0^h u^2 \, dy$$

The magnitudes of F, W, β have yet to be determined and Γ, $(\tau_s - \tau_w)$, N_s specified in terms of h, u_a, x, t. (2.25), (2.26) have then to be solved subject to initial conditions

$$u_a = u_i(x) \qquad h = h_i(x) \qquad t = 0$$

For a non-trivial solution, from (2.26) either $\beta \leqslant 0(\delta)$ or $F = 0(\delta^{-\frac{1}{2}})$. Also $\tau_s - \tau_w$ must be $0(\delta)$.

In methods of solution of equations of the type (2.25), (2.26) usually a 'self-similarity' profile assumption is made. It is assumed that the velocity profile under a wave is the same as it would be for a flat film of thickness h(x). Clearly this assumption is not valid at any point where h'(x) is not small, for example in the front of a breaking wave. The integration process for calculating u_a,Γ is relied on to make the result relatively insensitive to the shape of the velocity distribution assumed provided the boundary conditions are nearly satisfied.

An example of the use of the integral approach is Kapitza's (1964) work on falling films. He assumed that the wave had a steady profile with constant speed c and introduced the variable z = x - ct. (2.25) integrates to give

$$(c - u_a)h = \text{const} = q_o \tag{2.27}$$

(2.26) becomes

$$(-cu_a h)_z + (hu_a^2 \Gamma)_z = -\frac{1}{\delta}\tau_w + \frac{1}{F^2 \delta} h - W\delta^2 \, hh_{xxx} \tag{2.28}$$

Kapitza assumed the velocity profile

$$\frac{u}{u_a(z,t)} = \frac{y}{h(z)} - \frac{1}{2}\left(\frac{y}{h(z)}\right)^2$$

This enabled Γ, τ_w to be determined in terms of u_a,h. u_a was then eliminated from (2.27), (2.28) to give an ordinary differential equation of third order and fourth degree

$$f(h,\ z,\ Re_L,\ W,\ F,\ h_o k,\ c) = 0 \qquad \delta = h_o k \tag{2.29}$$

Once again an extra relationship between c and k is required before the problem can be solved completely.

Methods of solution of (2.29) generally depend on assuming a Fourier series for $\eta = h - 1$

$$\eta = \sum_N \beta^N (A_N \sin Nkz + B_N \cos Nkz)$$

$$A_1 = 1 \qquad B_1 = 0$$

This is effectively a small amplitude expansion and is thus not suitable for large amplitude waves. Telles (1968) assumed a Gram-Charlier rather than a Fourier series. The extra equation is supplied either by a minimization principle (Shkadov (1967)), a correlation between A_1 and $Re_L/W^{\frac{1}{2}}$ (Berbente and Ruckenstein (1968)) or experimental values of A_1 (Telles (1968)).

A second example of the integral approach is Dressler's (1949) solution for roll waves in an inclined open channel. He considered turbulent flow and assumed a uniform velocity profile and the Chezy formula for the wall shear stress. This gives

$$\tau_w = \delta\, C_f\, u_a^2 \qquad \Gamma = 1$$

where C_f is a friction factor.

Returning to dimensional variables and putting $g' = g\cos\beta$, $s = \tan\alpha$, the equation for steady waves corresponding to (2.28) is

$$h(u_a - c)\frac{du_a}{dz} + g'h\frac{dh}{dz} = hg's - C_f u_a^2 \qquad (2.30)$$

Using (2.27) to eliminate u_a gives

$$\frac{dh}{dz} = -\frac{(q_o - ch)^2 C_f - g'h^3 s}{g'h^3 - q_o^2} \qquad (2.31)$$

Thomas (1940) analysed all possible solutions of (2.31) and showed that there are no continuous periodic solutions. Dressler (1949) constructed a discontinuous solution of equation (2.31). He obtained a shock relation by integrating (2.30) with respect to z (equivalent to starting from the integral conservation form of the momentum equation) and letting the interval in z tend to zero. The right hand side of (2.30) is finite at a discontinuity in h. The shock condition becomes

$$h\left(\frac{q_o^2}{h^2} + \frac{g'h}{2}\right)\Bigg|_{x=0^-}^{x=0^+} = 0 \qquad (2.32)$$

The denominator of (2.31) vanishes for some $h = h_c$. Dressler showed that, for a solution to exist, the numerator must also vanish at $h = h_c$. Both numerator and denominator in (2.31) can therefore be divided by $(h-h_c)$ and the equation integrated. The extra equation required (see above) is provided by (2.32). Dresslers solution is shown in Fig. 2.4.

2.9 Miya's Integral Method

Miya (1970) considered horizontal co-current stratified flow of air and water in a rectangular channel of depth B. He assumed a turbulent velocity profile for the liquid film. He modelled the turbulence by assuming that a dimensionless velocity profile valid for single phase flow could also be applied to the liquid film (the Colburn-Carpenter hypothesis). Miya used the van Driest profile

$$\frac{du^+}{dy^+} = \frac{2}{1 + \left[1 + 4K^2 y^{+2}\,\{1-\exp(-y^+/A^+)\}^2\right]^{\frac{1}{2}}} \qquad (2.33)$$

where $\quad u^+ = \frac{u}{u^*} \qquad y^+ = \frac{yu^*}{\nu_L} \qquad$ and $\qquad u^* = \left(\frac{\tau_w}{\rho_L}\right)^{\frac{1}{2}}$

The constants were chosen to be $A^+ = 26.0$ and $K = 0.6$ so as to give the best agreement with experimental data for three dimensional waves in a similar channel.

Miya assumed a steady wave profile. Once the constant wave speed c had been fixed and the discharge coefficient q_0 had been calculated from undisturbed film flow quantities, Miya was able to determine τ_w,Γ as functions of h(z). To be consistent τ_s should also be determined as a function of h:

$$\tau_s = \tau_w \left.\frac{du^+}{dy^+}\right|_{h^+}$$

Miya, however, did not use this expression for τ_s but derived an alternative form by considering the gas flow equations.

A possible justification occurring to the author for this inconsistency lies in the fact that any proposed turbulence model for the film is necessarily highly speculative. Any film turbulence is due to surface agitation and occurs at Reynolds numbers well within the usual laminar flow region. Even assuming that the Colburn-Carpenter hypothesis is valid in the case of a smooth surface, the velocity profile under a wavy surface is likely to be very different. It could be argued that it is only the velocity profile close to the surface which departs significantly from the form (2.33) and that τ_w and Γ can be calculated from (2.33) whereas τ_s has to be determined by other methods. Although such an approach may yield reasonable results for the case of very small disturbances, it is likely to be seriously in error when the wave amplitude is of the same order as the film thickness.

Miya used an integral approach for the gas phase similar to that described for the liquid phase. His assumptions were:

1. $N_s = - p_G$.
2. The gas pressure p_G is independent of y.
3. The gas velocity profile can be regarded as uniform ($\Gamma_G = 1$).

Transforming to a co-ordinate system moving with the wave, the resulting (dimensional) integral momentum equation is

$$\frac{d\left[\frac{\rho_G}{2}(\bar{U}_G - c)^2\right]}{dz} = -\frac{1}{(B-h)}(\tau_s + \tau_B) - \frac{dp_G}{dz} \qquad (2.34)$$

An integral mass balance in the gas phase similar to that in the liquid phase gives

$$(B-h)(\bar{U}_G - c) = (B-h_o)(\bar{U}_{Go} - c) \qquad (2.35)$$

From (2.34), (2.35) the pressure gradient in the gas phase is given by

$$\frac{dp_G}{dz} = -\frac{\rho_G}{2}\frac{(B-h_o)^2(\bar{U}_{Go} - c)^2(2\frac{dh}{dz} + f_s + f_B)}{(B-h)^3} \qquad (2.36)$$

where $$\tau_s = \frac{\rho_G}{2} f_s (\bar{U}_G - c)^2$$

$$\tau_B = \frac{\rho_G}{2} f_B \bar{U}_G^2$$

f_B was obtained from measurements in a dry channel and regarded as being constant. Substitution of (2.36) into the liquid film equations leads to an equation of the form

$$M_1 \frac{dh}{dz} = M_2 \tag{2.37}$$

where M_1, M_2 are functions of h, c and M_2 is linear in the remaining unspecified parameter f_s. For relatively high gas velocities M_1 is always positive. This is in contrast to Dressler's equation (2.31).

In order to determine f_s, Miya made the following assumptions

1. At the wave crest and trough $\frac{dh}{dz} = 0$

Thus $$M_2\big|_{h_o} = M_2\big|_{h_{max}} = 0 \tag{2.38}$$

2. (Based on experimental data) f_s has the form

$$f_s = f_{so} + A\,(Re_L - Re_{Lo})$$

Miya also assumed an experimental linear relationship between h_{max} and c. This corresponds to the extra relation which has to be supplied in the methods of sections 2.7, 2.8. Then f_{so} and A can be determined using (2.38).

The equation (2.37) was integrated between h_o and h_{max} using the Runge-Kutta method. Experimental measurements indicated that τ_w decreased sharply to below τ_{wo} in the front of the wave. The wall shear stress in this region was expressed by means of a quartic fitted to the experimental data. In this way the function h in the front of the wave could be calculated.

The wave profiles obtained by this procedure were in reasonable agreement with experimental results. However, Miya admitted that this was due to a large extent to the use of (2.38) to determine f_s at the peak of the wave.

An attempt to use Miya's method for the case of vertical annular flow will be described in Chapter 8.

2.10 Alternative Approaches

Several research workers have tried to deduce characteristics of large amplitude waves by means of simple integral balances.

Dukler (1976) considered a control volume consisting of the front of a large wave in falling film flow (see Fig. 2.6). The dimensions L_f, h_p and h_o as well as the speed c are all measurable. The front of the wave was approximated by a line of constant slope. On taking a co-ordinate system moving with the wave, the integral momentum and continuity equations become (c.f. (2.26), (2.25)):

$$2\pi R_o \left[\rho(u_o-c)h_o\right] (u_o-c) - 2\pi R_o \left[\rho(u_p-c)h_p\right] (u_p-c) - F_g + F_s = 0$$

$$\left[u_o-c\right] h_o = (u_p-c)h_p$$

Combining these two equations and assuming F_s is constant gives (correcting a mistake in Dukler's paper):

$$c = u_o + \left[\frac{gL_f \left(1 + \frac{h_p}{h_o} - \frac{2\tau_w}{\rho_L g h_o}\right)}{2\left(1 - \frac{h_o}{h_p}\right)}\right]^{\frac{1}{2}}$$

Dukler examined the assumptions $\tau_w = \rho_L g h_s$ and $\tau_w = 0$. The latter, corresponding to a mixing vortex and separation at the wall in front of the wave, gave results closer to experiment. Dukler deduced the flow pattern shown in Fig. 2.7. He visualised the wave as a large liquid lump, acting as a reservoir of fresh liquid, moving rapidly downward, sweeping up liquid from the film in front and laying down a fresh film behind.

Pearce (1979) used a similar approach for two phase flow. He made what the author believes to be a rather unjustified assumption that the change in momentum from the trough to the peak is the same in the film and gas core. Taking a co-ordinate system moving with the wave, the momentum balance for the film and gas core then gives

$$\rho_G \, (R_o-h_o)^2 \, (V_o-c) \, | V_p-V_o | = 2\rho_L \, R_o \, (c-u_o) \, | u_p-u_o |$$

where $\frac{h_o}{R_o}$ is assumed to be small, and V is the gas velocity.

The continuity equations are

$$(R_o-h_o)^2 \, (V_o-c) = (R_o-h_p)^2 \, (V_p-c) \qquad \text{for the gas core}$$

$$h_o(c-u_o) = h_p(c-u_p) = h_m(c-u_m) \qquad \text{for the film. (m denoting mean film quantities).}$$

From these equations

$$c = \frac{\frac{h_m}{\sqrt{h_o h_p}} \, u_m + \left(\frac{\rho_G}{\rho_L}\right)^{\frac{1}{2}} U_G}{\frac{h_m}{\sqrt{h_o h_p}} + \left(\frac{\rho_G}{\rho_L}\right)^{\frac{1}{2}}}$$

assuming $V_o = U_G$, the average gas velocity. This expression gives predictions for c which are 50% higher than the measured values. However, good agreement with the experimental results of Whalley et al. (1974) and Azzopardi (1979) is obtained using a correlation of the same form:

$$c = \frac{u_s + U_G \left(\frac{\rho_G}{\rho_L}\right)^{\frac{1}{2}}}{1 + \left(\frac{\rho_G}{\rho_L}\right)^{\frac{1}{2}}}$$

where u_s is the film surface speed.

In an attempt to test the 'self-similarity' profile assumption implicit in Miya's integral method, James (1979) integrated the continuity equation (2.25) to give

$$h\ (\bar{u}-c) = \text{constant} = h_m\ (\bar{u}_m - c)$$

where m refers to mean film properties. A further relation between $\bar{u}$ and h was obtained by assuming the Van Driest turbulent velocity profile for the film and a force balance to connect τ_w and τ_s:

$$\tau_w = \tau_s \left[1 + \frac{2h}{R_o}\right] - \rho_L g h \left[1 - \frac{h}{R_o}\right]$$

Finally the surface stress was determined by the Wallis (1970) correlation:

$$\tau_s = \frac{0.0395\ \rho_G\ V_{GC}^2}{Re_{GC}} \left(1 + 360\ \frac{h}{R_o}\right)$$

where the gas core velocity V_{GC} is defined by

$$V_{GC} = \frac{G_{LE}}{\bar{C}}$$

with

$$\bar{C} = \frac{G_{LE}}{\rho_L} + \frac{G_G}{\rho_G}$$

where G_{LE} is the entrained liquid mass flux.

This correlation is valid for mean film properties in the disturbance wave region but over-predicts the mean shear stress in the ripple region.

James compared the calculated values of c given the peak height h_p with the experimental results of, among others, Hewitt and Nicholls (1968). In each case the predicted c was considerably greater than the experimental value (see Table 2.1). James also tried to correlate the surface shear stress at the peak of the wave by a correlation of the form

$$\tau_{sp} = \tau_{sm} \left[\frac{h_p}{h_m}\right]^{\phi}$$

with $\phi \simeq 0.5$

However, he was unable to find a suitable value of ϕ which gave good agreement with the experimental results and yet did not predict a negative peak wall shear stress.

The three approaches described above are all based upon the principle of continuity of mass together with some other relation connecting the average film velocity under the crest of the wave $\bar{u}_p$ with the peak height h_p.

Miya (1970) followed Dressler and tried to construct a discontinuous solution of (2.37). He used as his shock relation the classical equation for a hydraulic jump:

$$h \left(\frac{q_o^2}{h^2} + \frac{gh}{2}\right)\Bigg|_{x=0^-}^{x=0^+} \qquad (2.39)$$

He found that his results were not in good agreement with experimental data.

(2.39) is not the correct shock condition. The appropriate dimensional steady wave form of (2.26), taking $\Gamma = 1$, is

$$- c(hu_a)_z + (hu_a^2)_z = \tau_s - \tau_w - ghh_x - \frac{h}{\rho_L}\frac{dp_G}{dz}$$

In Miya's analysis, τ_s, τ_w are functions of h

$$\text{while} \quad h\frac{dp_G}{dz} = \frac{d}{dz}\left\{\frac{B-2h}{2(B-h)^2}\right\}\rho_G\,(B-h_o)^2\,(U_G-c)^2 + K(h)$$

where K is a function of h.

The shock condition, derived by the author, then becomes

$$h\left\{\frac{q_o^2}{h^2} + \frac{gh}{2} - \frac{(B-2h)}{2(B-h)^2}\frac{\rho_G}{\rho_L}(B-h_o)^2\,(U_G-c)^2\right\}\Bigg|_{0^-}^{0^+} = 0$$

For $\frac{h}{B}$ small, neglecting $0\left(\frac{h^3}{B^3}\right)$, the relation between h_o and h_p is given by

$$h_r^3\left(\frac{1}{2}+\tilde{G}\right) - h_r\left(\frac{1}{2}+\tilde{G}+F^2\right) + F^2 = 0 \qquad (2.40)$$

where

$$\tilde{G} = \frac{1}{2B^3}\frac{\rho_G}{\rho_L}\frac{(B-h_o)^2\,(U_G-c)^2}{g}$$

$$F^2 = \frac{(c-u_o)}{\sqrt{gh_o}}$$

$$h_r = \frac{h_p}{h_o}$$

The solutions of (2.40) give slightly improved agreement with experiment. A comparison with the values calculated from (2.39) is given in Table 2.2.

Miya blamed the disagreement with experiment on the neglect of the drag at the gas-liquid interface. He considered a momentum balance over a length of liquid film L_f between the crest and base film and introduced

$$\tilde{T} = \frac{L_f(\overline{\tau_s-\tau_w})}{\rho g h_p{}^2}$$ where $(\overline{\tau_s-\tau_w})L_f$ is the measured net force acting on

on a unit width of film due to the gas drag. Again Miya failed to include the term due to the pressure gradient. The corrected equation for h_r is

$$h_r{}^3\left(\tilde{T}+\tilde{G}+\tfrac{1}{2}\right) - h_r\left(\tfrac{1}{2}+\tilde{G}+F^2\right) + F^2 = 0$$

The values of h_r calculated by the author from this equation are shown in Table 2.2. There is improved agreement with experiment.

CHAPTER 3. Turbulent Flow Over a Wavy Boundary

3.1 Turbulent Flow Models

Until the dynamics of turbulence are better understood, models of flows over waves will, of necessity, be highly speculative. There is still no mathematical model which can predict consistently and accurately the stresses exerted by a turbulent gas flow on a liquid wave. The abundance of research in this area has been motivated by the need for a model to explain the generation of ocean waves by wind. A good review of the various models which have been proposed is given by Barnett and Kenyon (1975).

The simplest model for the stress distribution along the surface of small amplitude waves is the classical Kelvin-Helmholtz model (see Lamb, p.462 (1932)). Turbulence is ignored and the gas is assumed to be inviscid and incompressible. The model predicts zero surface shear stress and a pressure distribution exactly 180^0 out of phase with the wave height. For sufficiently high gas velocities, the pressure distribution over the wave due to the Bemoulli effect causes infinitesimal wave growth. The theory predicts amplitudes of pressure variation which are too large and too high a minimum wind speed necessary to cause wave growth.

Another early model is Jeffrey's 'sheltering hypothesis' (1924). Turbulent wind blowing over a pre-existing wave crest is assumed to act like air blowing past a blunt body. Boundary layer 'separation' is assumed to occur on the down wind side of the wave crest with re-attachment occurring on the upwind face of the next crest. The resulting asymmetrical properties of the wind relative to the wave cause a pressure distribution which could feed energy into the wave, provided the wave is moving slower than the wind. Laboratory measurements of air flowing over stationary waves have shown that pressure forces produced by this means are too small for Jeffrey's theory to provide an effective wave generation mechanism.

Most of the research in this area in the last twenty years has been based on the linear 'quasi-laminar' theory of Miles (1957) and Benjamin (1959). This model is an improvement on the Kelvin-Helmholtz mechanism. The wind profile in the absence of waves is prescribed and is assumed to be produced by turbulent processes. Apart from determining the mean gas profile, all effects of the turbulence on the interaction between the two phases are neglected. The motion of the gas is taken to be laminar and incompressible. The wave slope is assumed to be small enough to justify neglecting non-linear terms. For solid or very slow moving waves, Benjamin showed that the thin friction layer close to the surface gives rise to a phase shift in the gas velocity. Consequently, the maximum in the velocity just outside the viscous wall layer does not occur at the wave crest. This causes a phase shift in the pressure profile from that predicted by the Kelvin-Helmholtz theory and a wall shear stress profile that has a maximum upstream of the wave crest. Although earlier comparisons of this theory with experimental results were encouraging, more recent observations have shown the growth rate of wind wave energy in the ocean to be much greater than could be accounted for by Miles' theory. The 'quasi-laminar' theory has tended to be more successful in laboratory conditions.

Recent research (e.g. Davis (1972), Townsend (1972)) has concentrated on improving the Miles/Benjamin theory by modelling the,previously ignored, turbulent Reynolds' stresses. As yet, no completely satisfactory model has resulted.

All the theories mentioned above, except for that of Jeffrey, require continuous flow above the wave surface. Gent and Taylor (1977), in numerical simulations of turbulent flow over solid waves, found that separation did not normally occur except over very short waves. Experimental work together with an analytic discussion indicated to Banner and Melville (1976) that air flowing over simple water waves should be less prone to separation than air-flow over solid boundaries including wavy walls. Indeed, if the usual kinematic and dynamic boundary conditions are satisfied, air-flow should not separate from the surface of a simple gravity wave. However, they found that the onset of wave breaking was sufficient to ensure the existence of air-flow separation.

3.2 Benjamin's Theory Applied to Vertical Annular Two-Phase Flow

In this thesis, the author decided to use Benjamin's linear 'quasi-laminar' theory for the calculation of the stresses exerted by the turbulent gas core on the liquid film in vertical annular two-phase flow. Evidence is given later in this section for the applicability of the theory to this flow system, and the belief that the derived stresses will at least have the right order of magnitude. Benjamin's theory has the advantage of leading to relatively simple analytic expressions for the stresses which can be incorporated easily into a stability analysis (see Chapter 4) or into the interfacial boundary conditions for a numerical simulation (see Chapter 7). This is in contrast to the more complicated models (e.g. Davis (1972), Townsend (1972)) which take account of the turbulent Reynolds stresses.

Consider the two dimensional flow of a semi-infinite gas stream over a solid wavy boundary $y = \eta_o e^{i\alpha(x-ct)}$. The real part of this expression corresponds to the physical boundary. Assume that the flow has a primary dimensional velocity profile U(y) which tends to some constant value U_o for large y. Then the perturbation pressure and tangential stress are of the form

$$p_s = \eta_o \ (\Pi_R + i\Pi_I)e^{i\alpha(x-ct)}$$

$$\tau_s = \eta_o \ (\Sigma_R + i\Sigma_I)e^{i\alpha(x-ct)}$$

where Π_R, Σ_R are in phase with the surface displacement and Π_I, Σ_I are in phase with the surface slope (see Fig. 3.1).

The normal stress acting upwards on the boundary is

$$N_s = -p + 2\rho\ \nu\ \alpha\ U'(0)\ i\eta_0 e^{i\alpha(x-ct)}$$

where the variable component of tangential velocity has been neglected. The second term in this expression is usually negligible in comparison with the first.

Benjamin introduces curvilinear co-ordinates with the surface as one of the co-ordinate lines:

$$\xi = x - i\eta_0 e^{-\alpha(y-ix)}$$

$$\eta = y - \eta_0 e^{-\alpha(y-ix)}$$

The disturbed flow is described by a perturbation representing the difference between the actual flow pattern and the pattern formed by bending the primary profile to follow the wave.

In his analysis terms of $O((\alpha\eta_0)^2)$ are neglected.

The stream function $\psi(\xi,\eta)$ is introduced and expressed in the form

$$\psi(\xi,\eta) = \psi_0(\eta) + \eta_0\ \{\ F(\eta) + [U(\eta)-c]\ e^{-\alpha\eta}\ \}\ e^{i\alpha\xi}$$

where ψ_0 is the stream function in the absence of waves. Substitution of this expression into the equations of motion leads to the Orr-Somerfeld equation

$$(U-c)\ (F'' - \alpha^2 F) - U''\ F = (i\alpha R_\lambda)^{-1}\ \{\ F^{iv} - 2\alpha^2 F'' + \alpha^4 F\ \}$$

where $R_\lambda = \frac{U_0}{\alpha\nu}$. $F(\eta)$ is then expressed in the form $\phi(\eta) + f(\eta)$ where $\phi(\eta)$ is the inviscid solution and $f(\eta)$ is rapidly decreasing with increasing η and is significant within the friction layer.

The perturbation stress coefficients can be expressed in the form

$$\Sigma = -R_\lambda^{-1} \{f''(0)/f(0)\}\ \phi(0)$$

$$\Pi = \alpha^2 \int_0^\infty (U-c)\ \phi\ d\eta$$

Π is affected by viscosity through the boundary conditions on ϕ which depend on $\frac{f'(0)}{f(0)}$.

Under certain assumptions $f(\eta)$ satisfies the equation

$$f^{iv} = i\ \alpha\ R_\lambda\ \{\eta\ U'(0) - c\}f''$$

$f(0)$, $f'(0)$, $f''(0)$ can be found by contour integration techniques.

The expressions for Π, Σ derived by Benjamin (1959) for flows over a rigid wavy boundary ($c = 0$) are

$$\Pi = -\ \rho U_0^2 \alpha I\ (1 - 1.288\ e^{\frac{\pi i}{6}}\ \Delta) \tag{3.1}$$

$$\Sigma = 1.372\ e^{\frac{\pi i}{3}}\ \rho U_0^2 \alpha K \tag{3.2}$$

where $\Delta = \dfrac{\alpha m U_0^2 I}{[U'(0)]^2}$ $\qquad K = \dfrac{\alpha I}{m}$ $\qquad m = \left(\dfrac{\alpha U'(0)}{\nu}\right)^{\frac{1}{3}}$

$$I = \int_0^\infty \left(\frac{U}{U_0}\right)^2 e^{-\alpha y}\ d(\alpha y).$$

The ratios of Σ_R, Σ_i to Π_R, Π_I are of order K/Δ which is generally much less than unity. In the limit R_λ $(= \frac{U_0}{\alpha\nu}) \to \infty$ the expressions (3.1), (3.2) yield the pressure distribution according to the Kelvin-Helmholtz theory.

The length scales in the problem are:

$2\pi/\alpha$ wavelength of disturbance

δ 'overall' boundary layer

δ^* width of region where most of the variation in U occurs

δ_L thickness of layer close to boundary

m^{-1} measure of the thickness of the wall friction layer where the influence of viscosity upon the perturbations is appreciable.

The conditions under which the expressions (3.1), (3.2) are valid are:

i $\alpha \delta R_\lambda >> 1$

ii $m >> \alpha$

iii $\alpha \delta_* << 1$

iv $\alpha \delta_1 \geqslant 0(1)$

v $\Delta << 1$

vi $U'' \ (0) = 0$

For a non rigid boundary with a small velocity c, the same results hold provided

vii $\dfrac{mc}{U'(0)} \leqslant 0(1)$

For larger c, the analysis is complicated by the existence of a critical layer in the gas phase at a significant distance from the boundary.

The above theory was originally developed for laminar flow. In order to apply it to turbulent flow it is necessary to adopt a 'quasi-laminar' turbulence model. In this model turbulence is neglected except inasmuch as it may determine relevant properties of the mean flow. Attention is focussed on the effects arising from disturbance on the boundary of the gas stream. The effect of the fluctuating velocity components in the flow is disregarded.

When the wavy boundary is not solid but is the interface between two fluids, there is an extra term in the stress formulae relating to the slipping of surface particles relative to their positions on the undisturbed plane. The formulae are still valid provided $U'(0) >> |\beta|$ where $\beta\eta_0 e^{i\alpha(x-ct)}$ is the tangential velocity perturbation at the fluid interface. This is generally true for air and water. In the case of turbulent flow, the turbulent fluctuations in one fluid will always be transmitted in some degree to the other. If the densities and viscosities of the two fluids are not much different, Reynolds' stresses will have a predominant effect on the interface. In this case, the viscous layer, necessarily assumed in Benjamin's theory will not occur. However, when the lower fluid is comparatively very viscous and dense, as in the case of air-water, it is reasonable to assume that the flow has a structure similar to one over a solid boundary, including a definite sublayer. Miles (1957), and, more recently, Wu (1968) and Stewart (1970) have indicated that, for the case of air and water, the main effect of turbulence in the water would appear to be only a slight roughening of the surface which can be accounted for theoretically by means of an 'equivalent roughness height'.

Thus the neglect of random surface stresses due to turbulence may be justified. However, additional systematic stresses resulting from the interaction of the wave and the turbulence may be appreciable. In particular, the components of stress which depend explicitly on viscosity may be overshadowed by the contribution due to turbulent interactions.

Benjamin's analysis assumes that no separation of the air flow occurs on the lee-ward side of the wave crest. As indicated in the last section, there is evidence that this condition holds for turbulent flow over long waves provided no breaking occurs. The results of the linearised analysis do lead to phase shifts in the shear stress and pressure profiles which have the same general character as if the flow had separated on the downstream side.

Although the expressions (3.1), (3.2) refer to a semi-infinite upper fluid, with slight modifications (see Craik (1966)) they also yield reasonable approximations in the case of (fully developed) turbulent flow in a finite channel of half height H. The extra condition

viii $\alpha H \geqslant 0\,(1)$

is necessary.

Outside the viscous sublayers near the boundaries where the velocity varies almost linearly, the velocity may often be well represented by the $^1/n^{th}$ power law where $n \simeq 7$.

$$\frac{U(y)}{U_o} = \left(\frac{y}{H}\right)^{1/n} \qquad \delta_1 < y < H$$

$$= \left(\frac{2H-y}{H}\right)^{1/n} \qquad H < y < 2H - \delta_1 \tag{3.3}$$

This choice of velocity profile requires that the viscous sublayers should occupy only a small fraction of the channel height, giving the additional constraint

ix $\delta_1 << H$

The factor I occurring in the expressions for the surface stresses is now given by

$$I = \int_o^H \left(\frac{y}{H}\right)^{2/n} e^{-\alpha y}\, d(\alpha y)$$

$$= \frac{\gamma\left(\frac{n+2}{n}, \xi\right)}{\xi^{\frac{2}{n}}}$$

where $\xi = \alpha H$ and $\gamma(n+1, \xi)$ denotes the incomplete gamma function

$\int_0^\infty x^n e^{-x}\, dx$. The corresponding integral for a boundary layer profile which obeys the $1/n^{th}$ power law for $y < H$ and which possesses the uniform velocity U_o for all $y \geqslant H$ is $I + e^{-\xi}$.

For $\xi > 6$, $\gamma\,(\frac{n+2}{n},\xi) \simeq \Gamma\,(\frac{n+2}{n})$. Thus a good approximation to the integral I is given by

$$I = \frac{\Gamma\,(\frac{n+2}{n})}{\xi^{\frac{2}{n}}}$$

For the case of turbulent flow in a finite channel, $\nu\, U'(0) = \frac{1}{2}\, C_f\, U_o^{\,2}$ where C_f is the friction coefficient at the interface. Following Benjamin (1959), the following measures of boundary layer thickness can be taken:

$$\delta_1 = \frac{10\nu}{U_o}\,(\frac{2}{C_f})^{\frac{1}{2}} \qquad \delta_* = \frac{2\nu}{C_f U_o} \qquad m = \left\{\frac{\alpha\, C_f U_o^{\,2}}{2\nu^2}\right\}^{\frac{1}{3}}$$

The validity conditions then become

i, $\quad R_\lambda >> \frac{1}{(\alpha H)^2}$

ii, $\quad R_\lambda^{\frac{2}{3}} >> C_f^{-\frac{1}{3}}$

iii, $\quad R_\lambda >> C_f^{-1}$

iv, $\quad R_\lambda^{\frac{1}{3}} \leqslant 10\,(\frac{C_f}{2})^{-\frac{1}{6}}$

v, $\quad R_\lambda^{\frac{4}{3}} >> I\, C_f^{-\frac{5}{3}}$

vi, $\quad \frac{c}{U_o} \leqslant (\frac{C_f}{2})^{\frac{2}{3}}\, R_\lambda^{\frac{1}{3}}$

vii, $\quad \alpha\, H \geqslant 0\,(1)$

viii, $\quad R_\lambda >> \frac{10}{\alpha H}\, C_f^{-\frac{1}{2}}$

Consider the case of vertical annular two-phase flow. Assume that all measurements are taken far enough up the tube for there to be a fully developed gas flow. The ratio of film thickness to tube radius is sufficiently small for the effects of curvature to be neglected.

For a typical flow situation based on the experimental conditions of Whalley et al.(1973) the magnitudes of the physical parameters are:

$$R_o = 1.59 \times 10^{-2} m$$
$$U_o \simeq 40 ms^{-1}$$
$$\rho \simeq 1.9\ kgm^{-3}$$
$$\nu \sim 10^{-5}\ Nsm^{-2}$$
$$C_f \sim 10^{-3}$$
$$\alpha \simeq 400 \text{ (corresponding to a 4\% wave slope)}$$
$$c \simeq 1 ms^{-1}$$
$$h_o \sim 10^{-4} m$$

Then $R_\lambda = \dfrac{U_o}{\alpha \nu} \sim 10^4$

The author has verified that the validity conditions are all satisfied.

From Hewitt and Hall-Taylor (1970), particularly in the ripple region, the gas velocity profile is well represented by (3.3) with n = 7. Thus for $\xi = \alpha\ R_o > 6$, $I \simeq \dfrac{0.9}{\xi^{\frac{2}{7}}}$

The extra term in the expression for the normal stress is given by

$$2\ \rho\ \nu\ \alpha\ U'(0) = 2\ \rho\ \alpha\ \tfrac{1}{2}\ C_f\ U_o^2$$

For this term to be negligible compared with the first term in the expression for the pressure

$$\rho \, \alpha \, C_f \, U_o^2 \ll I \, \rho \, U_o^2 \, \alpha^2$$

This implies $$C_f \ll I \, \rho \, \alpha$$

This condition is satisfied.

$$m \sim 2 \times 10^4$$

Thus the thickness of the wall friction layer, where the influence of viscosity upon the perturbation is appreciable, is of the same order as the film thickness.

$$\Delta = \frac{\alpha \, m \, U_o^2 \, I}{[U'(0)]^2} \sim 0.03$$

$$K = \frac{\Delta}{m} \sim 0.1$$

Thus the second, viscous term in the expression for the pressure is considerably smaller than the first term. However the effect of the perturbation tangential stresses is not negligible, as is generally true.

3.3 Benjamin's Theory Applied to Finite Amplitude Waves

To model the behaviour of large disturbance waves, it is necessary to be able to calculate the stress profiles over finite amplitude surface perturbations of arbitrary shape. Benjamin's results (3.1), (3.2) refer to a disturbance of the form $e^{i\alpha(x-ct)}$. However, since this is a linear theory, the expressions may be generalised by Fourier's theorem so as to apply when the boundary is an arbitrary perturbation from a plane.

If the deformation is of the form

$$y = \eta(x) = \frac{1}{\pi} \int_o^\infty \{g_1(\alpha) \cos \alpha x + g_2(\alpha) \sin \alpha x\} \, d\alpha$$

$$\text{where } g_1(\alpha) = \int_{-\infty}^{\infty} \eta(x) \cos \alpha x \, dx$$

$$g_2(\alpha) = \int_{-\infty}^{\infty} \eta(x) \sin \alpha x dx$$

then the stresses are given by

$$p_s = \frac{1}{\pi} \int_0^{\infty} \{g_1(\alpha) \, (\Pi_R(\alpha) \cos \alpha x - \Pi_I(\alpha) \sin \alpha x)$$

$$+ g_2(\alpha) \, (\Pi_R(\alpha) \sin \alpha x + \Pi_I(\alpha) \cos \alpha x)\} \, d\alpha$$

$$\tau_s = \frac{1}{\pi} \int_0^{\infty} \{g_1(\alpha) \, (\Sigma_R(\alpha) \cos \alpha x - \Sigma_I(\alpha) \sin \alpha x)$$

$$+ g_2(\alpha) \, (\Sigma_R(\alpha) \sin \alpha x + \Sigma_I(\alpha) \cos \alpha x) \quad d\alpha$$

Benjamin's theory is linear in $\alpha\eta_0$ and assumes a semi-infinite gas phase. In vertical annular flow, although disturbance waves can be up to five times the average film thickness, the ratio of wave amplitude to tube radius is still small. The maximum wave slope also tends not to be greater than a few per cent.

Benjamin's analysis assumes that no separation occurs on the leeward side of the wave crest. Separation seems more likely to occur for larger amplitude waves. However Miya (1970) found no evidence of separation in his experiments with disturbance waves in horizontal flow.

No direct experimental measurements have been made of the stress profiles over a water wave. However, there are a number of results concerning flow over solid waves. The gas flow behaviour over a solid wave will not be identical to that over a flexible surface, particularly a water wave. It is to be expected, however, that the behaviour in the two cases will show the same general trends. In particular it is hoped that the shear stress profile over the solid wave bears some resemblance to that over a water wave of the same shape.

Thorsness et al. (1978) compared Benjamin's theory with measurements of the variation in shear stress along a periodic solid wave. They came to the conclusion that, although a linear theory should be applicable for waves of small enough amplitude, the 'quasi-laminar' model gave large errors in the shear stress profile. They recommended that the range of applicability of the 'quasi-laminar' theory should be extended by means of a suitable mixing-length model. The difficulty with adopting such a model is that the simple analytical form of Benjamin's theory is lost and the surface stresses cannot be so easily incorporated into a numerical model of the film flow (see Chapter 7).

Miya (1970) measured the shear stress and pressure variations for the horizontal flow of water over a solid replica of a typical disturbance wave and also the wall shear stress and pressure variations for waves in the two-phase system.

The author calculated the shear stress and pressure profiles according to Benjamin's theory and compared them with Miya's measurements over the solid wave. A numerical package was developed which, when given the wave height at a number of unequally spaced points, calculated the stresses according to Benjamin's theory. The package was later incorporated into a SMAC program (see Chapter 7).

According to Benjamin's 'quasi-laminar' theory, given an infinitesimal disturbance of the form $e^{i\alpha x}$, the stresses exerted by the gas flow on the disturbance have leading terms (from section 3.2)

$$\tau_s = A\alpha^{\frac{29}{21}} e^{\frac{i\pi}{3}} e^{i\alpha x}$$

$$p_s = B\alpha^{\frac{5}{7}} e^{i\alpha x}$$

where A, B are suitable constants.

Generalising for an arbitrary profile $y = h(x')$ the stresses become

$$\tau_s = \sqrt{\frac{2}{\pi}} \int_0^\infty A\alpha^{\frac{29}{21}} \{g_1(\alpha) \cos(\alpha x + \tfrac{\pi}{3}) + g_2(\alpha) \sin(\alpha x + \tfrac{\pi}{3})\} \, d\alpha \tag{3.4}$$

$$p_s = \sqrt{\frac{2}{\pi}} \int_0^\infty B\alpha^{\frac{5}{7}} \{g_1(\alpha) \cos \alpha x + g_2(\alpha) \sin \alpha x\} \, d\alpha \tag{3.5}$$

$$\text{where } g_1(\alpha) = \frac{1}{\sqrt{2\pi}} \int_{-\infty}^{\infty} \cos \alpha x' \, (h(x') - h_0) \, dx'$$

$$g_2(\alpha) = \frac{1}{\sqrt{2\pi}} \int_{-\infty}^{\infty} \sin \alpha x' \, (h(x') - h_0) \, dx'$$

The author's earlier, unsuccessful attempts to calculate the stresses used a Fast Fourier Transform numerical package. $g_1(\alpha)$, $g_2(\alpha)$ were calculated, then substituted into (3.4), (3.5). Difficulties arose due to the very slow decay of the integrands in (3.4), (3.5). The method required specification of $h(x')$ at 4000 points; results were inaccurate and errors difficult to calculate.

An alternative approach uses the fact that

$$\frac{1}{\sqrt{2\pi}} \int_{-\infty}^{\infty} h_x e^{i\alpha x} \, dx = \left[\frac{1}{\sqrt{2\pi}} (h - h_0) e^{i\alpha x} \right]_{-\infty}^{\infty}$$

$$- \frac{i\alpha}{\sqrt{2\pi}} \int_{-\infty}^{\infty} (h - h_o) e^{i\alpha x} \, dx$$

$$= - i\alpha \left[g_1(\alpha) + i g_2 (\alpha) \right]$$

Similarly

$$\frac{1}{\sqrt{2\pi}} \int_{-\infty}^{\infty} h_{xx} e^{i\alpha x} \, dx = - \alpha^2 \left[g_1(\alpha) + i g_2(\alpha) \right]$$

It has been assumed that $h - h_o$, $h_x \to 0$ as $x \to \pm \infty$.

Then $\tau_s = A\sqrt{\frac{2}{\pi}} \int_0^{\infty} \alpha^{\frac{29}{21}} \{ g_1(\alpha) \cos(\alpha x + \frac{\pi}{3}) + g_2(\alpha) \sin(\alpha x + \frac{\pi}{3}) \} \, d\alpha$

$$= \frac{A}{\pi} \int_0^{\infty} - \alpha^{-\frac{13}{21}} \cos\,(\alpha x + \tfrac{\pi}{3}) \int_{-\infty}^{\infty} h_{x'x'} \cos \alpha x' \, dx' \, d\alpha$$

$$- \frac{A}{\pi} \int_0^{\infty} \alpha^{-\frac{13}{21}} \sin\,(\alpha x + \tfrac{\pi}{3}) \int_{-\infty}^{\infty} h_{x'x'} \sin \alpha x' \, dx' \, d\alpha$$

$$= A \int_{-\infty}^{\infty} h_{x'x'} \, I_1 \, (x - x') \, dx' \qquad (3.6)$$

where $\quad I_1(x) = - \frac{1}{\pi} \int_0^{\infty} \alpha^{-\frac{13}{21}} \cos\,(\alpha x + \frac{\pi}{3}) \, d\alpha$

$$= |x|^{-\frac{8}{21}} \{ -\tfrac{1}{4} \left[\Gamma \left(\tfrac{13}{21}\right) \right]^{-1} \sec \left(\tfrac{13\pi}{42}\right)$$

$$+ \frac{1}{\pi} \operatorname{sgn} x \, \Gamma \left(\tfrac{8}{21}\right) \cos \left(\tfrac{13\pi}{42}\right) \tfrac{\sqrt{3}}{2} \} \qquad (3.7)$$

Similarly $$p_s = B \int_{-\infty}^{\infty} h_{x'} I_2 (x-x') \, dx' \tag{3.8}$$

where $$I_2(x) = \frac{1}{\pi} \int_0^{\infty} \alpha^{-\frac{2}{7}} \sin kx \, d\alpha$$

$$= \frac{1}{\pi} |x|^{-\frac{5}{7}} \Gamma\left(\frac{5}{7}\right) \cos \frac{\pi}{7} \operatorname{sgn} x \tag{3.9}$$

The integrands in (3.6), (3.8) have integrable singularities provided h_x, h_{xx} are well behaved especially as $x \to \pm \infty$.

In the numerical integration procedure, the limits $(-\infty,\infty)$ were replaced by finite limits $(-R, +S)$ where the new interval included all the wave. Values $(x_i, h(x_i))$ obtained from a table given in Miya (1970) were provided as data. The derivatives $h'(x_i)$, $h''(x_i)$ were calculated using five point finite difference formulae.

Initially the integrals were calculated for each node point using the Harwell routine QA05AD for integrands with integrable singularities. The time taken (0.65 minutes for forty node points) was too great for the routine to be incorporated into a larger program. The C.P.U. time was reduced drastically (to 1.5 seconds) by the use of a numerical method described in Green (1969) p.111.

Consider the integral

$$\phi(x) = \int_a^b f(t) \, I(x-t) \, dt \tag{3.10}$$

where $I(x)$ has a singularity in $[a,b]$ and $f(t)$ is bounded. $[a,b]$ is partitioned into $t_o, \ldots, t_n$ with $t_j - t_{j-1} = h_j$. In (t_{j-1}, t_j), $f(t)$ is replaced by $\frac{1}{h_j} \left[(t_j - t) f(t_{j-1}) + (t - t_{j-1}) f(t_j)\right]$

Then $$\phi(x) = \sum_{j=1}^{n} (\alpha_j f(t_{j-1}) + \beta f(t_j))$$

where
$$\alpha_j = \frac{1}{h_j} \int_{t_{j-1}}^{t_j} (t_j - t)\, I(x-t)\, dt$$

$$\beta_j = \frac{1}{h_j} \int_{t_{j-1}}^{t_j} (t - t_j)\, I(x-t)\, dt$$

and can be calculated explicitly.

The above method was used to calculate the integrals (3.6), (3.7), putting f(t) equal to h" (t), h'(t) and I(t) equal to $I_1(t)$, $I_2(t)$ respectively.

Figs. (3.2), (3.3) show comparisons between the calculated stress profiles and Miya's experimental results. The channel used had a depth of 2.54×10^{-2}m. The maximum height of the wave was 3.23×10^{-3}m. The coefficients of the perturbation shear stress and pressure were given by

$$A = 3.172\, U_o^{\,2}\, \tau_{so}^{\,-\frac{1}{3}}$$

$$B = 2.570 \times 10^3\, U_o^{\,2}$$

The parameter τ_{so} in the expression for A was taken to be the experimental value at some distance from the wave. The pressure profile was calculated taking into account the experimental constant component of $\frac{dp}{dx}$.

From Fig. (3.2), there is reasonable agreement between the theoretical predictions for the shear stress and the experimental results. Both curves show a sudden relaxation of the shear stress at the front of the solid wave and also a definite phase shift in τ_s. Such behaviour cannot be predicted by Miya's theory (section 2.9) in which $\tau_s(x)$ is a unique function of h(x). However, the predicted τ_s on the back of the wave is less than the experimental value.

The agreement between the calculated and experimental pressure profiles is less encouraging. Fig. (3.3) also shows Miya's pressure profile calculated according to 'shallow-water' theory. This profile agrees more closely with the experimental results than does the profile calculated according to Benjamin's theory. This may be due to the maximum ratio of the height of the wave to the channel depth being as large as 0.13. The speed of the fluid would be expected to increase significantly above the crest of the wave. Account of the resulting pressure decrease is taken when calculating the Miya profile but not the Benjamin profile. In the case of vertical annular two-phase flow, this ratio is only about 0.03.

There are other factors which could help to account for the discrepancies between the theoretical and experimental results. Water was used as the fluid in the experiments and the validity conditions given in section 3.1 are not well satisfied. Also, the calculated profiles depend crucially on the given values of $h(x_n)$ which may not be accurate.

On considering all the evidence presented in this Chapter, the author decided that, at least as a first approximation, it would be suitable to use Benjamin's theory for the calculation of interfacial perturbation stress profiles in a mathematical model of disturbance waves in vertical annular two-phase flow.

CHAPTER 4. Stability Analysis and Wave Inception

4.1 Experimental Results for Wave Inception

In annular two-phase flow, if the gas flow-rate is fixed and the liquid flow-rate is gradually increased, there is a certain reproducible critical flow-rate below which the surface is covered with small ripples. Above this transition liquid flow-rate large disturbance waves appear. This feature is common to both upward and downward vertical flow and also horizontal flow.

Disturbance wave inception has been studied experimentally by a number of research workers (see Hewitt and Hall-Taylor (1970) for references).

The most comprehensive set of experiments for vertical upwards flow was carried out by Hall-Taylor (1966). He used a column of diameter 2.54×10^{-2}m and water (or an aqueous solution) and air.

Hall-Taylor found that at high gas flow rates, transition was clearly defined and reproducible. At low gas flow rates, however, it was more difficult to distinguish between large ripples and disturbance waves.

The wave inception curve was determined for air and four solutions of sucrose and water. The viscosity of the solutions was measured continuously throughout the experiments using a Ferranti viscometer. Surface tension was determined by capillary rise. The results are shown in Fig. (4.1). There is a definite effect of viscosity upon inception. This is contrary to observations made by Shearer (1964).

Teepol was added in order to discover the effect of a surface active agent on wave inception. This reduced the surface tension to 3.5×10^{-2} Nm^{-1}. The critical value of Re_L was slightly increased by the addition of teepol. It might be expected that reducing the surface tension would make the interface more unstable and consequently cause wave inception at a lower liquid Reynolds number. However, when surface agents are used, they involve additional effects of surface viscosity and variation in concentration of surface active agent with position on the interface. All these factors could affect wave inception.

There was good agreement between Hall-Taylor's results and those of Shearer (1964) for a 3.18×10^{-2}m diameter tube. Shearer's results for a 1.59×10^{-2}m diameter tube gave slightly lower critical values of Re_L for wave inception. Hall-Taylor postulated the following explanations for this:

1. There may be a genuine effect of diameter.
2. The results may be due to slight differences in viscosity.
3. It may be easier to detect disturbance waves in smaller diameter tubes.

A general feature of wave inception curves for vertical flow is that for low gas flow-rates the transition Re_L increases with increasing Re_G. For higher flow-rates ($Re_G \geqslant 10^5$), the transition Re_L is almost independent of Re_G, the asymptotic value being about 75.

More recent experimental results for vertical flow are due to Whalley et al. (1977). They developed a method for producing single disturbance waves. The liquid flow-rate was artificially increased above the critical value for a short time by injecting water from a hypodermic syringe near the sinter. They confirmed the general form of the wave inception curve for low Re_G found by Hall-Taylor.

In fig. 4.2, the results for vertical flow are compared with the experimental results for wave inception in horizontal flow found by Hershman (1960), Woodmansee et al. (1969) and Miya (1970). The behaviour in the two cases is similar for high Re_G but markedly different for low Re_G. This suggests that at least for low Re_G, different mechanisms are responsible for wave inception.

Thwaites et al. (1976) investigated disturbance wave transition for vertical flow using a 3.18×10^{-2}m diameter tube. They compared the results obtained using water with those using a polymer drag reducing solution. The behaviour was similar for G_G less than 46.2 kg m^{-2} s^{-1}. For higher gas flow-rates, however, the transition liquid flow-rate was uniformly some 80% higher for the polymer. They also found that for G_G greater than 23 kgm^{-2} s^{-1}, the wave frequency was proportional to the gas velocity. Thwaites et al. stated that these observations supported the hypothesis that two separate mechanisms are involved at high and low gas flow-rates.

4.2 A Linear Stability Analysis

Most attempts at predicting disturbance wave inception have been based upon linear perturbation techniques. The criterion for disturbance wave inception is taken to be the onset of instability according to the linear theory. A stability analysis for vertical two-phase flow is described in this section. The approach adopted is similar to that of Craik (1966) and Hall-Taylor (1966). The assumptions made are such as to make the analysis particularly applicable to the experimental conditions of Whalley et al (1973).

The system is regarded as having an arbitrary small disturbance, the Fourier components of which are assumed to be dynamically independent. Since each Fourier component is a solution of the linearised equations of motion, it is sufficient to examine the behaviour of a general harmonic disturbance. Also, since every periodic three dimensional disturbance may be treated in terms of a corresponding two dimensional problem (Lin (1955) §§ 3.1, 5.2) only two dimensional disturbances need be considered.

Consider the upward vertical co-current flow of air and water (see fig. 2.1). On making the assumptions outlined in section 2.2, the system can be regarded as two dimensional with the non-dimensional velocity profile for the primary film flow given by equation (2.8):

$$\bar{u} = (T - \frac{G}{2}) + Ty + \frac{G}{2} y^2$$

where $$T = Re_L \bar{\tau}_s$$

$$G = \frac{g(1-\rho^*)\, h_o^{\,2}}{u_a \nu_L}$$

where $\bar{\tau}_s$ is the shear stress exerted by the gas on the undisturbed film and $\rho^* = \rho_G/\rho_L$.

Let the equation of the perturbed interface be given by

$$y = \eta(z,t) = \delta e^{ik(z-ct)}$$

where the non-dimensional wave number

$$k = \frac{2\pi h_o}{\lambda} \; (<<1), \;\; \delta<<1$$

and $c = c_R + ic_I$

The normal and tangential perturbation stresses exerted by the gas on such a disturbance (N'_s, τ'_s respectively) are assumed to have been determined. The problem is to find expressions for c_R, c_I in terms of k and known quantities.

Denoting perturbation quantities by ', the linearised perturbation equations for the liquid flow are given by

continuity $$\frac{\partial u'}{\partial z} + \frac{\partial v'}{\partial y} = 0 \qquad (4.1)$$

Navier Stokes $$\frac{\partial u'}{\partial t} + \bar{u}\frac{\partial u'}{\partial z} + v'\frac{\partial \bar{u}}{\partial y} = -\frac{\partial p'}{\partial z} + \frac{1}{Re_L}\left\{\frac{\partial^2 u'}{\partial z^2} + \frac{\partial^2 u'}{\partial y^2}\right\} \qquad (4.2)$$

$$\frac{\partial v'}{\partial t} + \bar{u}\frac{\partial v'}{\partial z} = -\frac{\partial p'}{\partial y} + \frac{1}{Re_L}\left\{\frac{\partial^2 v'}{\partial z^2} + \frac{\partial^2 v'}{\partial y^2}\right\} \qquad (4.3)$$

together with the following boundary conditions:

1. perturbation velocities vanish at the wall

$$u' = 0 = v' \qquad y = -1 \qquad (4.4)$$

$$v' = \frac{\partial \eta}{\partial t} + \bar{u}\frac{\partial \eta}{\partial z} \qquad y = 0 \tag{4.5}$$

3. continuity of normal stress at interface

$$-p' + \frac{2}{Re_L}\{-\frac{d\bar{u}}{dy}\frac{\partial \eta}{\partial z} + \frac{\partial v'}{\partial y}\} = N_s' - W\frac{\partial^2 \eta}{\partial z^2} \tag{4.6}$$

4. continuity of tangential stress at interface

$$\frac{1}{Re_L}\{\frac{d^2\bar{u}}{dy^2}\eta + \frac{\partial v'}{\partial z} + \frac{\partial u'}{\partial y}\} \simeq \tau_s' \qquad y = 0 \tag{4.7}$$

where $$W = \frac{\sigma}{\rho_L u_a^2 h_o} = [\text{Weber no}]^{-1}$$

(4.1) is satisfied by introducing a perturbation stream function

$$\psi(z,y,t) = -\phi(y)\eta(z,t)$$

so that the perturbation velocity components are given by

$$u' = \frac{\partial \psi}{\partial y} = -D\phi\eta \qquad v' = -\frac{\partial \psi}{\partial z} = ik\phi\eta$$

where D denotes differentiation with respect to y.

Substituting for u', v' in (4.2), (4.3) gives respectively

$$p' = \{-(c-\bar{u})D\phi - D\bar{u}\phi + \frac{1}{ikRe_L}[k^2 D\phi - D^3\phi]\}\eta \tag{4.8}$$

$$\frac{\partial p'}{\partial y} = \{-(c-\bar{u})k^2\phi + \frac{1}{Re_L}(ikD^2\phi - ik^3\phi)\}\eta \tag{4.9}$$

Eliminating p' between (4.8) and (4.9) gives

$$D^4\phi - 2k^2 D\phi + k^4\phi = (ikRe_L)\{(\bar{u}-c)(D^2\phi - k^2\phi) - D^2\bar{u}\phi\} \tag{4.10}$$

This is the Orr-Somerfeld equation.

Substituting for u', v' in the boundary conditions (4.4)-(4.7) gives respectively

$$D\phi = 0 = \phi \qquad y = -1$$

$$\phi = \bar{u} - c \qquad y = 0 \qquad (4.11)$$

$$T_s' = -(D^2\phi + k^2\phi - D^2\bar{u})\eta \qquad y = 0 \qquad (4.12)$$

where $T_s' = \tau_s' \, Re_L$.

$$N_s' + k^2 W\eta = -\frac{2ik}{Re_L} D\bar{u}\eta + \frac{2ik}{Re_L} D\phi\eta - p' \qquad y = 0 \qquad (4.13)$$

Putting $N_s' = -\Pi\eta$, $T_s' = \Sigma\eta$ and using (4.8), (4.11) reduces (4.12), (4.13) to, respectively

$$D^2\phi + k^2\phi - \frac{(\Sigma - D^2\bar{u})}{c - \bar{u}}\phi = 0$$

$$kRe_L \{D\bar{u} + (\frac{-k^2W-\Pi}{c-\bar{u}})\}\phi + 2ik^2 D\bar{u}\phi + k(Re_L(c-\bar{u}) + 3ki) D\phi - iD^3\phi = 0$$

Thus the stability problem reduces to solving the Orr-Somerfeld equation (4.10) subject to the boundary conditions

$$D\phi = 0 = \phi \qquad y = -1$$

$$\phi = \bar{u} - c \qquad y = 0$$

$$D^2\phi + k^2\phi - (\frac{\Sigma - D^2\bar{u}}{c-\bar{u}})\phi = 0 \qquad y = 0$$

$$(kRe_L)\{D\bar{u} + (\frac{-k^2W-\Pi}{c-\bar{u}})\}\phi + 2ik^2D\bar{u}\phi + k\,[Re_L(c-\bar{u}) + 3ki]\,D\phi - iD^3\phi = 0$$

Consider the case where the primary velocity profile can be expressed in the form

$$\bar{u} = u_o + u_1 y + \frac{u_2}{2} y^2 + y^3 f(y)$$

where f is a polynomial in y.

Let $c' = c - u_o$

Then the problem reduces to

$$\left.\begin{aligned}
&D^4\phi - 2k^2D\phi + k^4\phi = (ikRe_L)\{(u_1 y + u_2 y^2 + y^3 f(y) - c') \\
&\qquad \times (D^2\phi - k^2\phi) - (u_2 + (y^3 f)_{yy})\phi\}
\end{aligned}\right.$$

subject to

$$\left.\begin{aligned}
&D\phi = 0 = \phi && y = -1 \\
&\phi = -c' && y = 0 \\
&D^2\phi - \left(\frac{\Sigma - u_2}{c'}\right)\phi = 0 && y = 0 \\
&kRe_L \{u_1 + \left(\frac{-k^2W - \Pi}{c'}\right)\}\phi + \frac{2ik^2u_1}{c'}\phi \\
&\quad + k(Re_L c' + 3ki)D\phi - iD^3\phi = 0 && y = 0
\end{aligned}\right\} \quad (4.14)$$

The Orr-Somerfeld equation together with these boundary conditions cannot be solved exactly analytically. A solution has to be found either by means of a series expansion in terms of a small parameter or by a numerical method (see Appendix 2).

4.3 Series Solution to the Orr-Somerfeld Equation

There are a number of methods described in the literature for obtaining series solutions to the Orr-Somerfeld equation. These are mostly derived for single phase liquid flow down an inclined plane but can easily be adapted for use in the present case. A good review of the various methods is given by Solesio (1977).

In the ripple and transition regions for vertical upwards flow, $Re_L < 10^2$. Also it is to be expected that the most unstable perturbations will occur for the case of long waves ($k \ll 1$) where the stabilising effect of surface tension is less pronounced. Finally, the derivation of the expressions for the perturbation gas stresses by means of Benjamin's theory is only valid for $k \ll 1$. Taking all these factors into account, the most suitable approach appears to be a series expansion for the solution in terms of powers of kRe_L. The method described in this section is due to Yih (1963) and follows that given by Hall-Taylor (1966) for two-phase flow. It requires the assumptions that both $k \ll 1$ and $kRe_L \ll 1$.

Consider the case of long waves where $kRe_L \ll 1$. On neglecting terms of $O(k^2)$ and expanding both ϕ and c' in powers of $\varepsilon = kRe_L$, the equations (4.14) reduce to

$$D^4\phi = i\varepsilon \{(-c' + u_1 y + \frac{u_2}{2} y^2 + y^3 f)D^2\phi - (u_2 + (y_3 f)_{yy})\phi\}$$

subject to

$$D\phi = 0 = \phi \qquad y = -1$$

$$\phi = -c' \qquad y = 0$$

$$D^2\phi - \frac{(\Sigma - u_2)\phi}{c'} = 0 \qquad y = 0$$

$$\varepsilon \{ u_1 + (\frac{-k^2 W - \Pi}{c'})\}\phi + \varepsilon c' D\phi - iD^3\phi = 0 \qquad y = 0$$

where
$$\phi = \phi_o + \varepsilon\phi_1 + \dots\dots$$

$$c' + c_o' + \varepsilon c_1' + \dots\dots$$

The lowest order equations are

$$D^4\phi_0 = 0$$

$$D\,\phi_0 = 0 = \phi_0 \qquad y = -1$$

$$\phi_0 = -c_0' \qquad y = 0$$

$$D^2\phi_0 - \frac{(\Sigma-u_2)\phi_0}{c_0'} = 0 \qquad y = 0$$

$$D^3\phi_0 = 0 \qquad y = 0$$

These have the solution $\phi_0 = -c_0'\ (1 + y)^2$

where $$c_0' = \tfrac{1}{2}\ (\Sigma-u_2).$$

The next order Orr-Somerfeld equation is

$$D^4\phi_i = i\ \{-c_0' + u_1 y + \frac{u_2}{2}y^2 + y^3 f)(-2c_0')$$
$$+ (u_2 + (y^3 f)_{yy})c_0'(1+y)^2\}$$

Write $$f = \frac{1}{6}u_3 + yF(y) \qquad \Phi_1 = \frac{\phi_1}{c_0'}$$

Then

$$D^4\ \Phi_1 = i\ \{(2c_0' + u_2) + (2u_2 - 2u_1 + u_3)y + D^4[g(y)y^6]\ \} \qquad (4.15)$$

where $$D^4[g(y)y^6] = -\frac{1}{3}u_3 y^3 - 2y^4 F + [y^4 F(y)]_{yy}\ (1 + y)^2 \qquad (4.16)$$

The boundary conditions become

$$D\Phi_1 = 0 = \Phi_1 \qquad y = -1$$

$$\Phi_1 = -\frac{c_1'}{c_0'} \qquad y = 0$$

$$D^2\Phi_1 - (\frac{\Sigma - u_2}{c_0'})\Phi_1 = (\frac{\Sigma - u_2}{c_0'^2})c_1' \qquad y = 0$$

$$D^3\Phi_1 = i(u_1 + (\frac{-k^2W-\Pi}{c_o'}) + 2ic_o' \qquad y = 0$$

The general solution of (4.15) is

$$\Phi_1 = \frac{i\Sigma}{24} y^4 + \frac{i}{120} (2u_2 - 2u_1 + u_3)y^5 + iy^6 g(y)$$

$$+ A_1 + B_1 y + C_1 y2 + D_1 y3 \qquad (4.17)$$

Using the boundary conditions to eliminate

$A_1 - D_1$ gives finally

$$c_1' = \{\frac{2}{15} i(u_1 - u_2) + \frac{iu_2u_3}{60} + \frac{i5\Sigma}{24} + i\frac{(-k^2W-\Pi)}{3(\Sigma-u_2)}\}(\Sigma - u_2) \qquad (4.18)$$

This is equivalent to the result derived by Hall-Taylor (1966). From here on, the author's treatment of the problem differs from that of Hall-Taylor.

In the above expression, non-linear terms appear in what is supposedly a linear theory. Also $\frac{\Sigma}{2}R$ appears in the lowest order term in c_R. These facts suggest that Σ should be of smaller magnitude than O(1). If the stresses are calculated using Benjamin's theory (see Chapter 3), the tangential perturbation stress is indeed much smaller than the normal stress.

Taking $\Sigma = O(\varepsilon)$ gives

$$\left.\begin{aligned} c' &= -\tfrac{1}{2}u_2 + \varepsilon\{\frac{\Sigma}{2\varepsilon} - \frac{i2}{15} u_2(u_1-u_2) - i\frac{u_2u_3}{60} + i(\frac{-k^2W-\Pi}{3})\} \\ c &= (u_o-\tfrac{1}{2}u_2) + \varepsilon\{\frac{\Sigma}{2\varepsilon} - i\frac{2u_2}{15}(u_1-u_2) - i\frac{u_2u_3}{60} + i(\frac{-k^2W-\Pi}{3})\} \end{aligned}\right\} \quad (4.19)$$

Equating real and imaginary parts gives

$$\left.\begin{aligned} c_R &= u_o - \tfrac{1}{2}u_2 + \varepsilon\left\{\frac{\Sigma_R}{2\varepsilon} + \frac{\Pi_I}{3}\right\} \\ c_I &= \varepsilon\left\{\frac{\Sigma_I}{2\varepsilon} - \frac{2}{15}u_2(u_1-u_2) - \frac{u_2u_3}{60} + \left(\frac{-\Pi_R - k^2W}{3}\right)\right\} \end{aligned}\right\} \quad (4.20)$$

To the first order in ε, c depends only on the first three coefficients in a power series expansion of the primary velocity profile.

For upward vertical annular flow with laminar film flow

$$\bar{u} = (T - \frac{G}{2}) + Ty + \frac{G}{2}y^2$$

$$= \tfrac{1}{4}(T+6) + T_{\text{,}}y + \tfrac{3}{4}(T-2)y^2$$

where $2 \leqslant T \leqslant 6$

From (4.20)

$$c_R = 3 - \tfrac{1}{2}T_y + \varepsilon\left\{\frac{\Sigma_R}{2\varepsilon} + \frac{\Pi_I}{3}\right\}$$

$$c_I = \varepsilon\left\{\frac{\Sigma_I}{2\varepsilon} - \frac{1}{10}(T-2)(6-T) - \frac{Wk^2}{3} - \frac{\Pi_R}{3}\right\}$$

In the above expression for c_I, the term $\frac{1}{10}(T-2)(6-T)$ is always greater than or equal to zero and has a stabilising effect like surface tension. The term vanishes in the two extremes of shear flow and the lower limit of co-current flow. It is largest when T = G = 3. This corresponds to the point of zero wall shear stress.

4.4 Connection Between Stability Analysis and Wave Inception

In this section, the asymptotic expressions derived for c_R, c_I for small kRe_L, together with the use of Benjamin's theory for the perturbation stresses, will be examined in an attempt to predict disturbance wave inception.

Difficulties associated with such an approach include

1. The liquid flow is assumed to be laminar. This is a doubtful assumption (see section 2.2).

2. Although it is to be hoped that Benjamin's theory describes qualitatively the form of the perturbation stresses, as pointed out in Chapter 3, it is unlikely to give accurate quantitative results.

3. The asymptotic expressions (4.20) are only valid for $\varepsilon = kRe_L << 1$. Again, it is to be hoped that they will still describe the correct behaviour qualitatively beyond the strict range of their validity.

The case of vertical downflow is simpler than that of vertical upflow and will be considered first. In the notation of the previous section, the velocity profile is given by

$$\bar{u} = (T+\frac{G}{2}) + Ty - \frac{G}{2}y^2$$

The two extremes of this flow are given by

$G = 3 \quad T = 0$ (free fall) (also $\Sigma = \Pi = 0$)

$T = 2 \quad G = 0$ (shear flow)

Free fall was analysed by Benjamin (1957). The expressions for the real and imaginary parts of c are:

$$c_R = 3$$

$$c_I = \varepsilon \{\frac{6}{5} - \frac{k^2W}{3}\}$$

The different numerical factors in Benjamin's expressions are due to his non-dimensionalisation of the flow variables with respect to the surface rather than the average film velocity. Surface waves will travel with a speed of twice that of the surface. The surface will always be unstable for sufficiently small values of k. It is reasonable to suppose that the wave most prominent in experiments corresponds to the one with the largest growth rate according to the linear theory and that waves with this wave number tend to suppress the other waves. The most unstable wave number k_m maximises $kc_I(k)$. The corresponding amplification experienced by

$$A = \exp \{\frac{k_m}{h_o} \frac{(c_I)_m}{c_R}\} = \exp (BRe_L^{\frac{1}{3}})$$

where B is a constant. This expression blows up for Re_L greater than 3 or 4. Benjamin proposed this result to explain the experimental observation of a critical Reynolds number of about 3 or 4, below which no waves were observed.

In the case of shear flow, the expressions for the real and imaginary parts of c become

$$c_R = 2 + \varepsilon \{ \frac{\Sigma_R}{3} + \frac{\Pi_I}{3} \}$$

$$c_I = \varepsilon \{ \frac{\Sigma_I}{2\varepsilon} - \frac{\Pi_R}{3} - \frac{k^2 W}{3} \}$$

The surface will again be unstable for sufficiently long wave-lengths. Since $\Sigma_R>0$ and $\Pi_I>0$ from (3.1), (3.2), the wave speed will be slightly greater than the film surface. Proceeding in the same way as for free fall, Benjamin's expressions for the perturbation stresses give

$$k_m = U_G Re_L^{\frac{9}{14}} U_G^{-\frac{2}{7}} \; 2.59 \times 10^{-3}$$

The above results predict the different behaviour of the film surface for low and high gas flow rates as found experimentally by Thwaites et al. (1976). For high gas flow-rates, the predicted wave number k_m does appear to have the correct order of magnitude and also increases roughly in proportion to U_G as observed. However, the theoretical results cannot explain the experimental result that no waves are observed for liquid Reynolds numbers below 50.

Now consider the case of vertical upflow. This is complicated by the second stabilising term in the expression for c_I. The asymptotic expression for c can be written (in dimensional form):

$$c_R = u(0) - \frac{gh^2}{2\nu_L} + \Sigma_R \frac{h^2}{2\mu_L} + \alpha\Pi_I \frac{h^3}{3\mu_L} \tag{4.21}$$

$$c_I = \Sigma_I \frac{h^2}{2\mu_L} - \alpha(\Gamma\alpha^2 + \Pi_R) \frac{h^3}{2\mu_L} - \frac{2\alpha g}{15\nu_L^2} \left(\frac{\tau_{so}}{\mu_L} - \frac{\rho g h}{\mu_L}\right) h^5 \tag{4.22}$$

According to Benjamin's theory (Chapter 3), the perturbation stresses are given by

$$\left.\begin{aligned} \Pi &= - \rho_G U_G^2 I_o \alpha^{\frac{5}{7}} \left(1 - 1.288 e^{\frac{\pi i}{6}} \Delta_o \alpha^{\frac{22}{21}}\right) \\ \Sigma &= 1.372\, e^{\frac{\pi i}{3}} \rho_G U_G^2 \frac{I_o}{m_o} \alpha^{\frac{29}{21}} \end{aligned}\right\} \tag{4.23}$$

where $\qquad I_o = \dfrac{0.9}{R_o^{\frac{2}{7}}} \qquad m_o = \left(\dfrac{C_f U_G^2}{2\nu_G^2}\right)^{\frac{1}{3}}$

$$\Delta_o = m_o U_G^2 I_o \left(\frac{2\nu G}{C_f U_G^2}\right)^2$$

For very high gas flow rates the expressions (4.21), (4.22) tend to those for downwards shear flow.

Since the terms involving Σ_R, Π_I in (4.21) are small (see Chapter 3), the asymptotic expression for the infinitesimal wave speed is generally slightly less than the surface speed. This result depends neither on the precise expressions adopted for the surface stresses nor on the form of the primary velocity profile. In contrast, Hall-Taylor (1966), who used different expressions for the perturbation stresses, found c_R to be about one and a half times u(0). From Benjamin's theory (4.23) $\Pi_I << \Pi_R$. As $\nu_G \to 0$, $\Pi_I \to 0$ and Π_R tends to the inviscid Kelvin-Helmholtz form as expected. Hall-Taylor's expressions (his (6.81), (6.82)) give $\Pi_I = -0.58\Pi_R$ and thus do not have this property. It is the O(1) value of Π_I which leads to Hall-Taylor's larger infinitesimal wave speed.

The neutral stability curves for $G_G = 63.4$ kgm^{-2}s^{-1}, 31.7 kgm^{-2}s^{-1} are shown in Figs. 4.3, 4.4 as functions of h_o and $k = \alpha h_o$ together with the curves of maximum instability.

The film surface is always unstable for suitable values of k. The author cannot explain, from linear stability considerations, why there should be a critical value of the liquid flow rate for disturbance wave transition.

From the stability curves, the ripple frequency should increase with increasing gas flow rate, and also with increasing h_o and hence liquid flow rate. This is observed in experiments.

In the linear stability analysis in section 4.3, it was assumed that the unperturbed surface was smooth and the primary velocity profile was calculated accordingly. It is believed that the effect of ripples on the liquid surface is to present a rough wall to the gas flow. Experimental measurements (see Chapter 5 and Shearer (1964)) indicate that the surface roughness increases with film thickness. If this effect is included in the analysis for high gas velocities, the qualitative behaviour is little altered. For low gas flow rates, however, the situation is very different. If the effect of the ripples on the surface roughness is neglected, the maximum liquid flow rate which the gas flow can maintain is considerably less than the observed transition flow rate. Thus the ripples have a marked effect on the film velocity profile and the applicability of the linear stability analysis is questionable.

Miya (1970) tried to overcome the problems connected with the ripples in the case of horizontal flow by assuming a turbulent velocity profile and a friction coefficient based on experimental measurements at the critical flow rate. His analysis was based upon the linearised form of the integral equations (2.25), (2.26). The shear stress profile was calculated by making the 'self-similarity' assumption (see section 2.8) and was thus in phase with the disturbance. The condition of neutral stability was used as a criterion for wave inception. There was good agreement between the calculated values and the experimental data of Miya and also those of Hershman (1960) and Woodmansee (1968) for $Re_L>200$. However, for $Re_L<200$, the linearised theory predicted a value for Re_G which was too low. Miya observed that for high gas flow rates, the nature of his roll waves was quite different than that for low gas flow rates. He postulated that for $Re_L<200$, the film flow was approximately laminar and that a different mechanism was involved.

Pashniak (1969) used Miya's analysis for vertical stream-water flow and obtained results agreeing with his experiments. The author has two criticisms of Pashniak's work. Firstly he is assuming a turbulent velocity profile in a region where $Re_L<100$. Secondly, for each value of Re_L he only considers stability with respect to a wave length of 1.27×10^{-2}m rather than for all values of the wave number. The point of neutral stability should be where $\max_k c_i(k) = 0$ and not where $c_i(k) = 0$ for some particular value of k.

From the linear theory, the infinitesimal wave speed for upward vertical flow is less than the surface speed. Experimentally the disturbance wave speed is always about three times the average film speed and hence greater than the surface speed.

From the evidence preserved in this section, it is the author's opinion that a linear stability analysis cannot predict disturbance wave inception.

4.5 Other Possible Explanations for Disturbance Wave Inception

Disturbance waves are observed to form very close to the inlet. Their frequency decreases with distance up the tube. If the waves were the result of the amplification of ripples, the author would expect new disturbance waves to continue to be formed some distance from the inlet. Thus disturbance wave inception may be connected in some way with the liquid behaviour at the inlet.

Assuming laminar film flow, the liquid mass flow rate is given by

$$G_L = \frac{u_a h_o}{X}$$

where
$$u_a = \frac{Th_o}{2} - \frac{2}{3} G h_o^2$$

$$X = \frac{R_o}{2\rho_L} \quad T = \frac{\tau_s}{\mu} \quad G = \frac{g}{2\nu_L}(1-\rho^*) = \frac{g^*}{2\nu_L}$$

The maximum liquid flow rate is given by

$$G_{LMAX} = 0.213\tau_s^3 \text{ for } h_o = \frac{T}{2G}$$

A possibility is that the transition liquid flow rate G_{LTR} equals G_{LMAX}. However, if τ_s is calculated assuming a smooth film $G_{LMAX} < G_{LTR}$ for low gas flow rates. For high gas flow rates, since G_{LTR} should increase like τ_s^3 (and hence $U_G^{\frac{23}{24}}$), there should not be the asymptotic limit observed experimentally. If τ_s is taken to depend on h_o according to the Shearer-Nedderman correlation (see section 5.3) then a maximum liquid flow rate is never achieved for any gas flow rate.

For low gas flow rates and liquid flow rates above G_{LMAX}, there is probably 'confusion' at the inlet. If the ripples do not form fast enough to provide sufficient surface roughness, and hence shear stress, to support the liquid flow rate, a bulge of liquid may develop. The author has examined a crude numerical model of injection with a porous sinter.

Assume that the liquid is injected at a constant rate V between $x = 0$ and $x = x_o$ and that the surface shear stress is independent of h. Then the continuity equation gives

$$h_t + (u_a h)_x - V = 0$$

Hence $$h_t + \left(\frac{\tau_s h}{\mu} - \frac{g^* h^2}{\nu}\right) \frac{\partial h}{\partial x} - V = 0 \qquad 0<x<x_o \qquad (4.24)$$

This has a steady solution (assuming h = 0, x = 0)

$$\left(\frac{\tau_s}{2\mu_L} - \frac{1}{3}\frac{g^* h}{\nu_L}\right)h^2 = \begin{cases} Vx & 0<x<x_o \\ Vx_o & x>x_o \end{cases} \qquad (4.25)$$

The value of V corresponding to G_{LMAX} is $\dfrac{\tau_s^3}{6\mu_L \rho_L^2 g^{*2} x_o}$

τ_s was taken to be 1.0 corresponding to $G_G \simeq 30\ kgm^{-2}s^{-1}$ and x_o was taken to be 0.1 (in experiments $x_o = 7.6 \times 10^{-2}$m).

A scaled form of (4.24) is

$$\frac{\partial \bar{h}}{\partial t} + (0.1\bar{h} - 0.097\bar{h}^2)\frac{\partial \bar{h}}{\partial x} - \chi\bar{V} = 0 \qquad (4.26)$$

where $$\chi = \begin{cases} 0 & x<0,\ x>0.1 \\ 1 & 0<x<0.1 \end{cases}$$

Equation (4.26) was solved using the following numerical technique for the general first order partial differential equation

$$\frac{\partial u}{\partial t} + \frac{\partial}{\partial x} g(u) + F[u] = 0 \qquad (4.27)$$

where F is some functional of u. A finite difference form of the equation was constructed using central space differences (index i) and a mixture of explicit and implicit time differencing (index h). (4.27) becomes

$$\frac{u_i^{n+1} - u_i^n}{\Delta t} = -\theta \frac{(g_{i+1}^{n+1} - g_{i-1}^{n+1})}{2\Delta x} - (1-\theta) \frac{(g_{i+1}^{n} - g_{i-1}^{n})}{2\Delta x}$$

$$+ F_i(u_i^n, \ldots, u_N^n) \tag{4.28}$$

where $\qquad g_i^{\,n} \equiv g(u_i^{\,n})$ etc.

(4.28) is to be solved for $u_i^{\,n+1}$ at each time step n.

Let $$u_i^p = u_i^n - \frac{(g_{i+1}^n - g_{i-1}^n)}{2\Delta x} \Delta t + F_i(u_1^n, \ldots, u_N^n) \tag{4.29}$$

$$\delta u_i \equiv u_i^{\,n+1} - u_i^p = -\theta \frac{(g_{i+1}^{n+1} - g_{i-1}^{n+1})}{2\Delta x} \Delta t$$

$$+ \theta \frac{(g_{i+1}^n - g^n{}_{i-1})}{2\Delta x} \Delta t$$

If u_i^{n+1} in the right-hand side of (4.29) is written in the form $u_i^p + \delta u_i$, the equation becomes a non-linear equation for δu_i of the form

$$0 = \tilde{F}_i(\delta u_1, \ldots, \delta u_N) \qquad i = 1, \ldots, N \tag{4.30}$$

This can be solved by the Newton-Raphson iteration scheme

$$\delta u_i^{M+1} = \delta u_i^M - \left[\frac{\partial \tilde{F}_i}{\partial(\delta u_j)} \right]^{-1} \tilde{F}_i(\delta \underline{u}^M)$$

In (4.30), δu_i couples only with itself and $\delta u_{i \pm 1}$. Thus the Jacobic matrix $\frac{\partial \tilde{F}_i}{\partial(\delta u_j)}$ is tridiagonal and can be inverted at each iteration very efficiently by the Thomas algorithm (see Ames (1965)). Convergence of this scheme (after two or three iterations) gives δu_i and hence u_i^{n+1}.

A second derivative discretisation of the form

$$\frac{g_{i+1} - 2g_i + g_{i-1}}{\Delta x^2}$$

with an arbitrary coefficient may be added in (4.28). By varying this coefficient, diffusion may be introduced which smoothes the solution near any sharp fronts. A suitable choice of coefficient, corresponding to upwinding, can reproduce the diffusion which would have been introduced had one-sided rather than central space differences been used.

For values of V less than $V_{MAX} \doteq 0.177$, the numerical solution of (4.26) with initial condition

$$\bar{h}(x,0) = 0$$

proceeded smoothly. The result for V = 0.17, t = 20.0 is shown in Fig. 4.5. The solution upstream of the front satisfied (4.25).

With $V > V_{MAX}$ the numerical solution began smoothly (see Fig. 4.6). As t increased, two humps appeared. The slope of the first hump increased until the solution became unphysical and the calculation stopped. No liquid extended upstream of the inlet and the film downstream of the inlet had the same form (and terminal thickness) as for just below V_{MAX}. A pulse appeared to be developing and trying to break at the edge of the inlet. Since there was no mechanism in the model to carry a broken wave downstream, the solution broke down. An estimate of the period of such a pulse is 0.5 seconds. This is of the same order of magnitude as the frequency of a disturbance wave.

A similar phenomenon may occur for two-phase flow at low gas flow-rates with sufficient shear stress developing over the pulse to send it downstream. Such a mechanism is not applicable to high gas flow-rates.

Azzopardi et al. (1979) proposed that disturbance waves are caused by the turbulent generation mechanism called turbulent bursts (see Heidrick et al. (1977)). They found that the wave frequencies at inception were similar to the equivalent turbulent burst frequencies. This mechanism can apply to upflow, downflow and horizontal stratified flow.

For high gas flow-rates, the inception behaviour has been found to be similar, experimentally, for upflow, downflow and horizontal stratified flow.

Since the effect of gravity upon the flow under such conditions is minimal, this is the expected result. Disturbance wave inception may be due to some interaction between the turbulent stresses in the gas and the liquid film, possibly turbulent bursts.

For low gas flow-rates, however, the author expects three different mechanisms to be involved. In horizontal flow, the interface is stabilised by gravity and inception may be governed by the neutral linear stability curve. In downwards flow, inception may be governed by Benjamin's falling film mechanism. Finally, in vertical upwards flow, wave inception may be due to inlet conditions as described in this section.

CHAPTER 5. Experimental Work

5.1 Introduction

In Chapter 6 the application of kinematic wave theory to the modelling of large amplitude waves in vertical annular two phase flow will be considered. In order to apply this theory, it is necessary to construct experimental curves of liquid flow rate against film thickness for fixed gas flow rate constant. Such systematic data, particularly in the ripple region, are not available from the experimental research literature.

The author undertook experiments to obtain this data using an experimental rig at AERE Harwell. In addition, in order to test the predictions of kinematic wave theory, she injected liquid pulses into the main film flow and observed their behaviour. The experiments are described in this Chapter.

5.2 Film Thickness Measurements

These experiments were carried out using apparatus similar to that described by Azzopardi et al. (1979). The apparatus is shown schematically in Fig. 5.1. The flow tube, of total length 5.5m, consisted of sections of perspex tubing of internal diameter 3.2 x 10^{-2}m. The fluids used were air and water. The flow was vertically upwards.

The air entered through a calming section of length 0.5m before being joined by the water, which entered through a porous section in the wall. It was assumed that no entrained droplets were created by the porous wall entry technique. It has been shown (Whalley et al. (1977)) that the presence of disturbance waves is a necessary condition for liquid droplet entrainment. Since the measurements were obtained in the ripple regime, it was assumed that there was no entrained liquid in the gas core. Thus the liquid film flow rate was given by the total water flow rate, which was controlled by a valve connected to a calibrated rotameter.

The film thickness was measured by means of a conductance probe (see

Hewitt et al.(1974). The probe consisted of two nickel pins set into the wall of the tube section, flush with the inner wall. The electrodes were positioned in a vertical line 1.25 x 10^{-2}m apart. The electrode section was 4m above the inlet. The conductivity of the water was increased to 55 mmho m^{-1} by adding potassium nitrate. A circuit box designed by Benn (1978) was used to produce a digital response voltage across the electrodes. The probes were calibrated by fitting several epoxy resin machined plugs into the electrode cell. When the cell was immersed in the tube solution, the plugs corresponded to liquid films of known thickness. A good linear relationship was obtained between the film thickness and the filtered output from the box.

The air pressure at the top of the tube was maintained at 1.34 bars. The air gas flow rate was fixed and the liquid flow rate was then adjusted. A low pass filter was used to obtain an average film thickness. Thirty voltage readings were taken at each flow rate and the mean recorded.

The measurements were taken in the ripple regime and were continued up to the point where disturbance waves appeared every few seconds. The wave inception liquid flow rate values were found to correspond with the results of Shearer (1964). The disturbance waves were clearly visible as milky bands which rushed up the tube at a considerably faster rate than the bulk of the liquid.

The ripples on the surface of the film were shown to be random by means of a correlator. The appearance of the ripples varied with the air flow rate. For low air flow rates, the ripples were large and distinguishable. At high air flow rates, the film was 'milkier', the ripples being smaller and more numerous. These features were reflected in the filter reading variations.

A number of experimental difficulties were experienced. Firstly, the conductance probe technique is thought to be unreliable when dealing with such extremely thin films ($<10^{-4}$m thick). The conductivity of the water also varied significantly with temperature.

Measurements with the liquid flow rate below 2.38-3.17 $kgm^{-2}s^{-1}$ in general were not possible, both due to the difficulty of closing the rotameter valve sufficiently and also due to non-wetting of the tube. For the lower liquid flow rates, the flow rate had first to be increased and then lowered to the required value in order to ensure wetting.

Due to the wavy nature of the film, even in the ripple regime, the voltmeter reading fluctuated. In order to record an average value, the strongest low pass filter available was used. Even so, fluctuations were evident and it was necessary to take many readings.

Although there were many sources of experimental error, all the measurements were taken on the same day with water at the same temperature ($15^{o}C$) and thus should be consistent.

The filter output was converted to an average film thickness value by means of the calibration curve. The results are given in Table 5.1. The graph in Fig. 5.2 shows the experimental results together with the average film thickness measurements obtained by Gill et al. (1963). The latter results were obtained in both the ripple and disturbance wave regimes using conductance probes. Some of their results are decidedly erratic. The two sets of results do appear to agree reasonably well, particularly for high gas flow rates.

5.3 Comparison Between Experimental Results and Values Calculated from the Shearer-Nedderman Correlation

Shearer and Nedderman (1965) conducted experiments on vertical upwards annular two-phase flow in tubes with diameters 3.18 x 10^{-2}m and 1.59 x 10^{-2}m. They measured the pressure drop in the tube as a function of air and liquid flow rates. They assumed that the interface appeared to the gas phase as a moving rough wall. They found that their results were well correlated in the ripple regime by the expressions

$$\frac{\Delta P}{L}\frac{D}{4} = C_f \, \rho_G \, (U_G - V_i)^2/2$$

$$\frac{1}{\sqrt{C_f}} = 4 \log_{10} \frac{D}{2\varepsilon} + 3.46 \qquad (5.1)$$

and

$$Y_L^+ = K_1 D^2 T + K_2 \left(\frac{U_G - V_i}{\mu_L}\right) \sqrt{\rho_G}\, \frac{\varepsilon}{D} \qquad (5.2)$$

where

ΔP = pressure drop

L = length of tube

D = diameter of tube

$$Y^+ = \sqrt{2Re_L} = \sqrt{2 G_L/\mu_L D} = \sqrt{G_L/\mu_L r_0} \qquad (5.3)$$

and K_1, K_2 are constants, their values being

$$K_1 = 6.104 \times 10^4 \; s^2 \, kg^{-1} \, m^{-2}$$

$$K_2 = 0.0122 \; kg^{\frac{1}{2}} \, m^{-\frac{1}{2}}$$

Using the values of the physical parameters relevant to the experiments described in the last section, (5.2) and (5.3) reduce to

$$G_L^{\frac{1}{2}} = 1.154 + 4.156 \, (U_G - V_i) \, \frac{\varepsilon}{D}$$

From (5.1) $\frac{2\varepsilon}{D} = 10^{\{0.865 - \frac{1}{4} C_f^{-\frac{1}{2}}\}}$

Therefore

$$G_L^{\frac{1}{2}} = 1.154 + 2.078 \, (U_G - V_i) 10^{\{0.865 - \frac{1}{4} C_f^{-\frac{1}{2}}\}} \qquad (5.4)$$

It will now be assumed, for lack of a better assumption (see Chapter 2), that the flow in the film is laminar.

Then $$G_L = \{\frac{\tau_i h_o}{2\mu_L} - g(\frac{1-\rho^*}{3\nu_L})h_o^2\} \frac{2\rho_L h_o}{R_o}$$

Thus $G_L = 5.8 \times 10^7 h_o^2\ C_f\ (U_G - V_i)^2 - 3.982 \times 10^{"}\ h_o^3$ (5.5)

Since $V_i << U_G$, V_i can be neglected in expressions (5.4) and (5.5). (5.4) and (5.5) are then two simultaneous equations for the three unknowns h_o, G_L, C_f.

Since the experiments described in section 5.3 were carried out in the ripple regime, the correlation derived by Shearer and Nedderman should be directly applicable. The $h_o v G_L$ graph derived from equations (5.4), (5.5) was therefore compared with that found by experiment.

On writing $h_o = 10^{-4}H$, $C_f = 0.005x_2^2$, $G_L = x_1^2$, (5.4), (5.5) become

$$x_1 = 1.154 + 2.078\ U_G 10^{(0.865-3.536/x_2)}$$

$$x_1^2 = 2.9 \times 10^{-3}\ HU_G^2\ x_2^2 - 0.398\ H^2$$

For certain values of U_g,H the curves do not intersect and there is no solution. The equations were solved numerically using Harwell subroutine NB02A.

The resulting $h_o v\ G_L$ curves are compared with the experimental results in fig. (5.3). There was no solution for h_o below a critical value depending on gas flow rate. There is good agreement for high but not low gas flow rates. The discrepancy at low gas flow rates could be due to a number of factors including inapplicability of the correlation in this region and the considerable experimental errors involved in measuring the average thickness of a rather wavy film.

5.4 Pulse Experiments

The basic apparatus used was the same as in the film thickness experiments. An additional conductance probe was positioned 0.88m vertically above the first one.

A pulse of liquid was sucked from or injected into, the main fluid flow by means of a syringe (see Fig. 5.4). A hydraulic system using compressed air drove the plunger back and forth. The syringe was securely mounted in a wooden block and the nozzle connected to a side arm in the pipe connecting the water supply to the tube. The travel length of the plunger was adjusted so that a volume of $1.5 \times 10^{-5} m^3$ was injected. By varying the air pressure, the time of the suck and injection could be varied. A brass plate was attached to the plunger mounting with a slit cut into it. This was adjusted so that, at the limits of the stroke, the slit rested above a torch bulb. Above the plate were pieces of fibre optic, their further ends clamped over a photodetector. The signal was amplified and then the pulses used to trigger a counter/timer.

The time taken for the pulse to travel from one probe to the other was measured using a double beam storage oscilloscope. The measurements were all taken in the ripple regime. It had been hoped to time either a transition from one known liquid flow rate to another or else a 'suck' pulse, effectively a transition from zero to a known value. Both of these measurements, however, proved to be impracticable, the features not being distinguishable on the oscilloscope trace.

A typical oscilloscope trace is shown in Fig. 5.5. It corresponds to a low gas flow rate (G_G = 39.7 kgm^{-2}s^{-1}). The injection pulse is clearly visible against the background of ripples. The experimental results are given in Table 5.2. Although the times given are averages over several readings, the times obtained were reasonably consistent.

It was found that the speed of the pulse did not depend critically on the injection time. The pulse appeared to be a single entity and produced a triangular oscilloscope trace. Naturally occurring disturbance waves travelled faster and had a more localised, sharply peaked trace.

The experiments were repeated after an interval of several weeks. Similar results were obtained to those in Table 5.2.

Using almost identical apparatus, Azzopardi et al (1979) observed the behaviour of injection pulses for flow rates just below the disturbance wave inception value. They found that disturbance waves were formed with properties similar to those of naturally occurring waves.

5.5 Single Frame Pulse Observations

A ciné film was taken of suck and injection pulses for a gas flow rate of 63.46 $kgm^{-2}s^{-1}$ and a liquid flow rate of 4.76 $kgm^{-2}s^{-1}$. The camera was focussed on the first metre of tube above the inlet. The speed of the film was 25 frames/sec. The film was analysed frame by frame. It was possible in this way to follow the progress of both the suck and injection pulses.

The suck pulse front was only just visible and measurements of travel distance were very subjective. No systematic trend in the behaviour of the speed of the front was observed. The average value for the front speed was $0.52ms^{-1}$.

In the region of the tube filmed, the injected pulses, in general, were found to be composed of more than one wave. The pulses could be followed from about 0.4m above the inlet. Below this height they were in shadow and could not be easily distinguished. The progress of a typical wave is shown in Fig. 5.6. The wave velocity is about $2ms^{-1}$ and decreases with distance up the tube. The catching up of one wave by a faster wave and the subsequent coalescence can also be distinguished.

CHAPTER 6. Kinematic Wave Theory

6.1 Outline of Theory

The concept of kinematic waves was first introduced in a paper by Lighthill and Whitham (1955). The author has attempted to apply kinematic wave theory to wave modelling in vertical two-phase flow. Before describing this particular application, an outline of the general theory will be given.

Consider a one-dimensional system in which there is a continuous distribution of either material or some state of the medium and for which there can be defined a density $\rho(x,t)$ per unit length and a flux $q(x,t)$ per unit time. A flow velocity $v(x,t)$ can be defined by

$$v = \frac{q}{\rho}$$

Assuming that the material (or state) is conserved, the rate of change of the total amount of it in any section $x_1 > x > x_2$ must be balanced by the net inflow across x_1 and x_2. That is

$$\frac{d}{dt}\int_{x_2}^{x_1} \rho(x,t)dx + q(x_1,t) - q(x_2,t) = 0 \qquad (6.1)$$

If $\rho(x,t)$ has continuous partial derivatives, taking the limit as $x_1 \to x_2$ gives the conservation equation

$$\frac{\partial \rho}{\partial t} + \frac{\partial q}{\partial x} = 0 \qquad (6.2)$$

Suppose that there exists, to some approximation, a functional relationship between q and ρ

$$q = Q(\rho) \qquad (6.3)$$

Substituting in (6.2) gives

$$\frac{\partial \rho}{\partial t} + c(\rho)\frac{\partial \rho}{\partial x} = 0 \tag{6.4}$$

where $$c(\rho) = Q'(\rho) \tag{6.5}$$

Equation (6.4) has one system of characteristics

$$\frac{dx}{dt} = c(\rho)$$

Along each of these characteristics ρ, and hence $c(p)$ is constant.

Consider the initial value problem

$$\rho = f(x) \qquad t = 0 \qquad -\infty<x<\infty$$

The solution of (6.4) is then given in parametric form by

$$\rho = f(\xi) \qquad t = \frac{x-\xi}{c(f(\xi))} = \frac{x-\xi}{F(\xi)} \qquad F(\xi) = c(f(\xi)) \tag{6.6}$$

Thus the distribution of ρ is known in the whole (x,t) plane. If only one characteristic curve C passes through each point of the (x,t) plane, this procedure leads to a unique solution. However, it can happen that characteristics cross and certain points carry more than one value of ρ. Then there exists no solution to the imposed initial value problem that is continuous at each point of the (x,t) plane. In order to obtain an unique solution, it is necessary to eliminate regions of multi-valuedness by the insertion of jump discontinuities.

Fig. 6.1 shows the progress of an initial hump for which $c'(\rho)>0$. The corresponding characteristic diagram is shown in Fig. 6.2 . The wave ultimately 'breaks' to give a triple valued solution. Breaking begins at time $t = t_B$ when the profile for ρ first develops an infinite slope.

i.e. when $$t = \frac{-1}{F'(\xi_B)}$$

where $|F'(\xi)|$ is a maximum for $\xi = \xi_B$.

Suppose that there is a discontinuity at $x = s(t)$ and that x_1 and x_2 are chosen so that $x_1 > s(t) > x_2$. Suppose that ρ and q and their first derivatives are continuous in $x_1 \geqslant x > s(t)$ and $s(t) > x \geqslant x_2$ and have finite limits as $x \to s(t)$ from above and below. Then (6.1) may be written

$$q(x_2,t) - q(x_1,t) = \frac{d}{dt}\int_{x_2}^{s(t)} \rho(x,t)dx + \frac{d}{dt}\int_{s(t)}^{x_1} \rho(x,t)dx$$

$$= \rho(s^-,t)\dot{s} - \rho(s^+,t)\dot{s} + \int_{x_2}^{s(t)} \rho_t(x,t)dx$$

$$+ \int_{s(t)}^{x_1} \rho_t(x,t)dx$$

where $\rho(s^-,t)$, $\rho(s^+,t)$ are the values of $\rho(x,t)$ as $x \to s(t)$ from below and above respectively and $\dot{s} = \frac{ds}{dt}$. Since ρ_t is bounded in each of the integrals separately, the integrals tend to zero in the limit as $x_1 \to s^+$, $x_2 \to s^-$. Therefore $q(s^-,t) - q(s^+,t) = \{\rho(s^-,t) - \rho(s^+,t)\}\,\dot{s}$.

Adopting the conventional notation of a subscript 1 for the values ahead of the shock and a subscript 2 for values behind, if U is the shock velocity, then

$$q_2 - q_1 = U(\rho_2 - \rho_1) \qquad (6.7)$$

The solution will be continuous on either side of a shock. Therefore the assumption (6.2) holds and $q_1 = Q(\rho_1)$, $q_2 = Q(\rho_2)$. The shock condition (6.7) becomes

$$U = \frac{Q(\rho_2) - Q(\rho_1)}{\rho_2 - \rho_1} \qquad (6.8)$$

The right hand side of this equation is the slope of the chord joining the two points on the flow-concentration curve (for given x) which correspond to the states ahead of and behind the shock front when it reaches x. In the limit when the shock front becomes a continuous wave, the slope of the chord becomes the slope of the tangent and the velocity given by (6.8) coincides with that given by (6.5).

The initial value problem reduces to fitting shock discontinuities into the solution (6.6) so that (6.8) is satisfied and multi-valued solutions are avoided.

For a more detailed discussion of the theory of kinematic waves, see Whitham (1974).

Kinematic wave theory is particularly useful for physical systems which are too complicated to be analysed completely but for which an experimental $q v \rho$ graph can be constructed. Since kinematic waves are governed by a single differential equation of the form (6.2), they are also termed continuity waves (see Cole (1968), Wallis (1969)).

Examples of applications of the theory are wave motions in traffic flow (Lighthill and Whitham (1955)), simple waves in ideal gases (e.g. Whitham (1974) p.167), flood waves in long rivers (Lighthill and Whitham (1955), Kluwick (1977)), sedimentation (Wallis (1960)) and glaciers (Nye (1960)).

6.2 Extensions

In kinematic wave theory, a kinematic shock is really a relatively narrow region in which, due to the locally rapid variation in q, the q-ρ relation (6.3) becomes invalid. As a first approximation it may be treated as a discontinuity producing the abrupt changes in q and ρ. A more detailed flow description in the shock region is usually obtained by calculating steady solutions in a higher order system of model equations.

As an example, consider turbulent flow down an inclined plane (see

Whitham (1974) and section 2.8). On averaging the velocity down the slope over the depth of the fluid and neglecting the fluid acceleration in the y direction, the continuity and momentum equations become

$$h_t + (hu_a)_x = 0 \tag{6.9}$$

$$u_{at} + u_a u_{ax} + g'h_x = g's - C_f \frac{u_a^2}{h} \tag{6.10}$$

where $g' = g\cos\alpha$, $s = \tan\alpha$ and C_f is the friction coefficient.

The kinematic wave approximation to (6.9), (6.10) neglects the left-hand side of (6.10) and takes

$$h_t + (hu_a)_x = 0 \qquad u_a = \left(\frac{g's}{C_f}\right)^{\frac{1}{2}} h^{\frac{1}{2}}$$

Kinematic shocks must satisfy the shock condition

$$U = \frac{u_{a2}h_2 - u_{a1}h_1}{h_2 - h_1}$$

In order to determine the shock structure, it is necessary to find steady solutions in the more detailed description (6.9), (6.10). Looking for solutions of the form

$$h = h(z) \qquad u_a = u_a(z) \qquad z = x - Ut$$

(6.9), (6.10) become

$$(u_a - U)\frac{du_a}{dz} + g'\frac{dh}{dz} = g's - \frac{C_f\, u_a^2}{h} \tag{6.11}$$

$$h(U - u_a) = q_0 \tag{6.12}$$

where the continuity equation has been integrated once. These are precisely the equations derived by the integral method in section 2.8. Uniform states (h_i, u_{ai}) at $z = \pm\infty$ satisfy

$$g's - C_f \frac{u_{a1}^2}{h_1} = g's - C_f \frac{u_{a2}^2}{h_2} = 0$$

$$h_1(U-u_{a1}) = h_2(U-u_{a2}) = q_o$$

All the flow quantities can be expressed in terms of h_1 and h_2. The speed U is given by

$$U = \frac{u_{a2}h_2 - u_{a1}h_1}{h_2 - h_1} = (\frac{g's}{C_f})^{\frac{1}{2}} \frac{h_2^{\frac{3}{2}} - h_1^{\frac{3}{2}}}{h_2 - h_1}$$

This is the same as the shock condition governing discontinuities in the basic kinematic theory. This is the usual result, with the more detailed structure being given by the solution of (6.11), (6.12) for a monoclinic wave.

Whitham (1974) showed that a continuous solution exists for values of U satisfying

$$c_1 < U < c_2 \tag{6.13}$$

where c_i are the maximum characteristic velocities on either side of the shoch according to the linearised form of equations (6.9), (6.10). In this example $c_i = u_{ai} + \sqrt{g'h_i}$. If this condition is violated, there will still be a discontinuity in the profile according to the higher order theory. This higher order discontinuity s(t) satisfies jump conditions derived from the conservation form of equations (6.9), (6.10). For the case of turbulent flow down a plane these conditions are the usual hydraulic jump conditions:

$$- \dot{s}\, h\Big|_{0-}^{0+} + hu_a\Big|_{0-}^{0+} = 0$$

$$- \dot{s}\, hu_a\Big|_{0-}^{0+} + (hu_a^2 + \tfrac{1}{2}g'h^2)\Big|_{0-}^{0+} = 0$$

6.3 Application of Kinematic Wave Theory to Vertical Annular Two Phase Flow

The formulation and solution of a detailed mathematical model for large disturbance waves is a formidable task. However, the waves are approximately uniform around the tube, $\frac{h}{R_o} \ll 1$, and the wave slope, especially on the windward side of the wave, is very shallow. Thus, to a first approximation, the system can be regarded as one dimensional with flow variables q(x,t), h(x,t) where h is the film thickness and q is the liquid flux per unit length of circumference. Also, at least in the back of the wave, the relation between q and h can be assumed to approximate that for a flat film. If an experimental qvh curve can be constructed for a flat film, kinematic wave theory can be used to describe the time dependent behaviour of large amplitude disturbances. In any region of steep slope, the assumption (6.3) will break down and the solution will involve kinematic shocks.

An experiment to construct a hvG_L and hence a qvh ($q = \frac{G_L R_o}{2\rho_L}$)curve was described in Chapter 5. The film thickness measurements could only be taken in the ripple region. For liquid mass fluxes in the disturbance wave region, large waves arose spontaneously and it was impossible to record the thickness of a flat film. The film thickness measurements obtained in this region by Gill and Hewitt (1963), shown in Fig. 5.2, were averages over film and disturbance waves. The graph of average film thickness against liquid flux shows a marked change at the point of wave inception. This corresponds to the sudden increase in pressure drop measured by Shearer and Nedderman (1965) and can possibly be explained in terms of flow separation over breaking disturbance waves (see Wu (1968)).

Thus, although a qvh graph can be constructed satisfactorily in the ripple region, it is not clear what relation should be assumed beyond the point of wave inception. A possibility is to assume that the measured increase in pressure drop is due solely to the effect of airflow separation over breaking disturbance waves and that if it was possible for flat films with ripples to exist in the disturbance wave region, the relationship between q and h would be an extrapolation of the curve in the ripple region.

Due to experimental difficulties in measuring very thin films, the experimental results show a fair degree of scatter. The curves calculated from the Shearer-Nedderman correlation agree reasonably with the experimental data (see section 5.3) and have the advantage that they can be extrapolated easily beyond the inception point.

Assuming a relationship between liquid flux and film thickness

$$q = \bar{u}h = Q(h) \tag{6.14}$$

the equation for long waves corresponding to (6.4) is

$$h_t + c(h)h_x = 0 \qquad \text{where } c(h) = Q'(h) \tag{6.15}$$

6.4 Application to the Pulse Experiments

In the second set of experiments described in 5.4., a syringe was attached to a side arm at the bottom of the flow tube. A quantity of water was drawn out of the flow and at a later time injected back into it. In this way, two pulses were created - a 'suck' pulse and an 'injected' pulse.

The boundary value problem corresponding to the injected pulse experiment is:

$$\begin{array}{lll} h = h_o & x>0 & t = 0 \\ h = g(t) & t>0 & x = 0 \end{array}$$

The characteristics in the (x,t) plane for this problem are shown in Fig. 6.3. An analysis of such a boundary value problem is given by Whitham (1974).

Consider a characteristic which passes through the t axis at $t = \tau$. For this characteristic

$$h = g(\tau)$$

$$x = G(\tau)(t-\tau) \qquad G(\tau) = c\{g(\tau)\}$$

Suppose that the characteristics $\tau_1(t)$, $\tau_2(t)$ meet at the shock $s(t)$ at time t

Then $$s(t) = (t-\tau_1)c_1 \qquad c_1 = G(\tau_1) \tag{6.16}$$

$$s(t) = (t-\tau_2)c_2 \qquad c_2 = G(\tau_2) \tag{6.17}$$

Let $\tau(h)$ be the inverse of $h = g(\tau)$ and $X(h,t)$ be the inverse of $h = h(x,t)$.

Then $$X(h,t) = c(h)(t - \tau(h))$$

Since h is conserved, the discontinuity must cut off lobes of equal area.

$$\therefore\ (h_1-h_2)s(t) = \int_{h_2}^{h_1} X(h,t)dh = \int_{h_2}^{h_1} \{c(h)(t - \tau(h))\}dh$$

Putting $c(h) = Q'(h)$ and integrating by parts:

$$(q_1-q_2)t - (h_1-h_2)s(t) = q_2\tau_2 - q_1\tau_1 - \int_{\tau_1}^{\tau_2} q(h)d\tau$$

Using (6.16), (6.17) to eliminate t, $s(t)$:

$$\{(q_2-h_2c_2)c_1 - (q_1-h_1c_1)c_2\}\ \frac{\tau_2-\tau_1}{c_2-c_1} = -\int_{\tau_1}^{\tau_2} q(\tau)d\tau$$

Since the shock starts from the origin

$$h_1 = h_o \qquad c_1 = c_o \qquad q_1 = q_o$$

Using τ can now be eliminated to give

$$\{(q-q_o) - (h-h_o)c\}\ (t-\tau) = -\int_0^{\tau} \{q(t')-q_o\}\ d\tau' \tag{6.18}$$

As a first approximation, take the injected pulse to have a uniform distribution

$$q = \begin{cases} q_o & t<0 \quad t>T \\ q^* & 0<t<T \end{cases}$$

Then (6.18) becomes

$$\{(q-q_o) - (h-h_o)c\}\ (t-\tau) = \begin{cases} -(q^*-q_o)\tau & \tau<T \\ -(q^*-q_o)T & \tau>T \end{cases}$$

For $\tau<T$ the shock will move with a constant speed, its position being given by

$$s(t) = \left(\frac{q^*-q_o}{h^*-h_o}\right)t \tag{6.19}$$

The last q^* characteristic meets the shock at $\tau = T$ where

$$T = t - \frac{s(t)}{c^*} \tag{6.20}$$

Eliminating t from (6.19), (6.20)

$$s(t) = \frac{Tc^*(q^*-q_o)}{c^*(h^*-h_o)-(q^*-q_o)} = s_o \tag{6.21}$$

Suppose $s>s_o$. Then the position of the shock is given by

$$\left.\begin{aligned} \{(q-q_o)-(h-h_o)c\}\ \frac{s(t)}{c(h)} &= (q^*-q_o)T \\ s(t) &= c(h)(t-T) \end{aligned}\right\} \tag{6.22}$$

Suppose $s>>s_o$. Then $(h-h_o)<<h_o$, $t>>T$ and

$$\begin{aligned} q-q_o &= Q'(h_o)(h-h_o) + \tfrac{1}{2}\ Q''(h_o)(h-h_o)^2 + \ldots \\ &\sim c(h_o)(h-h_o) + \tfrac{1}{2}\ c'(h_o)(h-h_o)^2 \end{aligned}$$

Using this relation in the equations (6.22) gives at the shock

$$h-h_0 \sim \frac{1}{c'(h_0)} \sqrt{\frac{(q^*-q_0)T2c'(h_0)}{t}} \tag{6.23}$$

$$c-c_0 \sim \sqrt{\frac{2(q^*-q_0)Tc'(h_0)}{t}} \doteq c_0 + c'(h_0)(h-h_0) \tag{6.24}$$

$$s(t) \sim c_0 t + \sqrt{2(q^*-q_0)Tc'(h_0)t} \tag{6.25}$$

Thus, as $t \to \infty$, the shape of the pulse becomes triangular as shown in Fig. 6.4.

For a non-constant pulse (6.23)-(6.25) still hold with $(q^*-q_0)T$ replaced by

$$A = \int_0^T (q^* - q_0)d\tau = \frac{1}{2\pi R_0} \text{ (volume injected)}$$

This is the result derived by Whitham (1974).

Although the expression (6.21) depends on a relation $q = Q(h)$ being known for very large values of q, the final asymptotic solution depends only on quantities relating to the base film and the volume of liquid injected.

The (x,t) plane corresponding to the suck pulse is shown in Fig. (6.5). The asymptotic form of the pulse is again a triangular wave. The speed of the shock is equal to the slope of the chord joining the points on the Qvh graph corresponding to conditions directly in front of and behind the shock front. As $t \to \infty$, and the shock strength decreases to zero, this chord becomes the tangent at (q_0,h_0) and the speed of the shock increases to c_0. Thus the speed of the suck pulse is predicted to lie between the average film speed q_0/h_0 and c_0.

Measurements were made of the time interval between an injection pulse meeting two conductance probes (see section 5.4). Assume that by the time the pulse reaches the first probe at X_1, it is in the asymptotic region.

That is $$X_1 \geqslant \frac{Tc^*(q^*-q_0)}{c^*(h^*-h_0) - (q^*-q_0)}$$

Then the shock is described by equations (6.23)-(6.25). Suppose the shock front reaches the probes at $t = T_1, T_2$.

Then $$X_1 = c_0T_1 + \sqrt{2Ac'(h_0)} \ \ T_1^{\frac{1}{2}}$$

$$X_2 = c_0T_2 + \sqrt{2Ac'(h_0)} \ \ T_2^{\frac{1}{2}}$$

Thus, given the relationship (6.14) between q and h, A and X_i, it should be possible to calculate T_1, T_2 and hence T_2-T_1. The measured average speed between the probes should be greater than c_0. Table 6.1 shows the measured average pulse speed u_p together with the average film velocity and c_0 calculated from the Shearer-Nedderman correlation. The results are discouraging. In all cases u_p is about half the value of c_0.

The comparison between kinematic wave theory and the single frame pulse observations nearer the inlet is more encouraging. For $G_G = 63.4$ kgm^{-2}s^{-1}, $G_L = 4.76$ kgm^{-2}s^{-1} and an injected volume of fluid of 15×10^{-6}m^3, $s_0 = 6.29$m. Thus the asymptotic results should not be valid. However, experimentally the pulse speed does decrease with distance up the tube.

The suck pulse had an average speed of about 0.5 ms^{-1}. This lies between the average film speed and c_0, as predicted by kinematic wave theory.

6.5 Application to Disturbance Wave Modelling

According to kinematic wave theory, any initial wave profile will become triangular for large time (see section 6.4). Assume that the front of a disturbance wave can be approximated by a discontinuity. Then from (6.8), the wave speed is given by

$$c = \frac{\bar{u}_p h_p - \bar{u}_o h_o}{h_p - h_o} \qquad (6.26)$$

where p refers to values at the wave crest and o refers to base film properties and the relationship $h\bar{u} = Q(h)$ is known. (6.26) can be rearranged to give

$$(\bar{u}_p - c)h_p = (\bar{u}_o - c)h_o$$

Thus lowest order kinematic wave theory is of the same form as the models described in section 2.10. Table 6.2 shows a comparison between the wave speeds calculated using (6.26) and the Shearer-Nedderman correlation and the values calculated by James (1979). The base film flow rate was taken to be the critical flow rate for disturbance wave inception. For $G_G = 31.7$ kgm^{-2}s^{-1}, Nash's results are in closer agreement than James' although still higher than the experimental wave speeds. For $G_G = 79.3$ kgm^{-2}s^{-1}, the predicted wave speed is far too high. Comparisons with the other experimental results in Table 2.2 were not possible due to the non-convergence of equations (5.4), (5.5) for the Shearer-Nedderman correlation. Thus, the Shearer-Nedderman correlation is clearly not appropriate to account for ripple roughness at large film thicknesses.

Certain qualitative comparisons can be made between kinematic wave theory and experiment. The theory predicts that an arbitrary wavy surface will in time separate into a number of large amplitude waves (see Kluwick (1977)) which appear to be travelling on the surface of a thin film. However it does not explain why there should be a critical flow rate for wave inception nor why the waves appear almost instantaneously as the liquid enters the tube. It allows for coalescence as a confluence of shocks but does not predict the resulting wave to have an amplitude or speed greater than its component waves.

According to kinematic wave theory the profile of any disturbance should become triangular with a steep front for large time (equations (6.23)-

(6.25)). Experimentally, waves in horizontal flow do have this form. In vertical flow, however, the waves appear to be almost symmetrical.

The lowest order theory cannot predict any increase in wave height. It neglects the destabilising effects of the pressure and shear stress perturbations (see section 4.4) and inertia effects. Also it can only approximate the front of a wave by a shock discontinuity. A more detailed flow description in the shock region is obtained by calculating steady solutions in a higher order system of model equations (see section 6.3). For disturbance waves in two-phase flow, the next-order equations are precisely the integral approach equations (2.25), (2.26) with $\beta = -\frac{\pi}{2}$. In (2.26) τ_w, τ_s, Γ and $\frac{dp_s}{dx}$ have all to be specified.

CHAPTER 7. SMAC Calculations

7.1 Introduction

The integral method, described in section 2.8, seems to the author to be the most encouraging of the approaches described in Chapter 2 for modelling large disturbance waves in vertical annular two-phase flow. It also provides the set of higher order model equations necessary for an extension of lowest order kinematic wave theory. In the integral method, the process of averaging over the film thickness leads to certain details of the flow being lost. In particular, the parameters $\Gamma(x), \tau_w(x)$ occurring in the model cannot be determined directly. Miya assumes in his model (see section 2.9) that the wave has a constant speed and a steady profile. It is not clear to the author that such solutions exist.

A numerical model, SMAC, was used in order to follow the time dependent behaviour of a disturbance wave and to provide information regarding $\Gamma(x)$, $\tau_w(x)$. SMAC is a computational technique for calculating time dependent flows of incompressible viscous fluids. It can deal with a free surface and is not restricted to small amplitude disturbances.

It was also possible to compare the time dependent behaviour of a disturbance with the predictions of lowest order kinematic wave theory. In this way the effects of the pressure and inertia terms neglected in the theory could be gauged.

7.2 The Marker and Cell Technique

SMAC (Simplified Marker And Cell) is based on the MAC method developed mainly in Los Alamos. MAC uses velocity and pressure as the primary physical variables. Massless marker particles are situated in each cell containing fluid. Finite difference forms of the continuity and momentum equations are solved iteratively to advance the flow field explicitly in time. The marker particles move with the advection field. The particles do not participate in the computation except by defining the free surface on which boundary conditions are imposed. Browne (1978) summarises the development of the MAC technique and gives a comprehensive list of references.

In MAC, the pressure for each cell is obtained by solving a Poisson equation. The source term of this equation is a function of the velocities, derived in such a manner that the resulting momentum equations satisfy the incompressibility condition. The full Navier-Stokes equations are then used to find the new velocity field throughout the mesh. The method is excessively complicated in several respects. The boundary conditions need to be derived so that there is precise consistency among the momentum and pressure equations. Although this presents little difficulty for simple configurations, it does lead to tedious derivation and programming logic for the case of rigid obstacles and various input or output boundaries.

The SMAC method was developed in Los Alamos (Amsden & Harlow (1970)) in order to overcome these difficulties. In SMAC, each calculational cycle is separated into two phases in a way resembling the technique proposed by Chorin (1968) for confined flows.

Phase I. A tentative field of advanced time velocities is calculated using an arbitrary pressure field within the fluid but with a pressure boundary condition at the free surface satisfying the normal stress condition. The correct velocity boundary conditions are also imposed. Since the vorticity transport equation is independent of pressure, this velocity field carries the correct vorticity at every interior point in the fluid. It does not however satisfy the incompressibility condition

$$\nabla . \bar{u} = 0 \tag{7.1}$$

Phase II. The tentative velocities are altered by the addition of the gradient of an appropriate potential function so as to satisfy (7.1). The resulting field carries the same vorticity and satisfies the incompressibility condition. It is uniquely determined and hence is the correct solution.

Since the pressure field need never be calculated using SMAC, only the velocity boundary conditions and free surface stress conditions are necessary. The Poisson equation needs only homogeneous boundary conditions. Although not a feature of the version of SMAC used ,it would thus be possible to use more efficient direct solution techniques.

In SMAC there is a further phase in the calculation.

Phase III. The massless marker particles are moved according to an area-velocity weighting scheme.

A detailed account of the SMAC method together with a flow diagram and a FORTRAN listing are given by Amsden and Harlow (1970). Example calculations are also included. Also see Nash (1980).

A number of research workers have suggested other refinements to the MAC technique. Chan et al. (1970) and Nichols and Hirt (1971) have considered improvements to the treatment of the boundary conditions. Surface tension effects have been considered by Daly (1969) and Foote (1973). The inclusion of variable density and an energy equation is found in Rivard et al. (1973). Hirt and Cook (1972) have applied the technique to 3D flows while Viecelli (1969) and Smithers (1978) have considered boundaries of arbitrary shape.

Recent developments have been concerned with the inclusion of more implicit terms in the finite difference forms of the equations and with the use of a combination of Lagrangian and Eulerian techniques to handle a wider range of flow speeds. These latter methods replace the stationary grid by a grid moving in such a way that each cell contains the same element of fluid throughout the calculation. They are not appropriate for flows undergoing large distortions where the cells are twisted into unacceptable shapes.

Examples are YAQUI (Hirt 1974) and GALE (Chan 1975).

Browne (1978) summarises the development of the MAC technique and gives a comprehensive list of references.

7.3 The ZUNI Program

The numerical scheme used by the author is based on the Los Alamos SMAC program ZUNI. The program, written for use on a CDC 6600 computer had first to be translated from CDC to H Fortran and modified for use on the Harwell IBM 370 computer.

The basic program is designed to model single phase fluid flow with zero imposed free surface stresses. The initial fluid distribution can be specified in terms of a superposition of rectangular and circular fluid parts, the velocity in each part being constant. Fluid inflow at a constant speed can be prescribed through one boundary together with continuative or prescribed out-flow through the opposite boundary. Further details can be found in the Los Alamos report Amsden and Harlow (1970b). The test examples given in this report were run successfully.

The program can be used for calculations in either cylindrical or plane co-ordinates. For the application to vertical two phase flow the plane co-ordinate formulation is appropriate. The equations in this Chapter will refer to this case.

The computing mesh is shown in Fig. 7.1. There are five types of computational cell:

1. Empty (EMP) cell containing no fluid.
2. Full (FUL) cell containing fluid and having no EMP cells adjoining any of its four faces.
3. Free-surface (SUR) cell containing fluid but with at least one adjoining EMP cell.
4. Boundary (BND) cell lying in the belt of cells outside the boundaries.

These cells simplify the task of handling boundary conditions particularly those relating to velocities.

5. Obstacle (OB) cells lying within an imposed rectangular obstacle in the flow field.

The primary cell variables are the two velocity components u,v, the pseudo-pressure θ, the velocity divergence D and the potential function ψ. The centring of the variables about a cell is shown in Fig. 7.2. $u_{i+\frac{1}{2},j}$, $v_{i,j+\frac{1}{2}}$ are denoted by U(I,J), V(I,J) respectively.

The Navier Stokes and continuity equations are expressed in the form

$$(7.2)\quad \left\{ \begin{aligned} &\frac{\partial u}{\partial t} + \frac{\partial (u^2)}{\partial x} + \frac{\partial (uv)}{\partial y} = -\frac{\partial \phi}{\partial x} + g_x + \nu \frac{\partial}{\partial y} \left(\frac{\partial u}{\partial y} - \frac{\partial v}{\partial x}\right) \\ &\frac{\partial v}{\partial t} + \frac{\partial (uv)}{\partial x} + \frac{\partial (v^2)}{\partial y} = -\frac{\partial \phi}{\partial y} + g_y - \nu \frac{\partial}{\partial x} \left(\frac{\partial u}{\partial y} - \frac{\partial v}{\partial x}\right) \\ &D \equiv \frac{\partial u}{\partial x} + \frac{\partial v}{\partial y} = 0 \end{aligned} \right.$$

In the above equations ϕ is the pressure with the fluid density normalised to unity. The finite difference representation of the equations uses explicit time differencing.

A number of modifications to the program have had to be made by the author in order to extend SMAC to model two phase flow. The two phases are regarded as a one phase liquid film flow with imposed free surface boundary conditions. These conditions depend on the current surface profile and model the effect of the gas stream.

New subroutines have been introduced so as to incorporate an inflow velocity profile varying with depth, initial velocities varying with position and an initial rectangular fluid part with an arbitrary upper surface.

A major alteration to the program has been the introduction of a second ordered set of marker particles to move with the fluid surface. These particles are moved in a similar fashion to the interior particles; that is by a linear area-weighted velocity interpolation. A reasonably accurate representation of the fluid surface $y = h(x)$ is thus given at every cycle. The initial distance between the x co-ordinates of the surface particles is taken to be $\frac{\delta x}{4}$. During the calculation a surface particle is deleted if the distance between it and the next one becomes less than $\frac{D}{8}$ and inserted if the distance between two particles becomes greater than $\frac{3D}{8}$ where $D^2 = \delta x^2 + \delta y^2$. These distances are recommended by Smithers (1978).

Another subroutine calculates the first and second derivatives $h'(x)$, $h''(x)$ of the surface by five point central differences at the positions of the marker particles.

The free surface boundary conditions have been modified to cater for time dependent imposed surface stresses. A new primary cell variable TAUS(I,J) = τ_s/ν has been introduced. At the beginning of each cycle a subroutine calculates the imposed surface normal and tangential stresses at the centre of every SUR cell, corresponding to the current surface profile.

Other minor alterations have been made to the program. They will be mentioned in context in the following sections.

The report by Nash (1980) gives a more detailed account of the ZUNI calculational cycle and the modifications made by her to cater for two phase flow.

7.4 Form of the Momentum Convection Terms

The momentum convection terms from the equations of fluid motion (7.2) are

$$\frac{\partial}{\partial x}(u^2) + \frac{\partial (uv)}{\partial y}$$

$$\frac{\partial}{\partial x}(uv) + \frac{\partial}{\partial y}(v^2)$$

In the original form of MAC, a central difference form of these terms was used:

$$\frac{u^2_{i+1,j} - u^2_{i,j}}{\delta x} + \frac{(uv)_{i+\frac{1}{2},j+\frac{1}{2}} - (uv)_{i+\frac{1}{2},j-\frac{1}{2}}}{\delta y}$$

$$\frac{(uv)_{i+\frac{1}{2},j+\frac{1}{2}} - (uv)_{i-\frac{1}{2},j+\frac{1}{2}}}{\delta x} + \frac{v^2_{i,j+1} - v^2_{i,j}}{\delta y}$$

where for example

$$u^2_{ij} = \tfrac{1}{4}(u_{i+\frac{1}{2},j} + u_{i-\frac{1}{2},j})^2$$

$$(uv)_{i+\frac{1}{2},j+\frac{1}{2}} = \tfrac{1}{4}(u_{i+\frac{1}{2},j} + u_{i+\frac{1}{2},j+1})(v_{i,j+\frac{1}{2}} + v_{i+1,j+\frac{1}{2}})$$

This finite difference scheme leads to a destabilising truncation error term (see Hirt (1968)). To eliminate this, Hirt introduced the 'ZIP' form for the cell centred momentum convection terms. This type of differencing introduces the definition

$$(u_{ij})^2 \equiv u_{i-\frac{1}{2},j}\, u_{i+\frac{1}{2},j}$$

This scheme, used in the Los Alamos SMAC program assures internal momentum conservation as in MAC and also conserves momentum in the immediate vicinity of a rigid wall.

In the current version of SMAC, the cell-corner convection terms have been replaced by a donor cell formulation, for example

$$(uv)_{i+\frac{1}{2},j-\frac{1}{2}} \equiv \begin{cases} u_{i+\frac{1}{2},j}\, v_{i+\frac{1}{2},j-\frac{1}{2}} & \text{if } v_{i+\frac{1}{2},j-\frac{1}{2}} < 0 \\ u_{i+\frac{1}{2},j-1}\, v_{i+\frac{1}{2},j-\frac{1}{2}} & \text{if } v_{i+\frac{1}{2},j-\frac{1}{2}} \geqslant 0 \end{cases}$$

This modification was recommended by Amsden and Harlow (1970b) in a post-script. Although this scheme does improve stability, an artificial viscosity is introduced which could affect the accuracy of certain problems.

7.5 Boundary Conditions

Consider a FUL cell adjacent to a left wall (Fig. 7.3). For a viscous fluid, the appropriate boundary condition is that of no-slip where the tangential velocity is forced to go to zero at the wall.

$$u|_o = 0 \quad \Rightarrow \quad u_{i-\frac{1}{2},j} = 0$$

$$v|_o = 0 \quad \Rightarrow \quad v_{i-1,j+\frac{1}{2}} = -v_{i,j+\frac{1}{2}}$$

$$v_{i-1,j-\frac{1}{2}} = -v_{i,j-\frac{1}{2}}$$

$$\frac{\partial\psi}{\partial n}\Big|_o = 0 \quad \Rightarrow \quad \psi_{i-1,j} = \psi_{i,j}$$

At an inflow wall, fluid moves into the system at a prescribed rate. Marker particles are inserted through the wall to represent the incoming fluid.

$$u|_o = u_L \quad \Rightarrow \quad u_{i-\frac{1}{2},j} = u_L \text{ prescribed}$$

$$v|_o = 0 \quad \Rightarrow \quad v_{i-1,j+\frac{1}{2}} = -v_{i,j+\frac{1}{2}}$$

$$v_{i-1,j-\frac{1}{2}} = -v_{i,j-\frac{1}{2}}$$

$$\frac{\partial\psi}{\partial n}\Big|_o = 0 \quad \Rightarrow \quad \psi_{i-1,j} = \psi_{i,j}$$

A continuative outflow boundary allows fluid to pass out of the system at its own chosen rate:

$$\tilde{u}_{i-\frac{1}{2},j} = \tilde{u}_{i+\frac{1}{2},j}$$

$$u_{i-\frac{1}{2},j} = \tilde{u}_{i-\frac{1}{2},j} - \frac{1}{\delta x}(\psi_{i,j} - \psi_{i-1,j})$$

where $$\psi_{i-1,j} = 0$$

$$\frac{\partial v}{\partial n}\bigg|_o = 0 \quad \Rightarrow \quad v_{i-1,j+\frac{1}{2}} = v_{i,j+\frac{1}{2}}$$

$$v_{i-1,j-\frac{1}{2}} = v_{i,j-\frac{1}{2}}$$

where $\tilde{u}$ is the 'tentative' velocity field.

In her two phase flow modelling work the author found that more accurate results were obtained by imposing the condition $\psi_{i-1,j} = \psi_{i,j}$ at the continuative outflows corresponding to $\frac{\partial \psi}{\partial x} = 0$ than the condition above.

The boundary conditions to be satisfied at the free surface are the normal and tangential stress conditions. For example, consider the surface cell $S_{i,j}$ in Fig. 7.4a. The tangential stress condition is

$$\frac{\partial u}{\partial y} + \frac{\partial v}{\partial x} = \frac{\tau}{\mu}$$

where τ is the imposed tangential surface shear stress. $u_{i+\frac{1}{2},j+1}$ is determined by

$$u_{i+\frac{1}{2},j+1} = u_{i+\frac{1}{2},j} - \frac{\delta y}{\delta x}\left(v_{i+1,j+\frac{1}{2}} - v_{i,j+\frac{1}{2}}\right) + \frac{\tau_{i,j}}{\mu}\,\delta y$$

The normal stress condition is

$$\phi = \phi_{(\text{applied})} + \frac{2\nu\partial v}{\partial y}$$

with finite difference form

$$\phi_{i,j} + \phi_{i,j\,(\text{applied})} + \frac{2\nu}{\delta y}\left(v_{i,j+\frac{1}{2}} - v_{i,j-\frac{1}{2}}\right)$$

Consider the corner surface cell $S^*_{i,j}$ (Fig. 7.4b) with two adjacent EMP cells. The surface slope is assumed to be at 45^0 to the horizontal within the cell. The tangential stress condition with zero imposed surface shear stress becomes

$$\frac{\partial v}{\partial y} - \frac{\partial u}{\partial x} = 0$$

The normal stress condition becomes

$$\phi_{ij} = \phi_{ij(\text{applied})} - 2\nu \left(\frac{\partial v}{\partial x} + \frac{\partial u}{\partial y}\right)$$

In the Los Alamos SMAC, but not the current version, the viscous contribution was neglected.

The no-slip condition at a rigid wall is only appropriate when the boundary layer is several cell widths thick. In the case of low viscosity flows, where the boundary layer is less than one finite difference cell in width, the no-slip condition forces an artificially large drag on the fluid. It then becomes more realistic to apply the following free-slip condition (with reference to Fig. 7.3)

$$u|_o = 0 \qquad \Rightarrow u_{i-\frac{1}{2},j} = 0$$

$$\frac{\partial v}{\partial n}\Big|_o = 0 \qquad \Rightarrow \qquad \begin{aligned} v_{i-1,j+\frac{1}{2}} &= v_{i,j+\frac{1}{2}} \\ v_{i-1,j-\frac{1}{2}} &= v_{i-1,j-\frac{1}{2}} \end{aligned}$$

$$\frac{\partial \psi}{\partial n}\Big|_o = 0 \qquad \Rightarrow \qquad \psi_{i-1,j} = \psi_{i,j}$$

Similar considerations apply to the tangential stress free surface condition. When modelling low viscosity flows, Chan and Street (1970) proposed that the free-surface velocity field be evaluated by extrapolating the internal velocity field. This may be achieved by using a second order extrapolation scheme. With reference to Fig. 7.4c this may be illustrated as follows:

$$v_E = 3v_1 - 3v_2 + v_3$$

$$u_E = 3u_1 - 3u_2 + u_3$$

In cases where it is not known, a priori, that there will be a large enough depth of fluid to use the extrapolation, the continuity condition should be used rather than the tangential stress condition.

7.6 Stability Considerations

Instabilities constitute the major problem of the MAC technique. Hirt (1968) presented an heuristic stability analysis in which he was able to investigate the truncation errors of the finite difference formulation in the original MAC by expanding each term in a Taylor series about some central point. This yielded the stability constraints

$$2\ \nu > \delta t\ u^2$$

where u is the maximum fluid speed and

$$2\ \nu > (\delta x)^2\ \frac{\partial u}{\partial x}$$

where $\frac{\partial u}{\partial x}$ is the maximum velocity gradient in the direction of flow. For small viscosity values, these conditions impose severe restrictions on δx, δt.

The finite difference form of the momentum convection terms used in the current form of SMAC eliminates the destabilising truncation error term present in the original MAC (see section 7.4). The above stability conditions have been found by several research workers to be unnecessarily restrictive. It is sufficient that the time interval be constrained only by the Courant stability condition

$$c\ \delta t < \frac{2\ \delta x\ \delta y}{\delta x + \delta y}$$

where c is the maximum surface wave speed and the diffusional stability condition

$$\nu\ \delta t \ < \ \frac{1}{2}\left(\frac{\delta x^2\ \delta y^2}{\delta x^2 + \delta y^2}\right)$$

In addition, the fluid must not be permitted to flow across more than one computational cell per time step

i.e. $$\delta t < \min\ \{\delta x/u_{max},\ \delta y/v_{max}\}$$

Instabilities may also occur due to insufficiently accurate treatment of the free surface boundary conditions. These result in a jagged surface profile after a large number of time steps. In the original MAC (and the current SMAC), the boundary conditions are applied at the centre of the surface cell rather than at the actual fluid surface. A number of authors have obtained more accurate results by applying the pressure conditions actually at the fluid surface. The free surface is located by a set of free surface marker particles. The pressure at the centre of a surface cell can then be determined either by the method of 'irregular stars' involving the use of irregular leg lengths in the definition of the finite difference Laplacian operator (Chan and Street (1970)) or by an interpolation involving the pressure of an adjacent FUL cell (Nichols and Hirt (1971)). The method of 'irregular stars', in particular, requires a large amount of additional computer storage. Both methods also require that the pressure be calculated explicitly in FUL cells and are thus not suitable for incorporation into the SMAC method.

7.7 Other Water Wave Calculations

Chan and Street (1970) used the MAC technique to study the run up on a vertical wall of a solitary wave on the surface of an inviscid fluid. They made certain improvements to the treatment of the surface boundary conditions. They used the 'method of irregular stars' to apply the pressure condition actually on the surface, together with the inviscid boundary conditions described in section 7.5. These alterations produced a considerably less jagged surface profile than the original MAC. They found that the Courant stability criterion was necessary and sufficient to determine δt for stable calculations. The surface particles were moved by means of a second order interpolation scheme rather than the original linear area weighting scheme. This caused a significant improvement only in the very curved portions of the free surface.

The initial conditions for the solitary wave were given by a second order perturbation analysis (Laitone (1960)). This analysis is only valid for small amplitude waves. For the case $\eta_0/h_0 = 0.5$, Laitone's initial conditions caused the condition D = 0 to be seriously violated in certain parts of the flow region. The resulting wave also propagated with an erroneous speed. Consequently, the initial conditions for waves with $\eta_0/h_0 > 0.4$ were given by a highly accurate numerical steady state solution. The numerical solutions agreed well with experimental and analytical results.

Smithers (1978) performed similar calculations, together with simulations of the progress of a solution over a sudden change in bed height and the interaction of two solitary waves of different heights travelling in opposite directions. Although his results were in reasonable agreement with theoretical predictions, there was an overall attenuation of the wave height and an increase in jaggedness of the surface profile after many time steps. Smithers blamed these errors on the setting up of the initial velocities at discrete locations rather than on a continuous basis and on the errors in Laitone's approximation for waves with $\eta_0/h_0 = 0.5$. He used the linear scheme for surface particle movement.

Chan (1975) used the combined Lagrangian and Eulerian scheme GALE to repeat the numerical simulations of Chan and Street. He created the solitary wave by moving the left boundary to the right with a displacement which was a hyperbolic tangent function of time. This was an exact anology with experimental procedure and eliminated the doubt as to the validity of Laitone's approximation. The results were in excellent agreement with the experiments of Camfield and Street (1967) and with the numerical solution of Chan and Street.

GALE was also used to model the Kelvin-Helmholtz instability of an interface separating two inviscid fluids of different densities in a gravitational field. The initial condition was the linear solution for a periodic wave train with $\eta_o/\lambda = 0.005$, $\eta_o/h_o = 0.025$ (see Fig. 2.3). The solution became unstable once the wave crest had formed an angle very close to 120^o and a height to length ratio of 0.147. This agrees well with the Stokes solution of 120^o angle for waves of maximum amplitude and a theoretical ratio of height to length of 0.143.

7.8 Modelling Large Disturbance Waves Using SMAC

The use of the MAC technique for modelling large disturbance waves in vertical annular two phase flow is considerably more ambitious than the soliton investigations carried out by Chan and Street and Smithers. 2D cartesian co-ordinates are used. The system is treated as a one phase laminar incompressible film flow with imposed surface stresses. The perturbation surface stresses are calculated according to Benjamin's quasi-laminar theory (see sections 3.2, 3.3).

There are advantages in using SMAC to model disturbance waves. The full Navier-Stokes equations are used and thus inertia effects are included. The solution is time dependent. Also, there is no restriction to small amplitude waves on the surface of the liquid.

Unfortunately there are many difficulties associated with the approach.

1. The basic flow is driven by the surface shear stress and the effect of the upper fluid is contained in the surface boundary conditions. Thus the treatment of the free-surface, the most unsatisfactory part of the MAC

technique, is crucial.

2. According to the linear stability analysis (Chapter 4), the system is basically unstable. Thus it is possible that small perturbations in the free surface, caused by the numerical method, will grow disasterously and swamp the solution.

3. The perturbation surface stresses are calculated according to Benjamin's theory, and are really only valid for infinitesimal disturbances. They also only apply to very shallow sloping waves.

4. Chan and Street (1970) and Smithers (1976) used Laitones second order expansion expressions for the initial velocity distribution. They found that, for waves with $\eta_o/h_o > 0.4$, the subsequent behaviour of the solution was affected. In the case of two phase annular flow, an analytical solution is only available to the first order in η_o/h_o and/or zero order in $Re_L h_o/L$. The calculation of a more accurate velocity distribution would be a formidable task.

5. It is not clear what initial surface profile it is sensible to adopt.

The set up for a wave run in vertical two phase flow is shown in Fig. 7.5. The inlet velocity was prescribed to be the undisturbed film velocity profile and a continuative outflow was used.

The lengths, velocities and stresses in the problem were non-dimensionalised with respect to the undisturbed film thickness h_o, the average undisturbed film velocity u_o and $\rho_L u_o^2$ respectively. With this non-dimensionalisation

$$NU = \frac{\nu_L}{u_o h_o} \qquad GX = \frac{-gh_o}{u^2}$$

Since it is known experimentally that the maximum wave slope is only a few per cent, δy was taken to be 0.1 while δx was taken to be 1.0 or 2.5.

For liquid Reynolds numbers (and hence $^1/NU$) in the experimental range

50-100, the boundary layer thickness lies between 0.1 and 0.14, i.e. 1-1½ cell widths. This is on the borderline between the suitability of adopting free-slip or no-slip boundary conditions. It was decided to use no-slip boundary conditions since the flow is driven by the imposed surface shear stress.

7.9 Interfacial Boundary Conditions

The flow in the liquid film in annular two phase flow is driven by the normal and tangential stresses exerted by the gas core on the interface. These are combinations of constant stresses exerted on the undisturbed surface and perturbation stresses which depend on the surface profile. Any constant component of pressure gradient was incorporated into GX. A new cell variable TAUS(I,J) = τ_s/NU was introduced and initially set equal to CTAUS = τ_{so}/NU where τ_{so} is the constant undisturbed surface shear stress.

The perturbation surface stresses were calculated according to Benjamin's theory (see section 3.3) using the numerical integration technique described by Green (1969) p.111. The range of integration $[a,b]$ was set equal to $[0, \text{IBAR} \times \delta x]$ with t_j corresponding to the x co-ordinate of the $(j + 1)^{th}$ surface marker particle. The stresses were first calculated assuming a constant surface roughness corresponding to that for the undisturbed surface $\bar{h} = 1.0$. Later the surface friction factor $C_f(x)$ was assumed to be a function of the film thickness $h(x)$. A new variable CFBAR = $C_f(x)$/0.005 was calculated for each surface marker particle according to the Shearer-Nedderman correlation (see section 5.3). The film thickness at each surface cell centre was calculated by a linear interpolation on the surface marker particle positions. The corresponding CFBAR value was used in the calculation of the undisturbed surface stress CTAUS. The values of CFBAR at the surface marker particles were also incorporated into the integrand in the perturbation shear stress integral.

During the routine for the calculation of the surface perturbation stresses, $h'(t_j)$, $h''(t_j)$ are calculated. Thus it would be straightforward (see Daly (1969) and Foote (1973)) to incorporate surface tension into the normal stress boundary condition through the addition of a term

$$\frac{\sigma h_{xx}}{(1+h_x^2)^{\frac{3}{2}}}$$

However, in the case of vertical annular flow the ratio of the surface tension term to the pressure perturbation term is of the order 10^{-3}. It was therefore neglected.

The viscous form of the boundary conditions was used in the disturbance wave calculations. The tangential free surface stress condition is

$$\frac{\partial u_n}{\partial m} + \frac{\partial u_m}{\partial n} = \frac{\tau}{\mu}s$$

(see Fig. 7.6). When the surface is at an angle θ to the horizontal, this expression becomes

$$-2\cos\theta\sin\theta \frac{\partial u}{\partial x} + (\cos^2\theta - \sin^2\theta) \frac{\partial u}{\partial y}$$

$$+ (\cos^2\theta - \sin^2\theta) \frac{\partial v}{\partial x} + 2\cos\theta\sin\theta \frac{\partial v}{\partial y} = \frac{\tau}{\mu}s$$

In the original SMAC method, the slope of the free surface in corner cells was taken as cutting the cell at 45^0 (see section 7.5), leading to $\tan\theta = \frac{\delta y}{\delta x} = 1$ and the boundary condition

$$\frac{\partial v}{\partial y} - \frac{\partial u}{\partial x} = \frac{\tau}{\mu}s$$

For vertical annular flow $\frac{\delta y}{\delta x} \doteq 0.04$ or 0.1. Thus it is more appropriate to use the boundary condition

$$\frac{\partial v}{\partial x} + \frac{\partial u}{\partial y} = \frac{\tau_s}{\mu} \qquad (7.3)$$

Similar considerations apply to the normal stress boundary condition.

In SMAC models of large amplitude waves, the front of the wave tended to steepen so that a SUR cell was directly above another SUR cell. In this region τ_s varies considerably. It was found that if either of the above expressions was used to evaluate the 'just outside' velocity v, significant errors in the movement of the marker particles developed leading to an extremely jagged surface profile after a few time steps. Smooth profiles were obtained by imposing the boundary conditions

$$\frac{\partial u}{\partial x} = 0 = \frac{\partial v}{\partial y}$$

in such cells.

The integral expressions for the perturbation stresses are extremely sensitive to any jaggedness in the surface profile. This sensitivity proved to be the most serious limitation in the modelling of the flow using the SMAC method.

7.10 Initial Conditions

The choice of initial conditions presented another serious problem to the use of SMAC for modelling disturbance waves. There is no accurate steady solution as in the inviscid soliton problem studied by Chan and Street (1970). An approximate initial velocity profile was determined and it was hoped that the velocity profile under the wave would settle down to the correct value in a few cycles before the surface profile changed significantly.

At first the perturbation velocities according to the linear theory

$$u' = \frac{2c'}{h_o} h(x)$$

$$v' = \frac{-c'}{h_o^2} y^2 h'(x)$$

were used as initial conditions. However, when the height dependent roughness was introduced, the author found that more accurate conditions could be specified by assuming a 'self-similarity' profile within the wave. The film thickness h(x) at the x co-ordinate of the centre of each surface cell was determined, together with the corresponding scaled surface shear stress $T_s(x)$. The initial fluid velocity at the cell centre (x,y) was then taken to be

$$u = (T_s(x) - Gh)y + \frac{G}{2} y^2$$

where $G = \frac{-\bar{g}}{NU} x$

$$v = 0$$

It was found that the velocity profile settled down in about 3 cycles in wave calculations.

Another problem was the suitable choice of an initial wave profile. Two profiles were considered.

$$\text{Poisson wave} \quad y = A(L-x)e^{-\lambda(L-x)} \quad x<L$$

$$\text{Cos wave} \quad y = A(1+\cos\pi\lambda x) \quad -{}^1/\lambda \le x \le {}^1/\lambda$$

It was particularly convenient for programming to choose an initial wave profile given by an analytic expression. The Poisson wave was chosen because, according to kinematic wave theory, any initial disturbance will eventually tend to a triangular profile. The shape of the Poisson wave also vaguely resembles that of a typical disturbance wave found in experiments, particularly those of Miya (1970). The Cos wave was chosen as an example of a symmetrical wave, for which the progress according to kinematic wave theory could be easily calculated.

In experiments the heights of disturbance waves are found to be 4-5 times the base film thickness. However, in the numerical simulations it was necessary to ensure that

1. The front portion of the wave spanned a sufficient number of cells to be represented reasonably accurately.

2. The wave slope at the front of the wave was sufficiently small that the horizontal surface shear stress boundary condition (7.3) was still appropriate.

3. The wave had decayed sufficiently at the inlet for no instability to develop there that swamped the main disturbance. In early runs, with insufficient decay, instabilities in the surface profile developed near the inlet which had large values for $h''(x_n)$. The instabilities tended to dominate the integrand in the calculation of the surface stresses leading to erroneous results.

4. The number of computing cells was not so large as to make the computing time excessive.

It was found that a reasonable compromise was obtained by taking the Poisson wave to be $y = 0.1359\ (80.0-x)e^{(-0.1(80.0-x))}$ with 52 cells in the x direction ($\delta x = 2.5$) and 20 in the y direction. The amplitude of this wave is half the film thickness. Although results could also be obtained for waves with $1\frac{1}{2}$ times this amplitude, the solution for the higher waves was found to break down after only a few cycles.

Thus the waves used in the numerical computations, although still non-linear, were considerably smaller than those found in experiments. It was hoped, however, that the smaller waves would still portray the correct qualitative behaviour.

7.11 Results

The SMAC results presented in this section are mainly for the case $G_G = 63.4\ kgm^{-2}s^{-1}$, $G_L = 11.4\ kgm^{-2}s^{-1}$. This gas flow rate lies just outside the asymptotic region while the liquid flow rate lies just above the disturbance wave inception value.

In the first numerical simulations, it was assumed that the system had a uniform surface roughness. The constant value τ_{so}, calculated from the Shearer-Nedderman correlation (see section 5.3) was used for CTAUS and in the expression (3.6) for the perturbation shear stress. A Poisson wave profile with a maximum height of 0.5 h_o was used as an initial condition.

Fig. 7.7 shows the wave profile for the case $G_G = 63.4\ kgm^{-2}s^{-1}$, $G_L = 11.4\ kgm^{-2}s^{-1}$ together with the surface and wall shear stresses after 18 cycles (t = 0.9). Fig. 7.8 shows the corresponding SMAC plot. The wave has grown by 0.15% and is travelling at a speed of about 1.36. The front of the wave has become slightly steeper and just in front of the wave the film thickness drops slightly below the unperturbed value. As t increases, this depression becomes more marked and the wave slope steepens still further until the solution breaks down in about 30 cycles. There is a sudden drop in wall shear stress in the front of the wave to a value below that in the unperturbed film. This drop occurs further upstream than the corresponding drop in surface shear stress. From the cell centre velocity plot it can be deduced that the wave is moving more slowly than the fluid particles.

Fig. 7.9 shows the SMAC plot at t = 0.2 for an equivalent calculation with $G_G = 31.7$, $G_L = 6.45$. There is a re-circulation zone and negative wall stress under the crest of the wave. The wave did not move forward and the solution broke down after 18 cycles.

In Chapter 3 it was shown that the perturbation shear stress calculated according to Benjamin's theory agreed well with measurements over a solid (and hence uniformly rough) wave. However, comparison with Miya's (1970) results for stresses over a water wave shows that the assumption of constant roughness gives the calculated stress to be an order of magnitude less than that found in experiment. Also the SMAC simulations described above, assuming constant roughness, predicted the speed of large waves to be less than that of the surface of the base film, in contrast to experimental results.

In their numerical model, Gent and Taylor (1976) took into account the roughness variation over a wave caused by the presence of much smaller gravity and capillary waves riding on the dominant waves. These are generated by a non-linear transfer of energy from the dominant wave and ~~are~~ are steepest just forward of the wave crest (Longuet-Higgins (1969)). They considered flow over sinusoidal (stationary) waves and hypothesised that the maximum roughness occurred at about $^{\pi}/4$ forward of the wave crest. They also assumed that the variation of roughness height from its mean value was sinusoidal. It would be difficult to use such a scheme with non-sinusoidal waves.

For their shallow waves, Miya et al. (1971) assumed that the surface roughness at any height h in the wave profile was the same as would occur for a flat film of thickness h. They assumed, based on experimental results, that the roughness increased linearly with $Re_L(h)$.

The author adopted an approach, similar to that of Miya, for vertical annular flow. The roughness coefficient was calculated using the Shearer-Nedderman correlation. This correlation gives a hvG_L graph in the ripple region which agrees well with experiment, particularly at high gas flow rates (see section 5.3). It was assumed that the correlation reasonably represented the roughness caused by ripples on the surface of disturbance waves.

The variation in surface roughness with height was incorporated both into CTAUS and into the expression for the perturbation shear stress as described in section 7.9. Fig. 7.10 shows the new surface and wall shear stresses for $G_G = 63.4$ kgm^{-2}s^{-1} after 18 cycles. Fig. 7.11 shows the corresponding

SMAC plot. The wave amplitude has grown by 2.1% and the speed is about 2.23. The front of the wave has again become steeper but the front edge of the wave has become smoothed out with no depression below the unperturbed film thickness. As t increases, the wave continues to grow and steepen until the solution breaks down after 36 cycles. There is again a sudden drop in the wall shear stress in the front of the wave slightly upstream of the corresponding minimum in the surface shear stress. Finally, from the cell centre velocity plot it can be seen that, in this case, the wave is moving faster than the fluid particles.

Introduction of the increase of surface roughness with film thickness removes any re-circulation zones for lower gas flow rates.

The effect of the perturbation surface stresses on the wave profile and wall shear stress was studied for the case $G_G = 63.4$ kgm^{-2}s^{-1}. Neglecting the surface shear stress perturbation means that the surface shear stress is now in phase with the wave height. It was found that the wall shear stress still had the same qualitative behaviour. There was a significant quantitative difference only in the front of the wave. In 18 cycles the wave increased in height by 2.1% with speed about 2.3.

The effect of neglecting the pressure perturbation was more significant as shown in Fig. 7.12. The wave increased in height by only 1.7% in 18 cycles and had a speed of about 1.97. There was no longer a sudden decrease in the wall shear stress in the front of the wave.

Miya's (1970) measurements of the wall shear stress under a large amplitude wave of similar form to the Poisson wave showed similar qualitative behaviour to the SMAC calculations. Miya suggested relaminarisation of the flow due to the strong negative pressure gradient near the crest of the wave as a possible mechanism for stress relaxation. The SMAC results, however, show that for a completely laminar flow the same phenomenon can occur due to the sudden decrease in negative pressure gradient in the front of the wave.

The parameter Γ was calculated for the Poisson wave with $G_G = 63.4$ $kgm^{-2}s^{-1}$ at $t = 0.9$ from the computed velocity profile and also assuming a similarity profile. The value of Γ assuming a similarity profile was between 1.347 and 1.348 throughout the wave. The computed Γ was 1.35 to 2 decimal places throughout the back part of the wave. In the front, however, Γ was considerably higher, reaching 1.48.

Comparison between the average velocity according to the similarity profile and the computed value showed good agreement. There was a slight discrepancy in the non-disturbed film value. This could be due to the artificially large drag on the fluid at the wall due to the application of non-slip boundary conditions (see section 7.5), or due to a 4% artificial increase in viscosity resulting from upwinding (see section 7.4).

SMAC was used to follow the progress of the initially summetrical wave

$$h = \begin{cases} h_o + 0.25\, h_o(1+\cos\pi\lambda x/h_o) & \frac{-h_o}{\lambda} \leq x \leq \frac{h_o}{\lambda} \\ 0 & \text{o.w.} \end{cases}$$

The results were compared with the behaviour of the wave calculated according to kinematic wave theory (see Chapter 6). According to the lowest order theory, such a wave for $G_G = 63.4$ $kgm^{-2}s^{-1}$ should develop an infinite slope, corresponding to breaking, after 53 cycles. The breaking point should be at $\bar{h} = 1.288$. Figs. 7.13a, b, c and the corresponding SMAC plots, Figs. 7.4a, b, c show the progress of the wave. The wave developed a triangular profile as predicted but also grew significantly in amplitude. The back of the wave was correspondingly steeper. The speed of the wave was much less than predicted. The SMAC calculation broke down after 48 cycles, about 10^{-2} seconds. At this time the steepest portion of the wave was at $\bar{h} \simeq$ 1.29.

Figs. 7.4a, b show the progress of a cos wave with no perturbation surface stresses. The wave is slower and the front of the wave is less steep. The wave took longer to break. The wave has still increased in height.

The increase in amplitude is due to the increase in surface roughness with film thickness. With reference to section 4.4, there is a large positive component of Σ_I which acts as a destabilising term in the expression for C_I.

All the SMAC calculations described in this section have been for waves with amplitudes of 0.5 h_o. The use of SMAC to model larger amplitude waves is only restricted by the computer time associated with a large increase in the number of cells in the computing mesh. If the Shearer-Nedderman correlation is used to determine the surface roughness for all film thicknesses h, there will be no maximum admissable wave height.

A difficulty of the SMAC method is that there are no experimental results with which the results can be directly compared. Direct comparison with Miya's results is not possible since in his system $Re_L \simeq 3 \times 10^2$. For such a large Reynolds number it would be appropriate to use inviscid boundary conditions and surface shear stresses could not be imposed.

CHAPTER 8. Discussion and Conclusions

8.1 Further Thoughts on the Integral Method

The application of lowest order kinematic wave theory to the modelling of large amplitude waves in vertical annular flow was discussed in Chapter 6. The theory predicts too high a speed for both waves and injected pulses (see sections 6.5, 6.6). SMAC calculations (section 7.11) for the time dependent behaviour of a hump of liquid show that its speed is again less than predicted by kinematic wave theory. The disturbance also increases significantly in height. Thus, like experiment, SMAC produces wave speeds that are considerably less than predicted for a prescribed peak height.

The lowest order theory models the front of a wave by a kinematic shock. A more detailed flow description in the shock region, including the effects of inertia and pressure, is obtained by calculating steady solutions of the higher order system (2.25), (2.26) with $\beta = \pi/_2$. In (2.26), τ_w, τ_s, Γ and $dp_{s/dx}$ have to be specified.

Comparison with experiments (see Chapter 3) provides evidence that over a non-breaking wave of constant roughness, Benjamin's theory gives reasonable expressions for τ_s, $dp_{s/dx}$. Further evidence (see sections 5.3, 7.11) suggests that a better representation for vertical annular flow is given by Benjamin's theory in conjunction with the Shearer-Nedderman correlation for increasing roughness with increasing film thickness. However, the correlation is not applicable to very large film thicknesses (see section 6.6).

Miya assumed τ_w to be a function of the film thickness alone. However, SMAC calculations (section 7.11) and experimental results suggest that, particularly in the front of a wave, τ_w is also a function of $dp_{s/dx}$.

The specification of Γ depends on whether laminar or turbulent film flow is assumed. Arguments relating to this decision are outlined in section 2.2. Γ is 1.0 for uniform flow and $^4/_3$ for shear flow. For the case $G_G = 63.4\ \text{kgm}^{-2}\text{s}^{-1}$, $G_L = 11.4\ \text{kgm}^{-2}\text{s}^{-1}$ used in the SMAC simulations described in Chapter 7, $\Gamma \simeq 1.35$. In these simulations the value of Γ calculated according to the 'self-similarity' assumption agreed well within the computed value under the back of the wave. In the front of the wave, however, the computed Γ was significantly larger.

Miya (see section 2.9) calculated a solution of the steady state integral equations for horizontal flow. τ_s, τ_w, Γ and $dp_{s/dz}$ were all calculated using the 'self-similarity' assumption. Attempts were made to compute a steady profile for vertical flow. For simplicity, the effect of gravity was neglected corresponding to a very high gas flow rate. The perturbation surface stresses were calculated according to Benjamin's theory. Γ and τ_w were calculated assuming a 'self-similar' shear profile throughout the wave. The problem reduced to the solution of an equation of the form:

$$p_1 h' + p_2 \frac{h'}{h^2} + p_3 \frac{(h-1)}{h^2}(p_7 - u) = \int_{-\infty}^{\infty} h'' \left[\frac{p_4}{|x-x'|^{8/21}} + p_5 \frac{\operatorname{sgn}(x-x')}{|x-x'|^{8/21}} \right] dx' + hp_6 \int_{-\infty}^{\infty} h'' \frac{\operatorname{sgn}(x-x')}{|x-x'|^{5/7}}\, dx'$$

where the p_i are constants.

Two methods of solution were tried - a variation on the shooting method (England (1975)) and a collocation method involving the numerical integration procedure described in section 3.3. The attempts failed. The zero solution was the only continuous steady solution found vanishing at $x = \pm \infty$.

The time dependent form of equations (2.25), (2.26) was also studied. The numerical method described in section 4.5 for the injection model was modified to deal with two simultaneous partial differential equations. At the n^{th} time step, the film thickness h was fixed and the $(n+1)^{th}$ value for the averaged velocity u_a was calculated. u_a was then fixed at its new value and the $(n+1)^{th}$ value of h calculated. The initial condition was a Poisson wave (see section 7.10). With a zero right-hand side in the momentum equation, the wave initially increased slightly in height. Then, as the wave moved along and spread out, the height gradually decreased. A second hump appeared slightly upstream of the wave peak. The profile remained smooth. For stresses corresponding to the case $G_G = 63.4$ kgm^{-2}s^{-1}, $G_L = 11.4$ kgm^{-2}s^{-1}, the wave rapidly doubled in amplitude and then 'broke'. For perturbation pressure coefficients less than about half the physical values, the behaviour of the wave was similar to the case of no right-hand side; the larger the perturbation pressure coefficient, the greater the initial increase in disturbance height. Thus the behaviour of the wave was very sensitive to the pressure perturbations. The incorporation of an increase in surface roughness with increasing film thickness would be expected to hasten breaking.

For high gas flow rates, the relative magnitude of the stabilising gravitational term present in Miya's system is negligible. The author would expect any attempt at a steady solution of his equations to fail as in the vertical case. Miya only managed to obtain a steady solution due to the condition (2.38) in which dh/dz is forced to vanish for h equal to the experimentally measured peak height. Kinematic wave theory predicts wave breaking in Miya's system due to the increase in roughness and average velocity with film thickness. Wave breaking is associated with flow separation (section 3.1). It is thus surprising that Miya did not find any experimental evidence of wave separation.

Whitham's analysis leading to a criterion for the existence of a continuous solution in the higher order system breaks down when the system is unstable, according to linear stability theory, as in the case of vertical annular flow. Both lowest order kinematic wave theory and the SMAC simulations predict wave breaking on a very short time scale. Pressure drop measurements of Shearer and Nedderman (1965) also indicate that disturbance wave breaking and separation may be occurring. Thus the author expects shocks still to occur in the higher order theory. An approach could be to solve the steady state integral equations and fit in shocks as in Dressler's solution (section 2.9). Unfortunately, Benjamin's theory for the perturbation stresses breaks down when there is a discontinuity or separation over the wave. Also, since τ_w and Γ depend on $\frac{dp_s}{dx}$ as well as on h, they will contribute to the shock condition and must be correctly specified. Thus, in order to extend the kinematic wave theory model for disturbance waves, new expressions will have to be derived for τ_w, τ_s, $dp_{s/dx}$ and Γ.

Disturbance waves have an average height of about 5.3 times the mean film thickness (Hewitt and Hall-Taylor (1970)). The average wave height decreases with increasing gas flow rate. There must be some mechanism limiting the increase in amplitude predicted by SMAC and the linear stability theory. This may be due to a balance between the rate of increase in height, and the rate of decrease in height due to the breaking front propagating back along the asymptotic triangular form (section 6.4). Other explanations could include a different specification of increasing roughness with height over a wave than that assumed or a stabilising force due to some turbulent interaction between the gas core and the film which has not been accounted for.

8.2 Conclusions

In Chapter 2, a number of approaches for modelling disturbance waves were discussed. None of them was completely satisfactory. Some were restricted to small amplitudes (sections 2.5, 2.6), some broke down for vertical flow due to the lack of a restoring term (section 2.6) while others were impossibly complicated for the case of vertical two-phase flow (section 2.7).

In Chapter 3, the difficulty of modelling the stresses exerted by the turbulence gas core on the liquid film surface was discussed. Benjamin's theory was shown to provide reasonable expressions for the perturbation stresses. The theory is 'quasi-laminar' and restricted to long wave lengths but has the advantage that the expressions have a reasonably simple analytic form. The roughness of the film surface was shown to increase with film thickness (Chapter 5). This relationship is difficult to specify. Evidence has been given (section 5.3) to suggest that, for reasonably small film thicknesses, the Shearer-Nedderman correlation may be used.

A linear stability analysis (Chapter 4) showed that the interface is always unstable and that the linear theory does not provide a criterion for disturbance wave inception. The author hypothesised that, for low gas flow rates, inception is connected with the liquid behaviour near the inlet. For high gas flow rates it may be connected with turbulent interactions between the film and gas core.

The SMAC method has been developed to model the time dependent behaviour of waves in vertical two phase flow (Chapter 7). The author hopes that it will provide a useful tool for further research.

Kinematic wave theory was discussed in Chapter 5. This theory can incorporate experimental results. Comparisons of the lowest order theory with experiment and SMAC simulations show the importance of the neglected effects of the perturbation pressure, inertia and the wave amplification due to the increase in surface roughness with film thickness. Both SMAC and the lowest order kinematic wave theory discussed in Chapter 6 predict that a wave breaks in the order of 10^{-2} seconds.

The integral equations discussed in section 2.8 correspond to a higher order theory. Shocks are still expected in this higher order system. There is evidence to suggest that there is flow separation on the leeward side of a breaking wave. Benjamin's theory then breaks down and some other expressions are required to represent the interfacial stresses.

It is the author's opinion that the most suitable approach for the modelling of disturbance waves in vertical annular two-phase flow is that of kinematic wave theory. In order to apply a higher order theory, a more accurate specification of τ_s, τ_w, Γ, $dp_{s/dx}$ is required especially in the front of a wave. This in turn depends on more accurate experiments being conducted. It would be particularly useful if the wall shear stress profile under a wave could be measured. Comparison with SMAC results could provide a valuable check on the suitability of the various assumptions made particularly as regards the surface roughness. Such an experimental programme is planned at Harwell in the near future.

A further experimental investigation into wave inception criteria is now in progress at Harwell, beginning with a comparison of the inception curves obtained with different liquid injection devices.

Appendix 1: Interfacial Wave Profile Equation
Assuming the Long Wave Approximation

The equation corresponding to (2.24) for annular two-phase flow, assuming $\delta << 1$, is given by

$$h_t - Re_L h_x h^2 \{ A + \frac{5}{6} Bh + \frac{3}{4} Ch^2 + \frac{7}{10} Dh^3 + \frac{2}{3} Eh^4 \}$$

$$+h^3 \{ \frac{1}{3} A_x + \frac{5}{24} B_x h + \frac{3}{20} C_x h^2 + \frac{7}{60} D_x h^3 + \frac{2}{21} E_x h^4 \} = 0 \qquad \text{(A.1)}$$

where $A = p_{so,x} + (W\delta^2)h_{xx} + \frac{h_x}{F} \cos \beta$

$B = \frac{-Re_L}{F^2} \sin \beta \, h_t + Re_L \, \tau_{s,x,t}$

$C = \frac{-Re_L^2}{2F^2} \sin \beta \, h \, \tau_{s,x} + \frac{Re_L^2}{2} \tau_s \, \tau_{s,x}$

$D = \frac{Re_L^2}{2F^2} \sin \beta \, h \, \tau_{s,x,t} + \frac{Re_L}{2F^2} \sin \beta$

$E = \frac{-Re_L^2}{2F^2} \sin \beta \, \tau_{s,x,t}$

and $h = 1 + \eta$

Appendix 2: Numerical Solution of the Orr-Somerfeld Equation

The expansion method of solution of the Orr-Somerfeld equation described in section 4.3 is only valid for $kRe_L \ll 1$. The author has written a computer program to provide a numerical solution valid for larger values of kRe_L. The computation involves the method of multiple shooting and uses Harwell subroutine DD03AD.

The equations (4.14) were split into their real and imaginary parts and reduced to a new system of eight simultaneous real non-linear first order ordinary differential equations together with ten boundary conditions. The eigenvalue problem could then be cast in the form:

$$\frac{d}{dy}\,\underline{f}\,(y) = \underline{g}\,(y, \underline{f}\,(y), \underline{\mu}) \qquad (A.2)$$

$$\underline{h}(\underline{f}\,(-1), \underline{f}(0), \underline{\mu}) = 0 \qquad (A.3)$$

where $\underline{f} = (f, f', f'', f''', g, g', g'', g''')$

$\phi = f + ig$

$\underline{\mu} = (c_R, c_I)$

Initial values were given to ϕ, c_R, c_I and hence $\underline{f}$, $\underline{\mu}$ corresponding to the zero order solution in Yih's (1963) expansion (see section 4.3). The wave number k was fixed. The subroutine DD03AD improved iteratively on the approximations to $\underline{f}$ and $\underline{\mu}$ at shooting points (chosen automatically by the subroutine) $-1 = y_1 < y_2 < \dots < y_q = 0$. Runge-Kutta integrations were performed forwards and backwards from each shooting point to 'matching' points y_i' $i=1, \dots, q-1$ where $y_i \leq y_i' \leq y_{i+1}$. The iteration aimed for continuity at these points as well as satisfaction of (A.3).

The results for $kRe_L = 0.0966$ and suitable values for Π, Σ, W, G, T, k, Re_L were compared with the first order solution from the expansion method. The results agreed to within two significant figures. For values $kRe_L \sim 1$, the subroutine generally chose only two shooting points.

An alternative numerical solution method, described by Solesio (1977), involves the method of 'quadrature by differentiation'. This method expresses the integral

$$\int_0^1 f(x)\,dx$$

in the form

$$\frac{1}{C_0^n} \sum_{k=0}^{n-1} C_{k+1}^n \left[f^{(k)}(0) + (-1)^k f^{(k)}(1) \right] + \eta_n \qquad \text{(A.4)}$$

where $$C^n{}_k = \frac{(2n-k)!}{k!(n-k)!}$$

and the error term $\eta_n \simeq (-1)^n \sqrt{\frac{\pi}{n}} \frac{f^{(2n)}(\theta)}{2n!} (\tfrac{1}{2})^{2n+1}$

where $$0 \leq \theta \leq 1$$

It can be used to solve (4.14) in the following manner: First redefine the independent variable so that the undisturbed surface is at $y = 0$ and the wall is at $y = 1$. Next express ϕ in the neighbourhood of $y = 0$ by

$$\phi_0(y) = \sum_{j=0}^{N} a_j y^j$$

Substitute this expression into the Orr-Somerfeld equation and the boundary conditions at $y = 0$. Equate coefficients of powers of y. This leads to $N - 1$ linear equations in the $N + 1$ unknowns a_j. Choosing a_2, a_3 to be independent, the equations can be solved for the remaining a_j in terms of a_2 and a_3.

Repeat the above process with ϕ expressed in the neighbourhood of $y = 1$ by

$$\phi_1(y) = \sum_{y=0}^{N} b_j \ (y-1)^j$$

The b_j can be expressed in terms of b_2 and b_3. Now substitute for a_j, b_j into (A.4) with $f = \phi^{(m)}$ $m = 1, 4$; $N = n + 3$. This results in a homogeneous linear system in the four unknowns a_2, a_3, b_2, b_3. In order for the equations to have a non-trivial solution, the determinant of the matrix of coefficients must vanish. This gives a relationship between c and known parameters.

Solesio used Newton's iterative method to calculate c for the case of free film flow down an inclined plane. He used the zero order solution for c as an initial value. He obtained a relative accuracy of the order of 10^{-3} with n = 2.

Notation - Principal Physical Symbols

Symbol	Units	
c	ms^{-1}	wave speed
C_f		friction factor
F		Froude number $\frac{u_o}{\sqrt{gh_o}}$
g	ms^{-2}	acceleration due to gravity
g'	ms^{-2}	$g\cos\beta$
G		$\frac{gh_o^2}{u_o\nu_L}$
G_G	$kgm^{-2}s^{-1}$	gas mass flux per unit area tube cross section
G_L	$kgm^{-2}s^{-1}$	liquid mass flux per unit area tube cross section
h	m	film thickness profile
h_o	m	base film thickness
k		non-dimensional wave number
L	m	typical length in x direction
N_s	Nm^{-2}	surface normal stress
p_G	Nm^{-2}	gas pressure
p_L	Nm^{-2}	liquid pressure
P_s	Nm^{-2}	surface perturbation pressure
q	m^2s^{-1}	liquid flux u_ah
q_o	m^2s^{-1}	discharge coefficient $(c-u_o)h_o$
R_o	m	tube radius
Re_G		gas Reynolds number $\frac{U_GR_o}{\nu_G}$
Re_L		liquid Reynolds number $\frac{u_oh_o}{\nu_L}$
T		$Re_L\,\bar{\tau}$
u_a	ms^{-1}	liquid velocity profile averaged over film thickness
u_o	ms^{-1}	average film velocity

Symbol	Units	
U	ms^{-1}	primary velocity profile
U_G	ms^{-1}	average gas velocity
U_o	ms^{-1}	mainstream gas velocity
W		(Weber number)$^{-1}$ $\frac{\sigma}{\rho_L u_o^2 h_o}$
α	m^{-1}	dimensional wave number
β		angle of inclination of plane to horizontal
Γ		shape factor
δ		'shallow water' parameter $\frac{h_o}{L}$
ε		small amplitude parameter $\frac{\eta_o}{h_o}$
η	m	surface perturbation profile
η_o	m	amplitude of surface perturbation
λ	m	wave length
μ_G	$kgm^{-1}s^{-1}$	gas viscosity
μ_L	$kgm^{-1}s^{-1}$	liquid viscosity
ν_G	m^2s^{-1}	kinematic gas viscosity
ν_L	m^2s^{-1}	kinematic liquid viscosity
Π	Nm^{-3}	perturbation normal stress coefficient
ρ_G	kgm^{-3}	gas density
ρ_L	kgm^{-3}	liquid density
σ	kgs^{-2}	surface tension
Σ	Nm^{-3}	perturbation shear stress coefficient
τ_s	Nm^{-2}	surface shear stress

References

Ames, W. F., (1965) Non-linear Partial Differential Equations in Engineering, Academic Press Inc.

Amsden, A. A., Harlow, F. H., (1970a) J. Comp. Phys. 6 322-325.

Amsden, A. A., Harlow, F. H., (1970b) Los. Alamos Report LA-4370.

Azzopardi, B. J., Fryer, P. J., Freeman, G., (1979) UKAEA Report AERE-R9347.

Azzopardi, B. J., (1979) UKAEA Report AERE-R9483.

Banner, M. L., Melville, W. K., (1976) J. Fluid Mech. 77 825-842.

Barnett, T. P., Kenyon, K. E., (1975) Rep. Prog. Phys. 38 667-729.

Benjamin, T. B., (1957) J. Fluid Mech. 2 554-574.

Benjamin, T. B., (1959) J. Fluid Mech. 6 161-205.

Benjamin, T. B., (1967) Proc. Roy. Soc. A. 328 153-183.

Benn, D. N., (1978) UKAEA Report AERE-R9286.

Benney, D. J., (1966) J. Maths. Phys. 45 150-155.

Berbente, C. P., Ruckenstein, E., (1968) A.I.Ch.E.J. 14 772-782.

Brown, D. J., (1978) D. Phil. Thesis, Oxford Univ.

Browne, L. W. B., (1978) in 'Numerical Simulation of Fluid Motion' (J. Noye, ed), North-Holland Publishing Co., 223-247.

Camfield, F. E., Street, R. L., (1967) Dept. of Civil Eng. Technical Report No.81, Stanford Univ., California.

Chan, R. K. C., Street, R. L., (1970) J. Comp. Phys. 6 68-94.

Chan, R. K. C., (1975) J. Comp. Phys. 17 311-331.

Chorin, A. J., (1968) Math. Comp. 22 745.

Craik, A. D., (1966) J. Fluid Mech. 26 369-392.

Daly, B. J., (1969) J. Comp. Phys. 4 97-117.

Davis, R. E., (1970) J. Fluid Mech. 42 721-731.

Dressler, R. F., (1949) Comm. Pure Appl. Maths. 2 149-193.

England, R., (1975) Culham Report CLM-PDN 3/73.

Foote, G. B., (1973) J. Comp. Phys. 11 507-530.

Freeman, N. C., Johnson, R. S., (1970) J. Fluid Mech. 42 401-409.

Gent, P. R., Taylor, P. A., (1977) Bdry. Layer Met. 11 65-87.

Gill, L. E., Hewitt, G. F., Lacey, P. M. C., (1963) UKAEA Report AERE-R3955.

Gjevik, B., (1970) Phys. Fluids 13 1918-1925.

Green, C. D., (1969) 'Integral Equation Methods', Thomas Nelson and Sons Ltd.

Hall-Taylor, N. S., (1966) Ph.D. Thesis, Univ. of Cambridge.

Heidrick, T. R., Banerjee, S., Azad. R. S., (1977) J. Fluid Mech. 82 705-723.

Hershman, A., (1960) Ph.D. Thesis, Univ. of Illinois.

Hewitt, G. F., Nicholls, B., (1969) UKAEA Report AERE-R4506.

Hewitt, G. F., Hall-Taylor, N. S., (1970) 'Annular Two-Phase Flow', Pergamon Press.

Hirt, C. W., (1968) J. Comp. Phys. 2 339-355.

Hirt, C. W., Amsden, A. A., Cook, J. L., (1974) J. Comp. Phys. 14 227-253.

James, P. W., (1978) UKAEA Report AERE-R9080.

James, P. W., (1979) UKAEA Report AERE-R9368.

Jeffrey, H., (1924) Proc. Roy. Soc. A 107 189-206.

Jepson, T. C., Crosser, O. K., Perry, R. H., (1966) A.I.Ch.E. Journal 12 186-192.

Joseph, R. J., (1977) J. Phys. A: Math. Gen. 10 L225-L227.

Kapitza, P. L., (1964) 'Collected Papers of P. L. Kapitza (in English)', Macmillan, New York.

Kluwick, A., (1977) Acta Mechanica 26 15-46.

Krantz, W. B., Goren, S. L., (1970) Ind. Eng. Chem. 9 107.

Laitone, E. V., (1960) J. Fluid Mech. 9 430-444.

Lamb, H., (1932) 'Hydrodynamics', 6th edition, Cambridge University Press.

Lighthill, M. J., Whitham, G. B., (1955) Proc. Roy. Soc. A 229 281-316, 317-345.

Lin, S. P., (1969) J. Fluid Mech. 36 113-126.

Longuet-Higgins, M. S., (1969) Proc. Roy. Soc. A 311 371-389.

Mei, C. C., (1966) J. Maths. Phys. 45 266-287.

Miles, J. W., (1957) J. Fluid Mech. 3 185-204.

Miles, J. W., (1980) 'Annual Review of Fluid Mechanics' 12 11-43.

Miura, R. M., (1976) SIAM Review 18 412-459.

Miya, M., (1970) Ph.D. Thesis, Univ. of Illinois.

Miya, M., Woodmansee, D. E., Hanratty, T. J., (1971) Chem. Eng. Sci. 26 1915-1931.

Nash, B. A., (1978) M.Sc. Dissertation, Oxford Univ.

Nash, B. A., (1980) UKAEA Report AERE-R9838.

Nichols, B. D., Hirt, C. W., (1971) J. Comp. Phys. 8 434-448.

Nye, J. F., (1960) Proc. Roy. Soc. A 256 559-584.

Pashniak, D. W., (1969) Ph.D. Thesis, Univ. of Washington.

Rae, J., (1975) UKAEA Report AERE-TP611.

Rivard, W. C., Farmer, D. A., Butler, T. D., O'Rourke, P. J., (1973) Los Alamos Report LA-5426.

Shearer, C. J., (1964) Ph.D. Thesis, Univ. of Cambridge.

Shearer, C. J., Nedderman, R. M., (1965) Chem. Eng. Sci. 20 671-683.

Shkadov, V., (1967) Izv. Akad. Nauk. Ser. Mekh., Zhidk i Gaza 1 43.

Smithers, J., (1978) Ph.D. Thesis. Newcastle Univ.

Solesio, J. N., (1977) Report CEA-R4835, Centre D'Etudes Nucléaires de Grenoble, Service des Transfers Thermiques.

Stewart, R. W., (1970) J. Fluid Mech. 42 733-754.

Stoker, J. J., (1957) 'Water Waves', Interscience Publishers Ltd.

Telles, A. C. da S., (1968) Ph.D. Thesis, Univ. of Houston.

Thomas, H. A., (1940) Proc. of Hydraulics Conf., Univ. of Iowa.

Thorsness,C. B., Morrisroe, P. E., Hanratty, T. J., (1978) Chem. Eng. Sci. 33 579-592.

Thwaites, G. R., Kulov, N. W., Nedderman, R. M., (1976) Chem. Eng. Sci. 31 481-486.

Townsend, A. A., (1972) J. Fluid Mech. 55 719-735.

Viecelli, J. A., (1969) J. Comp. Phys. 4 543-551.

Wallis, G. B., (1969) 'One-Dimensional Two-Phase Flow', McGraw-Hill.

Whalley, P. B., Hewitt, G. F., Hutchinson, P., (1973) UKAEA Report AERE-R7521.

Whalley, P. B., Hewitt, G. F., Azzopardi, B. J., Pshyk, L., (1977) UKAEA Report AERE-R8787.

Whitham, G. B., (1974) 'Linear and Non-linear Waves', John Wiley and Sons.

Woodmansee, D. E., (1968) Ph.D. Thesis, Univ. of Illinois.

Woodmansee, D. E., Hanratty, T. J., (1969) A.I.Che.J. 15 712-715.

Wu, J., (1968) J. Fluid Mech. 34 239-252.

Yih, C-S., (1963) Phys. Fluids 6 321-334.

LIST OF TABLES

Run Number	G_G $kgm^{-2}s^{-1}$	G_L $kgm^{-2}s^{-1}$	Estimated G_{LE} $kgm^{-2}s^{-1}$	Experimental hp μm	Experimental c ms^{-1}	Calculated c ms^{-1}
139	15.9	55.5	17.5	3080	2.32	2.84
156	31.7	15.9	1.3	1350	2.16	2.85
157	31.7	31.7	4.8	2030	2.59	4.05
142	31.7	79.3	18.4	2250	2.8	5.27
146	47.6	15.9	3.2	1000	2.80	3.81
144	47.6	31.7	8.0	1100	3.02	4.32
145	47.6	79.3	28.6	1280	3.29	5.51
148	63.5	31.7	11.1	875	3.44	4.89
149	63.5	79.3	41.2	1080	3.93	6.48
150	79.3	31.7	11.1	650	3.84	4.89
159	79.3	55.5	27.0	875	4.05	6.34
152	79.3	79.3	41.2	1050	4.08	7.39

TABLE 2.1. COMPARISON BETWEEN THE EXPERIMENTAL WAVE SPEEDS OF HEWITT AND NICHOLLS (1968) AND THE CALCULATED VALUES OF JAMES (1979).

Run	F^2	$\tilde{T}$	h_p/h_o				
			experiment	Miya's hydraulic shock	hydraulic shock including pressure	Miya's modified theory	modified theory including pressure
430	16.8	1.53	2.05	5.31	4.08	2.17	2.10
876	20.1	1.17	2.27	5.86	5.41	2.87	2.77
410	29.3	1.75	2.57	7.16	6.57	2.98	2.92
386	44.3	2.11	3.01	8.93	8.31	3.55	3.46
449-4	42.6	1.98	2.91	8.74	8.18	3.60	3.48

TABLE 2.2. COMPARISON BETWEEN EXPERIMENTAL AND CALCULATED VALUES OF h_p/h_o.

G_G $kgm^{-2}s^{-1}$	G_L $kgm^{-2}s^{-1}$	Average Film Thickness $10^{-4}m$
31.72	2.38	1.96
	3.17	2.29
	3.97	2.51
	4.76	2.66
	5.55	2.75
	6.34	2.88
39.65	3.17	1.56
	3.97	1.65
	4.76	1.92
	5.55	2.14
	6.34	2.25
	7.14	2.41
47.58	1.59	0.99
	2.38	1.10
	3.17	1.22
	3.97	1.32
	4.76	1.46
	5.55	1.56
	6.34	1.70
	7.93	1.90
63.40	1.59	0.65
	2.38	0.79
	3.17	0.88
	3.97	0.87
	4.76	0.89
	5.55	1.02
	6.34	1.07
	7.14	1.16
	7.93	1.25
	8.72	1.55
79.30	3.17	0.72
	4.76	0.79
	6.34	0.92
	7.93	1.09
	9.52	1.10

TABLE 5.1. AVERAGE FILM THICKNESS RESULTS

G_G $kgm^{-2}s^{-1}$	G_G $kgm^{-2}s^{-1}$	Injection time s	Time for travel between probes (0.88m apart) s
39.65	2.38	0.207	2.80
	3.17	"	2.78
	3.97	"	2.40
	4.76	"	1.92
	5.55	"	1.5
47.58	3.17	0.207	2.20
	3.97	0.206	2.00
	4.76	0.208	1.70
	5.55	"	1.40
	6.34	"	1.40
63.40	3.17	0.207	1.58
	3.97	"	1.45
	4.76	"	1.32
	5.55	0.208	1.24
	6.34	0.207	1.08
79.30	1.59	0.216	1.90
	3.17	"	1.40
	3.97	0.204	1.30
	4.76	"	1.25
	5.55	"	1.10
	6.34	0.203	1.10
	7.93	"	1.00

TABLE 5.2. INJECTED PULSE RESULTS.

G_G $kgm^{-2}s^{-1}$	G_L $kgm^{-2}s^{-1}$	Average film speed ms^{-1}	Kinematic wave speed c_o ms^{-1}	Average pulse speed ms^{-1}
39.65	2.38	...	...	0.31
	3.17	...	...	0.32
	3.97	0.21	0.75	0.37
	4.76	0.24	0.79	0.46
	5.55	0.27	0.83	0.59
47.58	3.17	0.22	0.85	0.4
	3.97	0.26	0.88	0.44
	4.76	0.30	0.94	0.52
	5.55	0.33	1.01	0.63
	6.34	0.36	1.07	0.63
63.40	3.17	0.30	1.06	0.56
	3.97	0.38	1.12	0.61
	4.76	0.40	1.20	0.67
	5.55	0.44	1.29	0.71
	6.34	0.48	1.38	0.81
79.30	1.59	...	...	0.46
	3.17	0.41	1.26	0.63
	3.97	0.43	1.34	0.68
	4.76	0.48	1.44	0.70
	5.55	0.54	1.56	0.80
	6.34	0.58	1.66	0.80
	7.93	0.67	1.88	0.88

TABLE 6.1. COMPARISON BETWEEN KINEMATIC WAVE THEORY AND RESULTS OF PULSE EXPERIMENTS.

Run	Experimental Conditions		Experimental Wave Properties		Theoretical Wave Speeds	
	G_G $kgm^{-2}s^{-1}$	G_L $kgm^{-2}s^{-1}$	h_p μm	c ms^{-1}	James c ms^{-1}	Nash c ms^{-1}
156	31.7	15.9	1350	1.64	2.85	2.073
157	31.7	31.7	2030	2.59	4.05	2.816
142	31.7	79.3	2250	2.8	5.27	3.023
150	79.3	31.7	650	3.84	4.89	25.28

TABLE 6.2. COMPARISON BETWEEN EXPERIMENTAL DATA OF HEWITT AND NICHOLLS (1968) AND THEORETICAL PREDICTIONS OF JAMES (1979) AND NASH.

LIST OF FIGURES

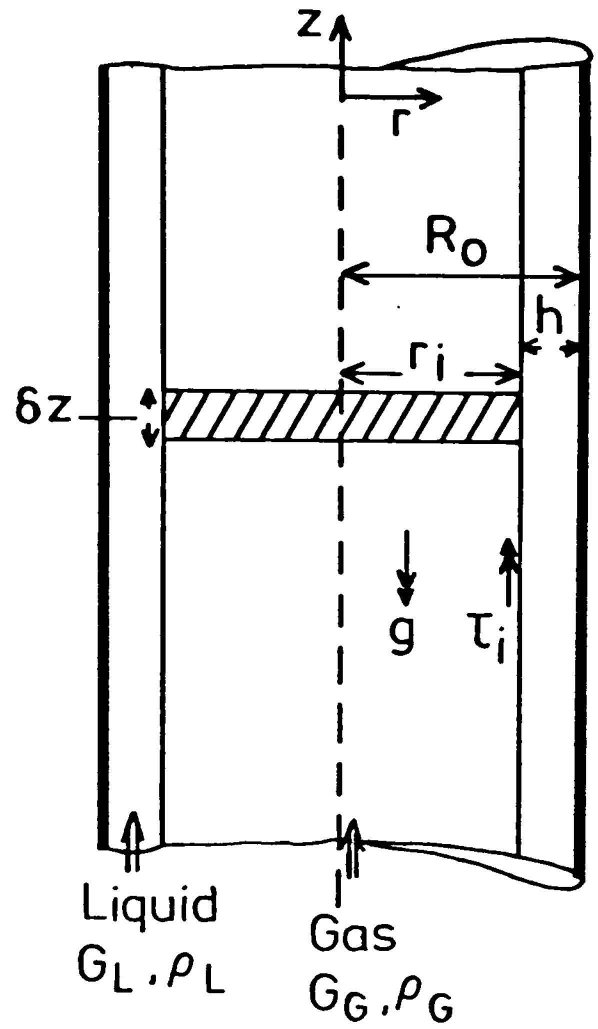

FIG. 2.1 NOTATION FOR VERTICAL UPWARD ANNULAR FLOW.

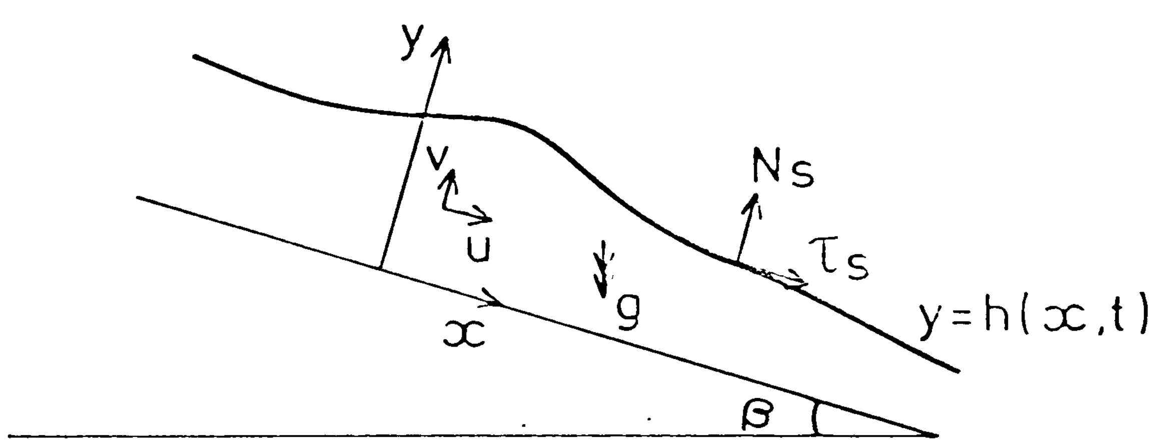

FIG. 2.2 NOTATION FOR FILM FLOW DOWN AN INCLINED PLANE.

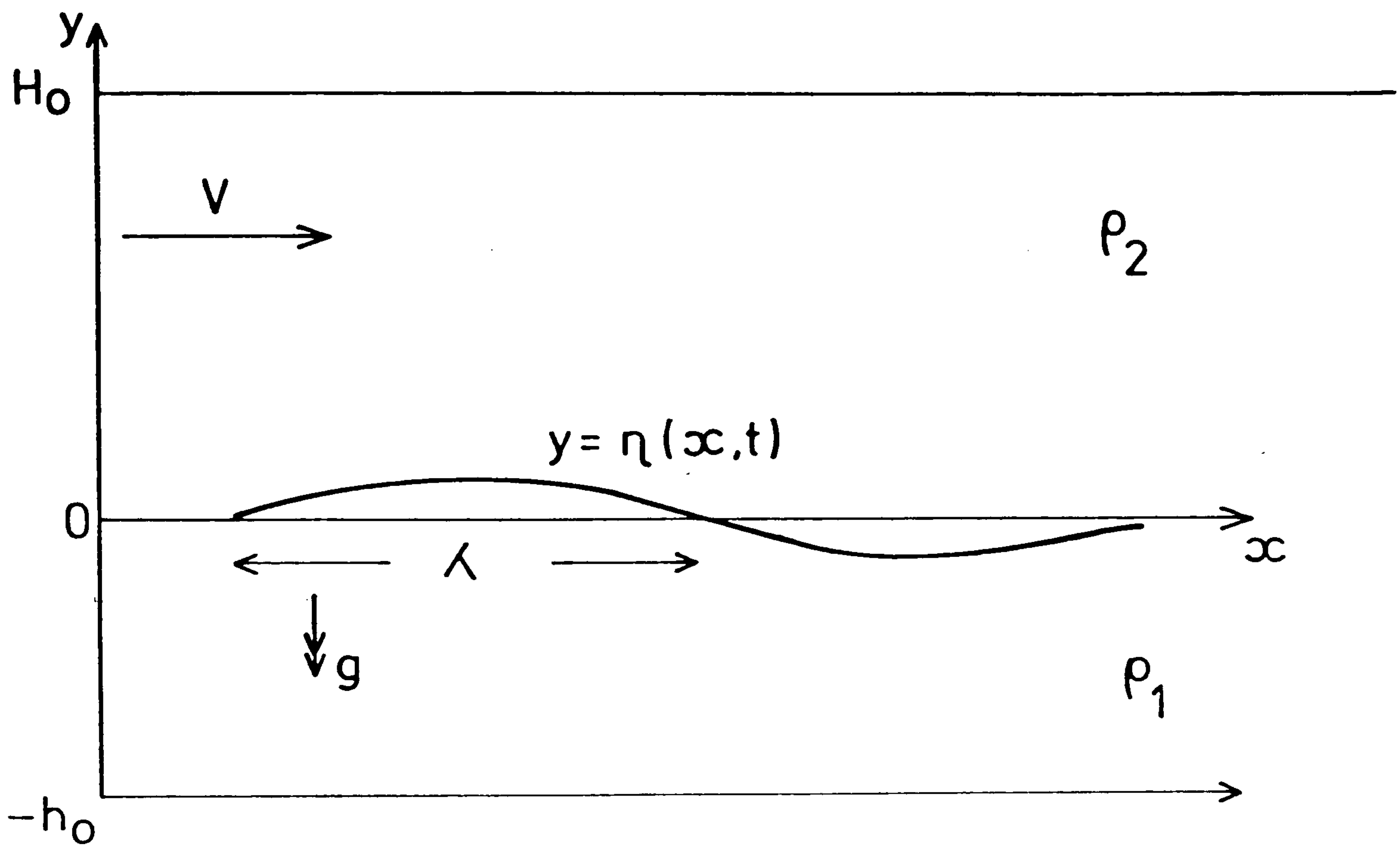

FIG. 2·3 NOTATION FOR HORIZONTAL STRATIFIED FLOW.

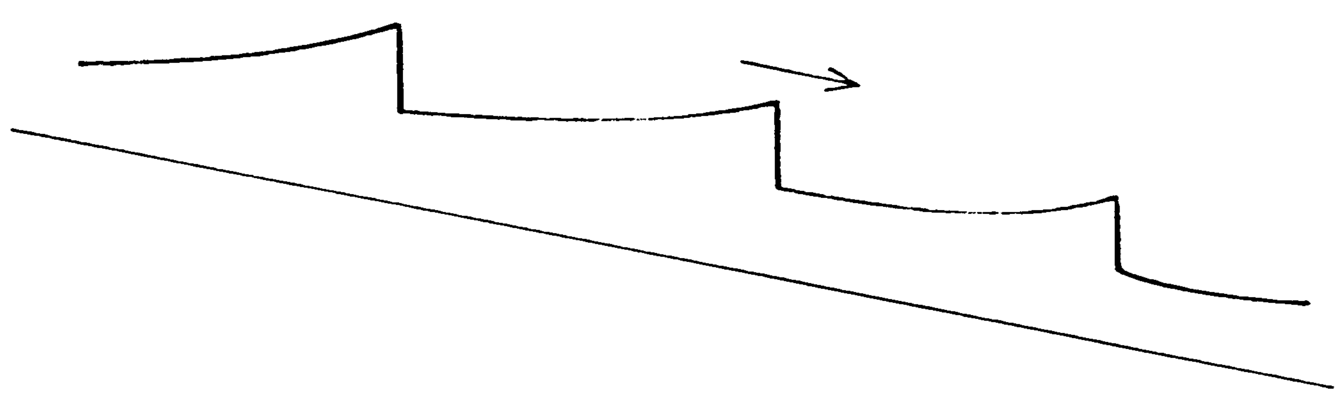

FIG. 2·4 DRESSLERS ROLL WAVE SOLUTION .

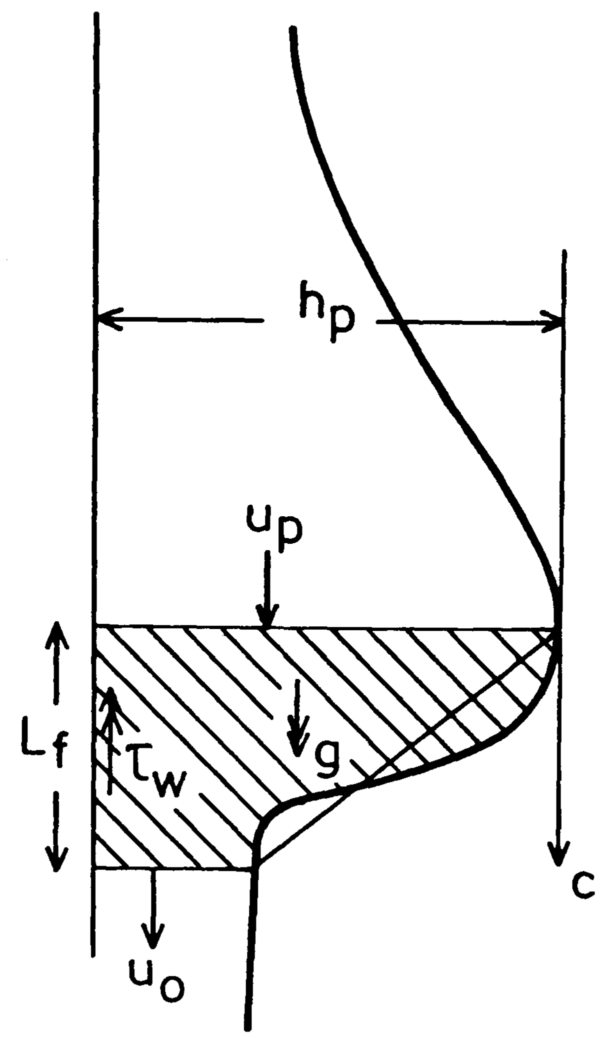

FIG. 2·5 MOMENTUM BALANCE ON FRONT SECTION OF LARGE WAVE IN VERTICAL DOWNFLOW.

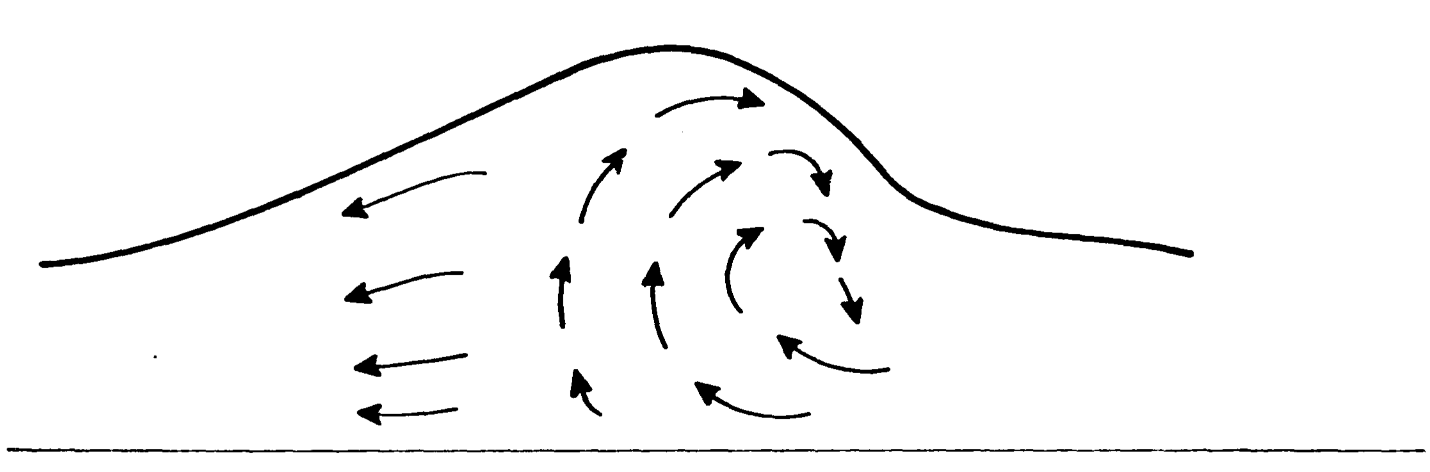

FIG. 2·6 DUKLERS PROPOSED FLOW PATTERN UNDER A WAVE.

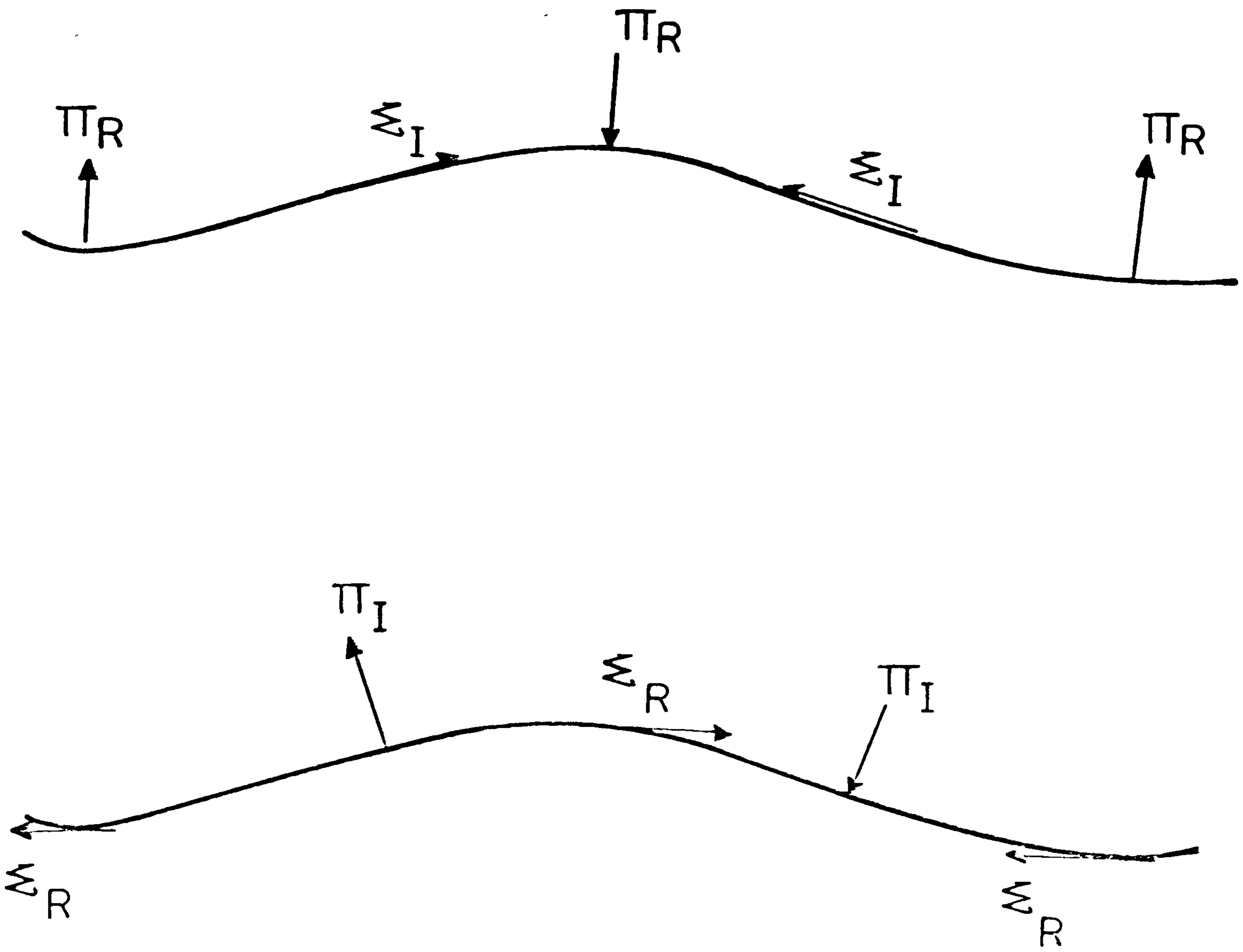

FIG. 3.1 PERTURBATION SURFACE STRESSES.

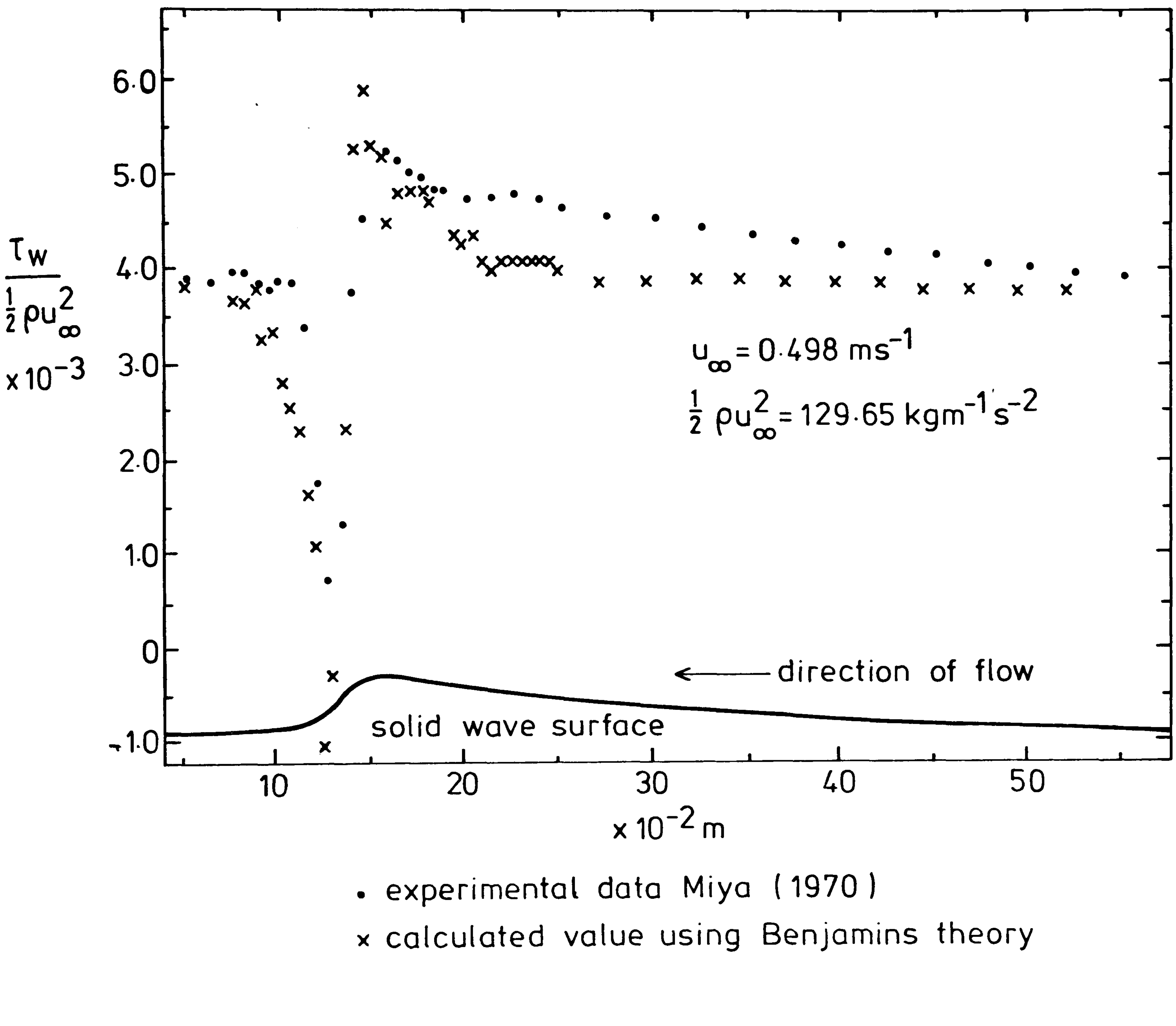

FIG. 3.2 SHEAR STRESS DISTRIBUTION OVER SOLID WAVE FOR Re = 22,700

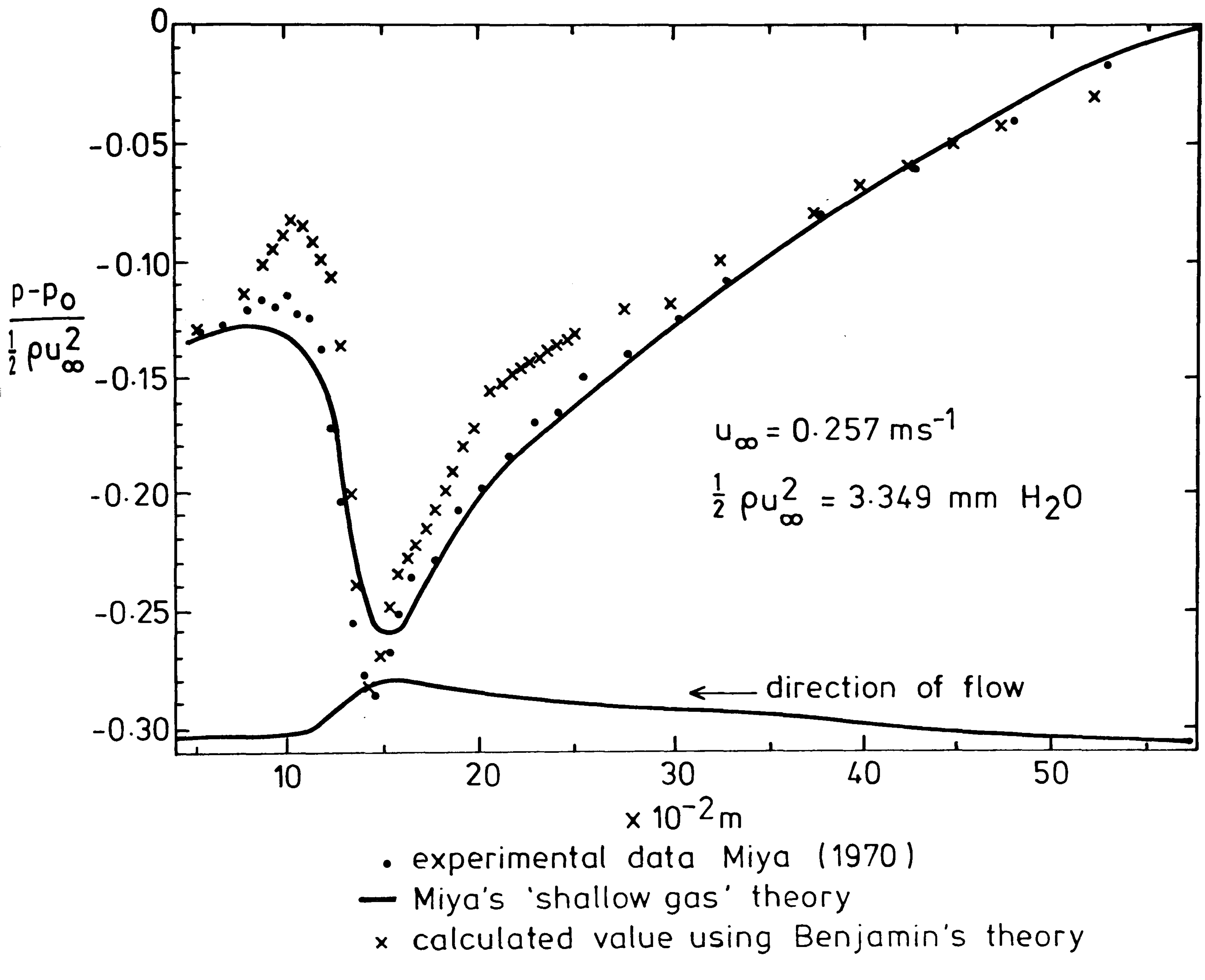

FIG. 3·3 PRESSURE DISTRIBUTION OVER SOLID WAVE FOR Re = 14,240

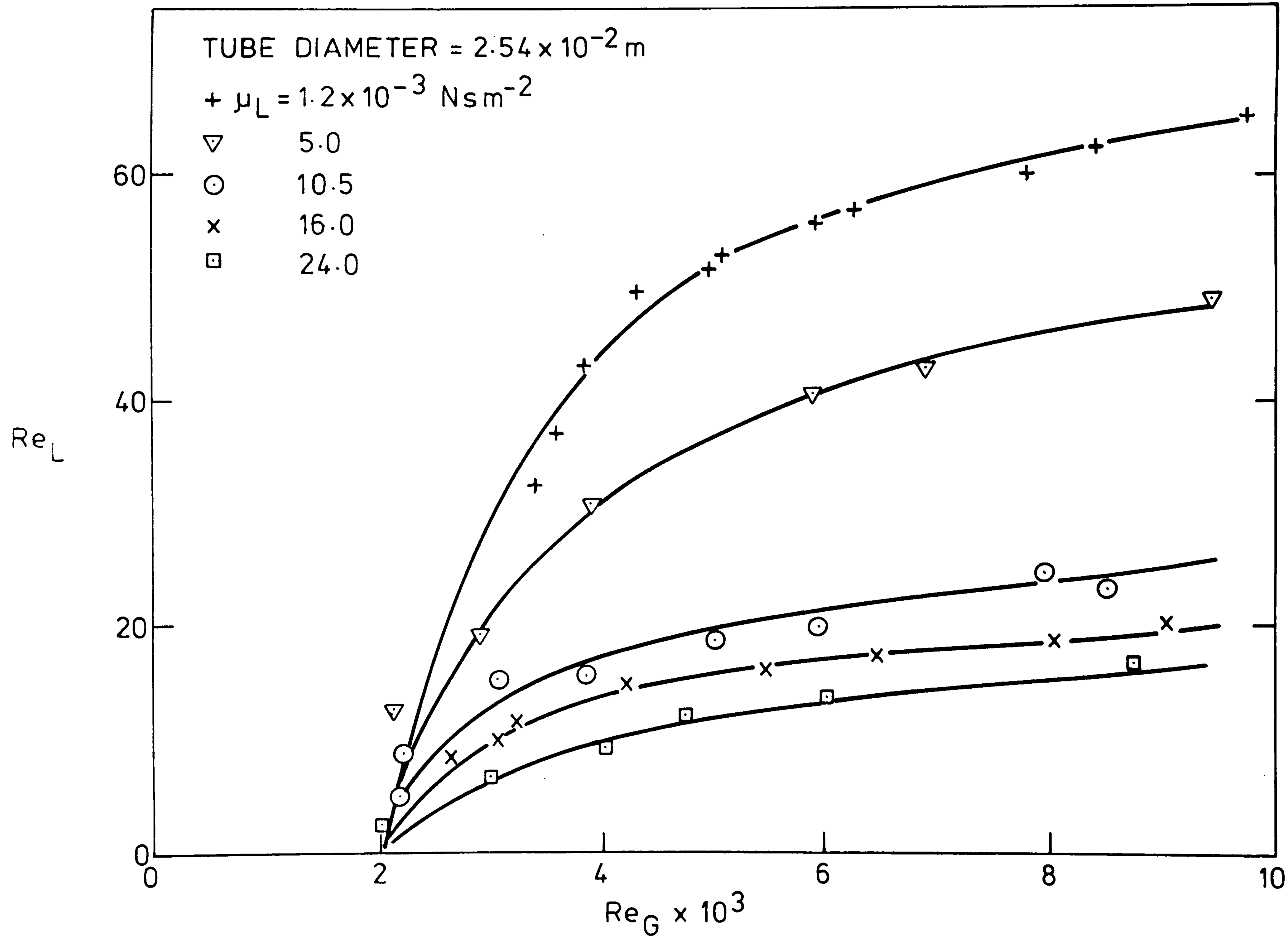

FIG. 4·1 EFFECT OF VISCOSITY ON WAVE INCEPTION -RESULTS OF HALL-TAYLOR (1966)

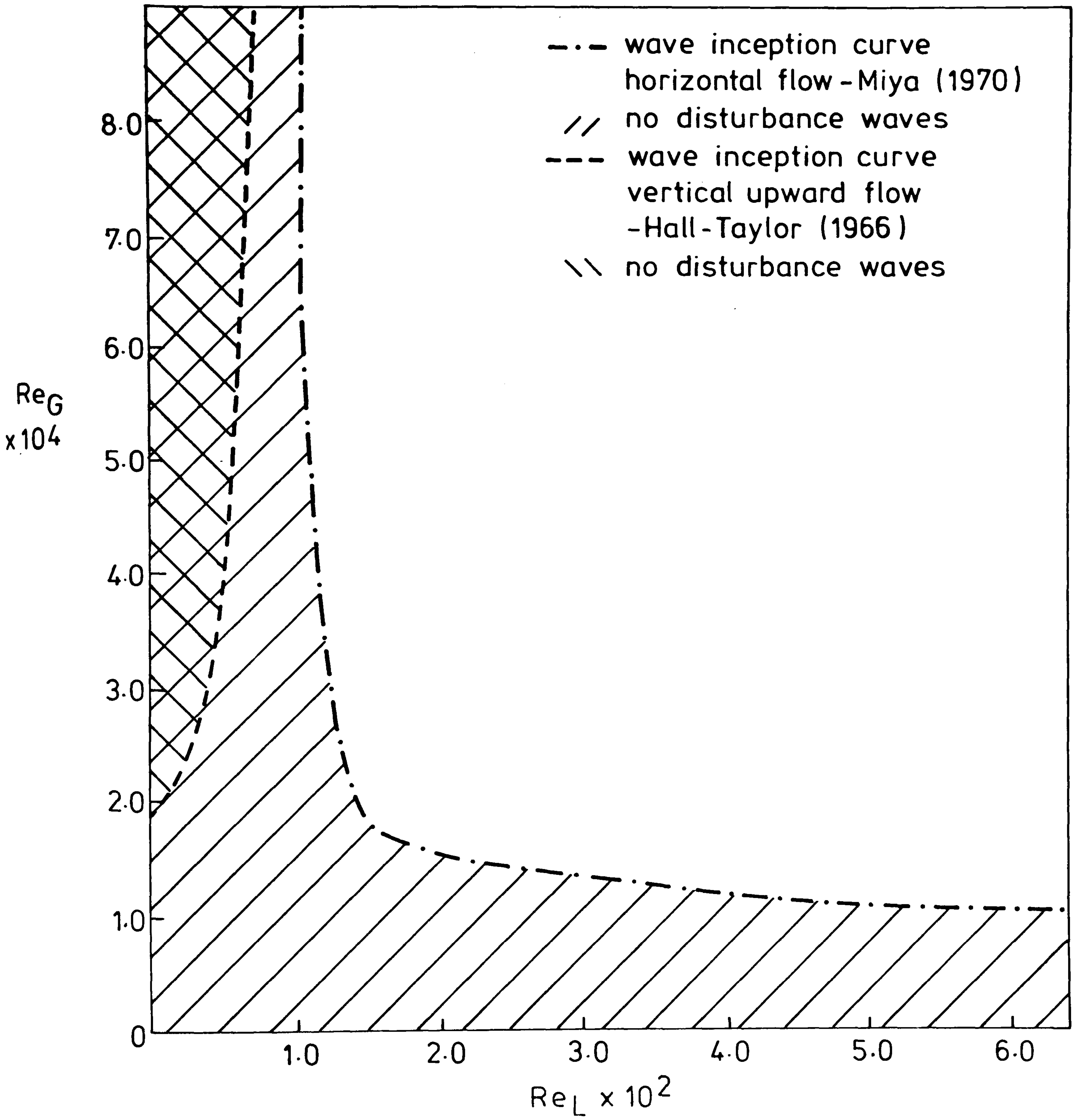

FIG. 4.2 EXPERIMENTAL WAVE INCEPTION CURVES FOR VERTICAL UPWARD AND HORIZONTAL FLOW.

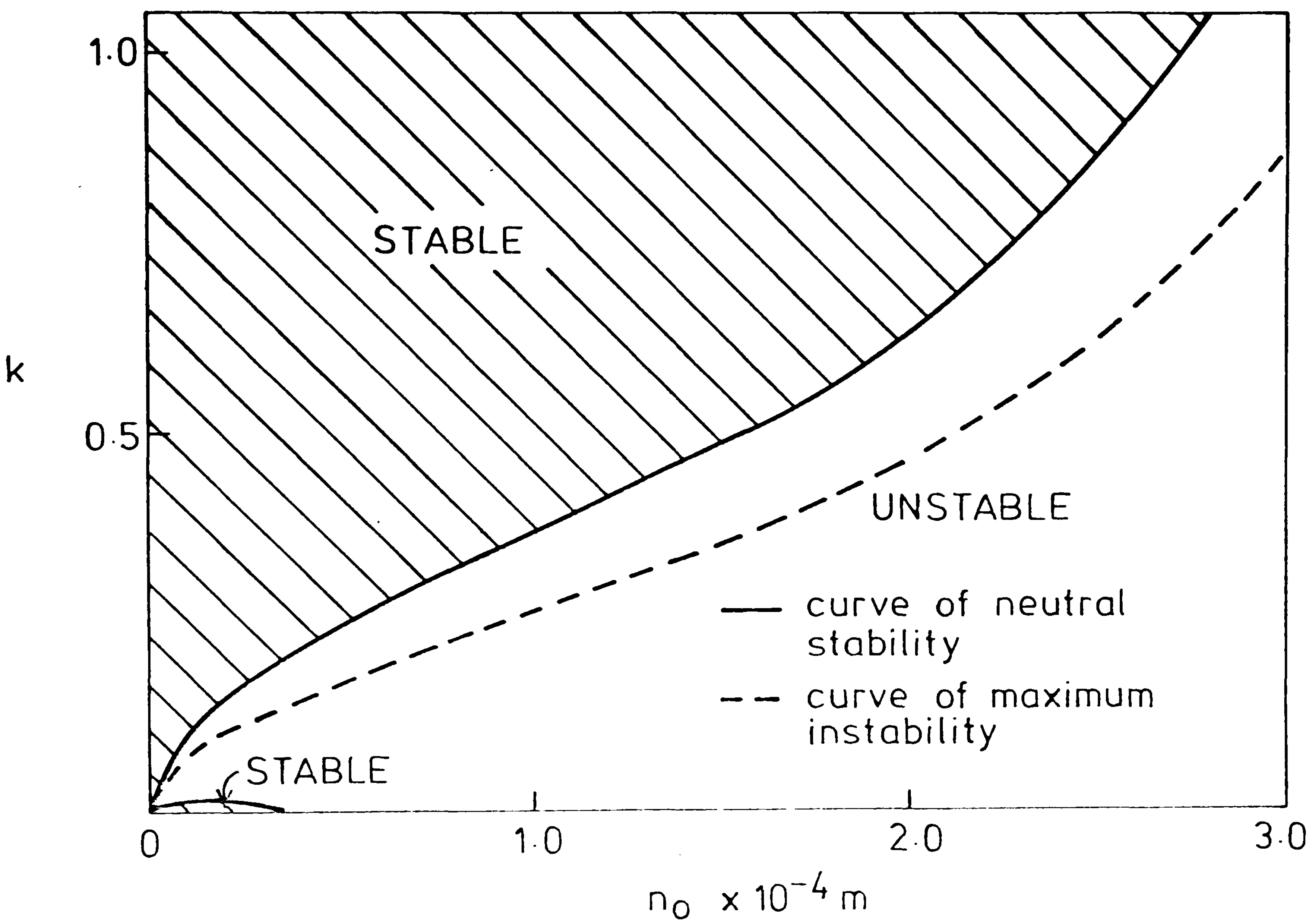

FIG. 4.3 STABILITY CURVES FOR VERTICAL UPWARD ANNULAR FLOW. $G_G = 31.7\ kgm^{-2}\ s^{-1}$

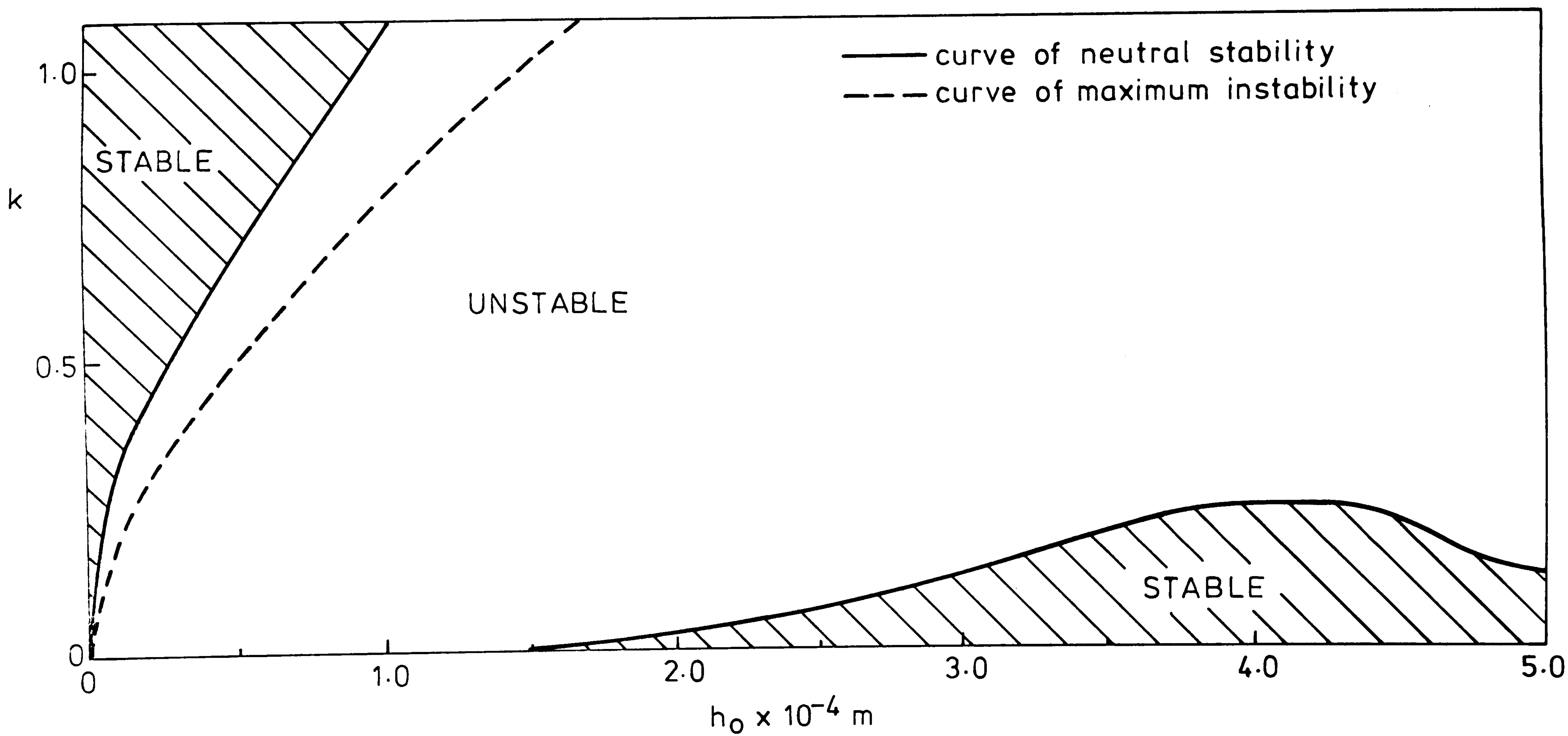

FIG. 4.4 STABILITY CURVES FOR VERTICAL UPWARD ANNULAR FLOW. $G_G = 63.4\ kgm^{-2}\ s^{-1}$.

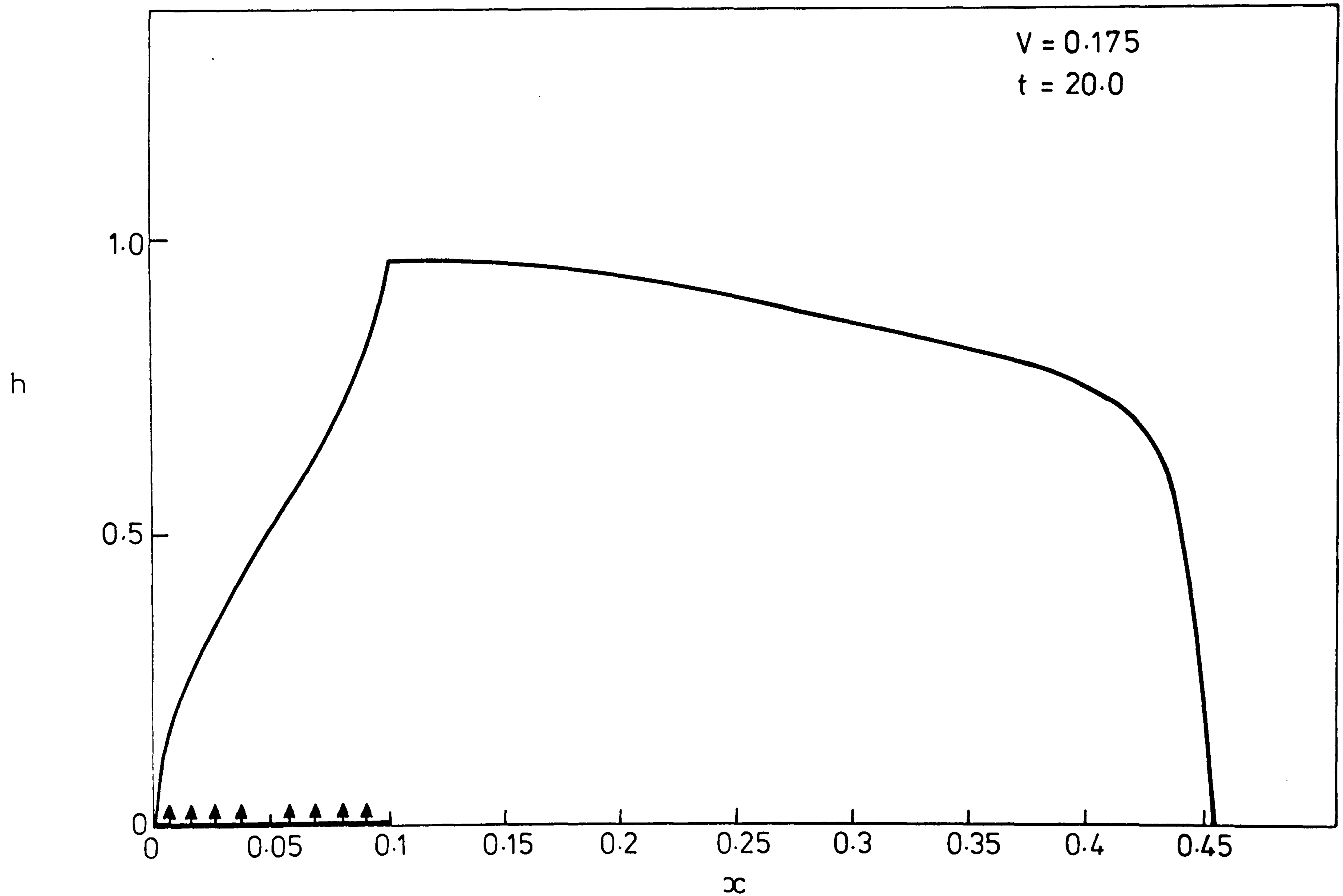

FIG. 4·5 NUMERICAL INJECTION MODEL $V < V_{MAX}$.

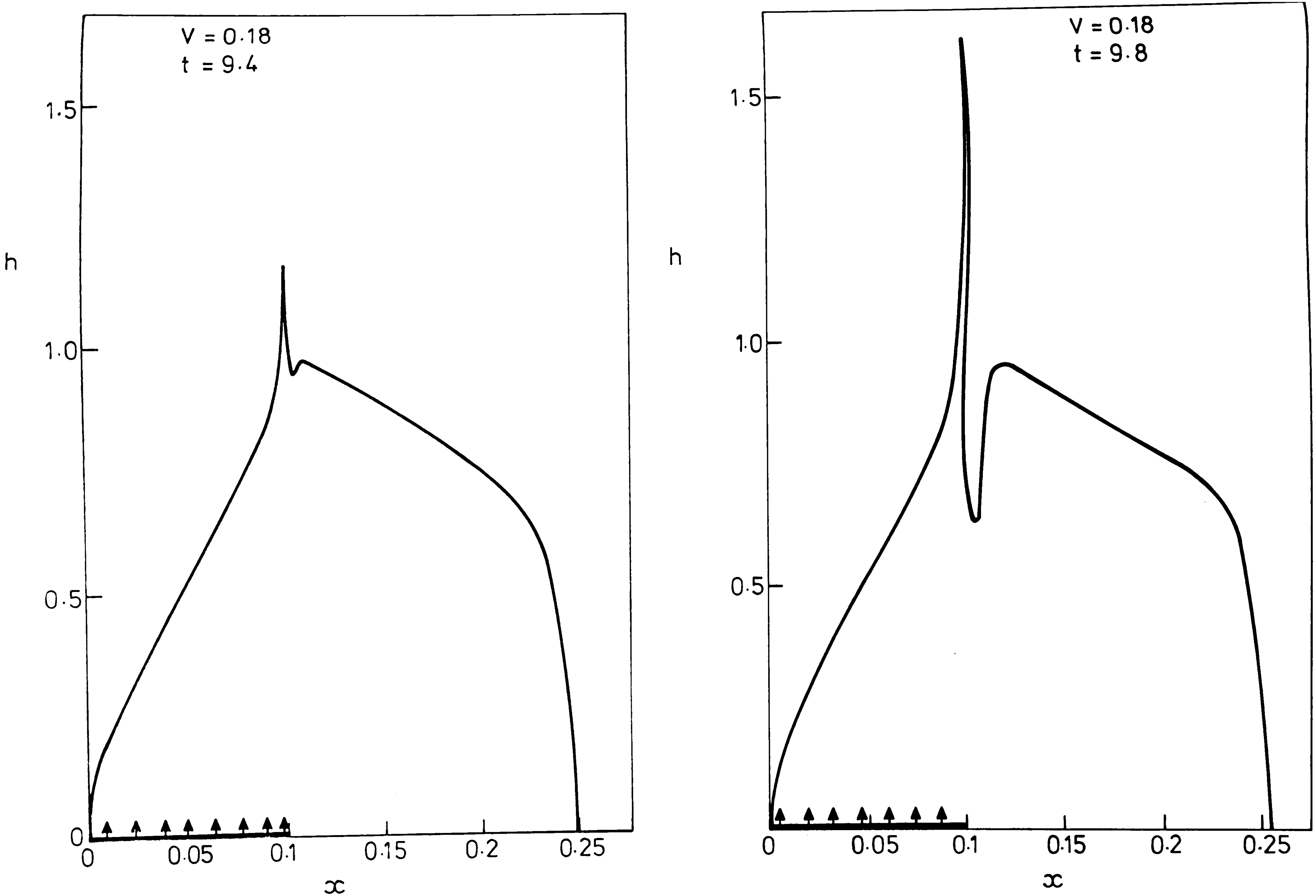

FIG. 4·6 NUMERICAL INJECTION MODEL $V > V_{MAX}$.

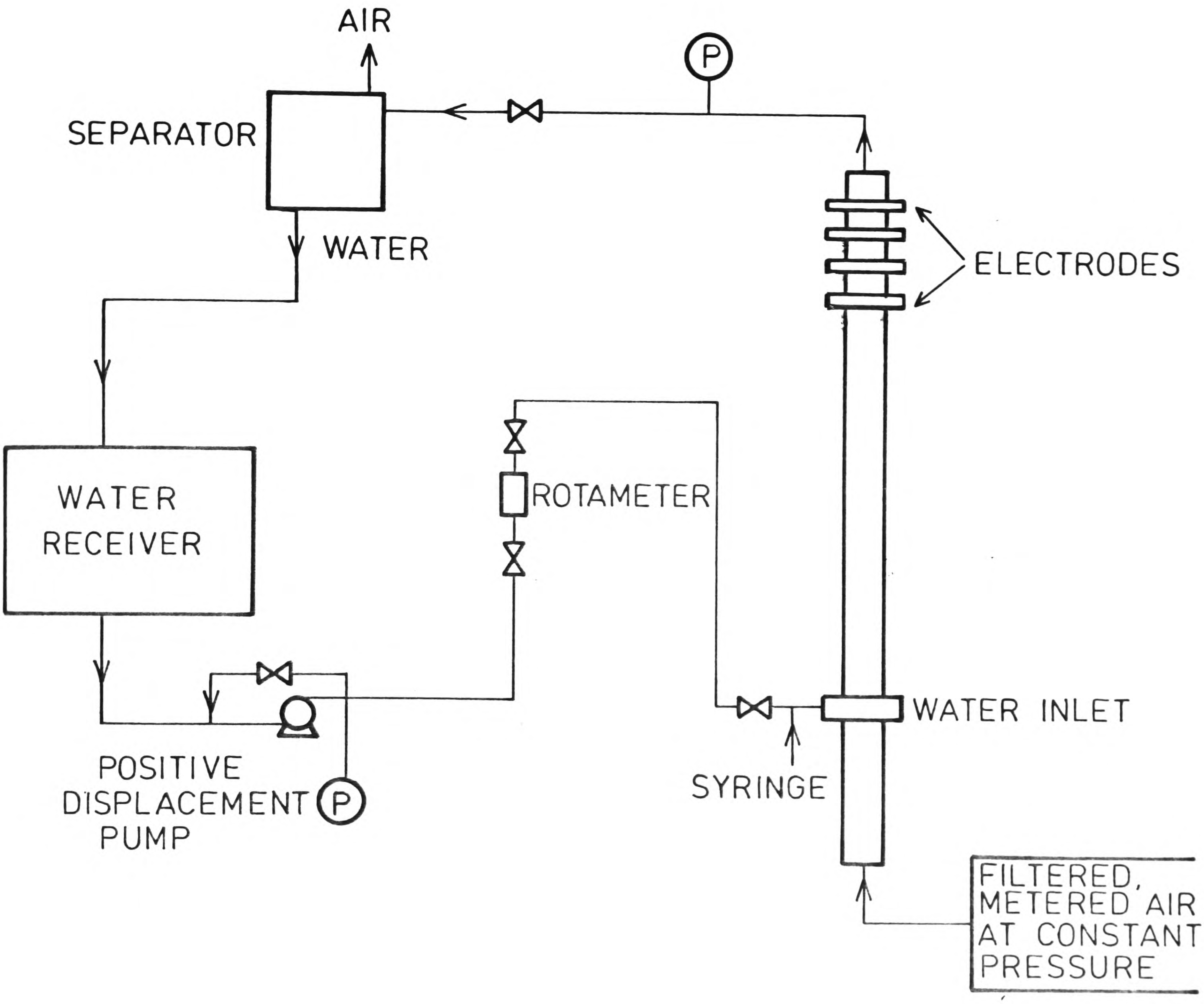

FIG. 5.1 APPARATUS.

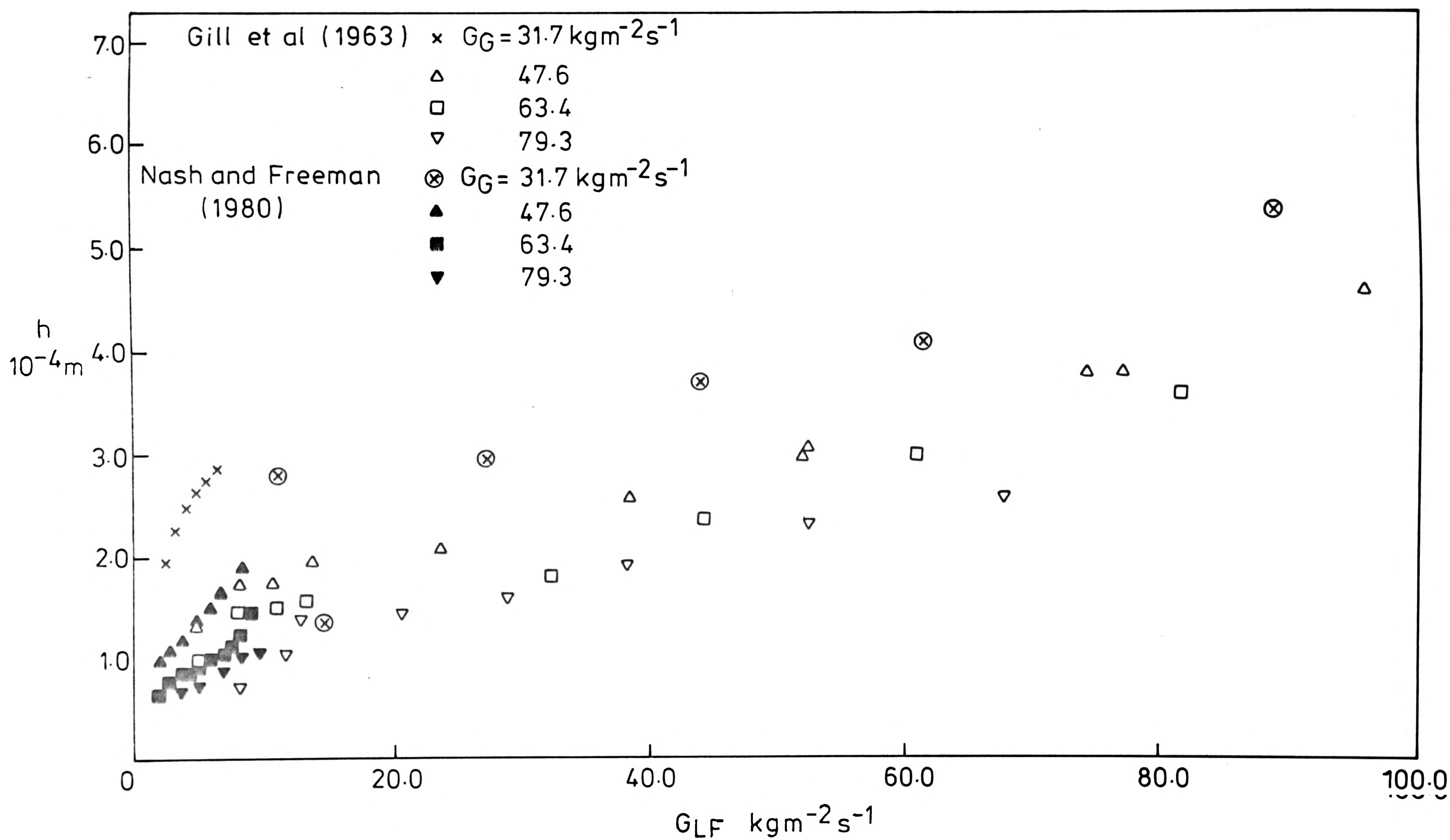

FIG. 5.2 EXPERIMENTAL AVERAGE FILM THICKNESS RESULTS .

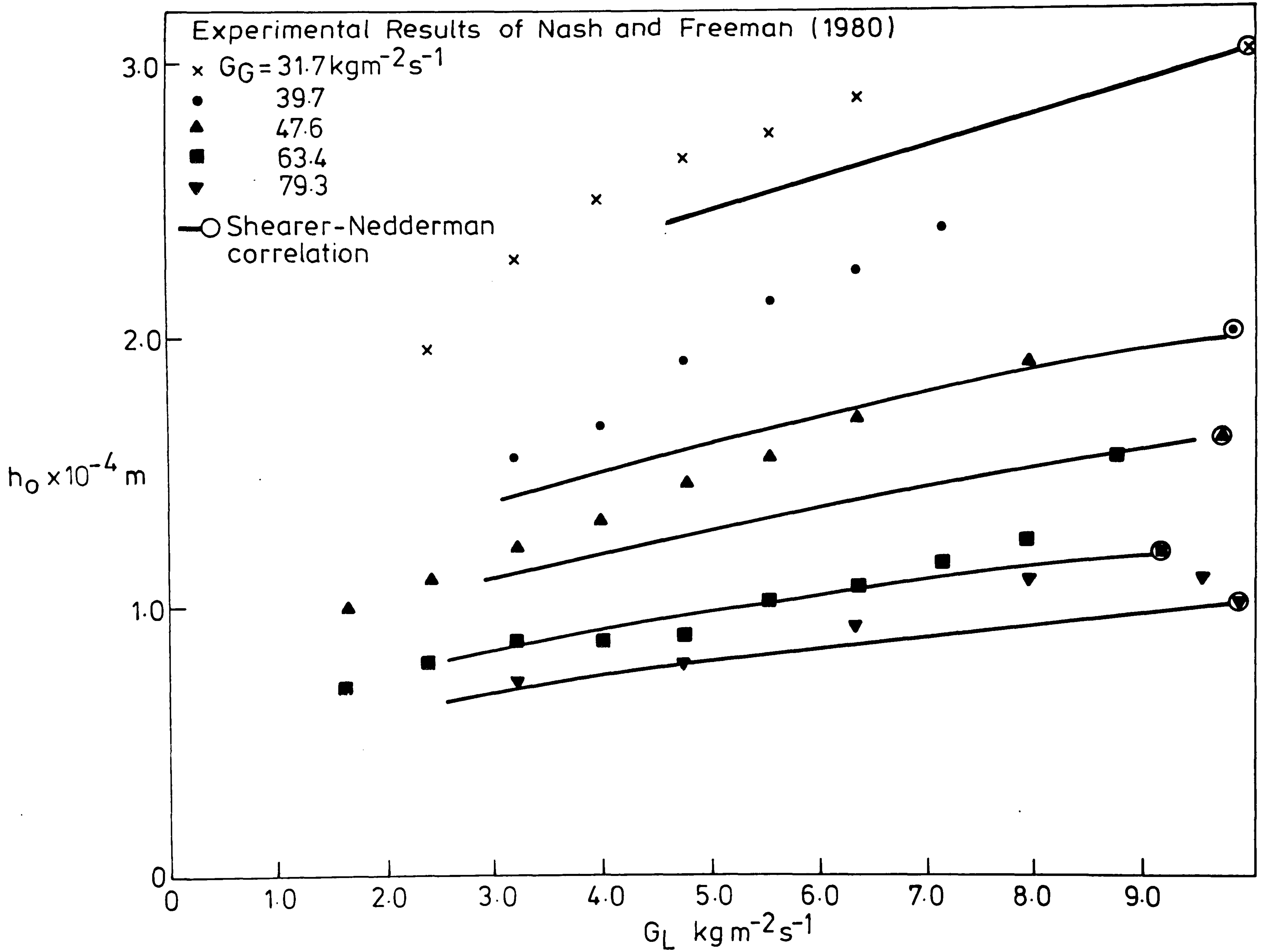

FIG. 5.3 COMPARISON BETWEEN EXPERIMENT AND SHEARER-NEDDERMAN CORRELATION.

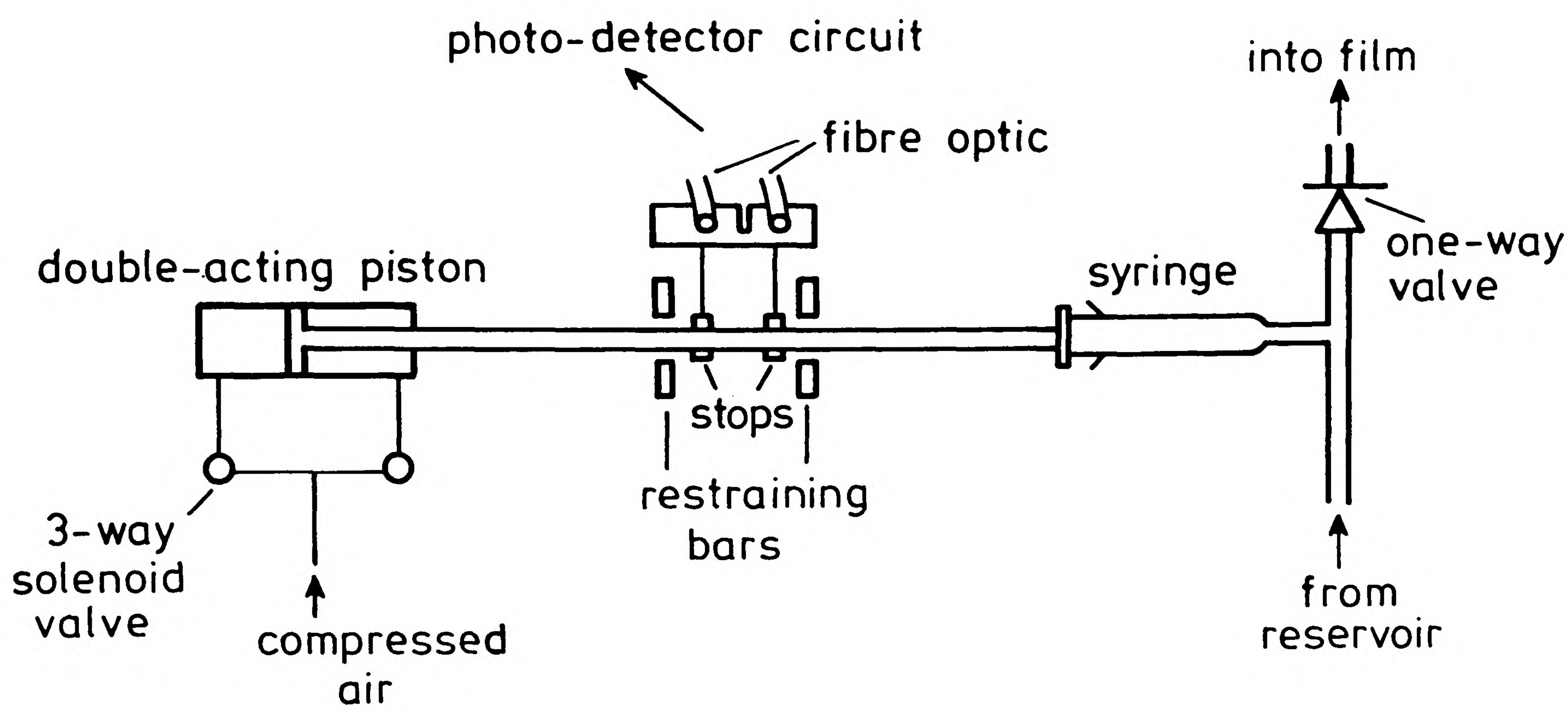

FIG. 5.4 INJECTION DEVICE.

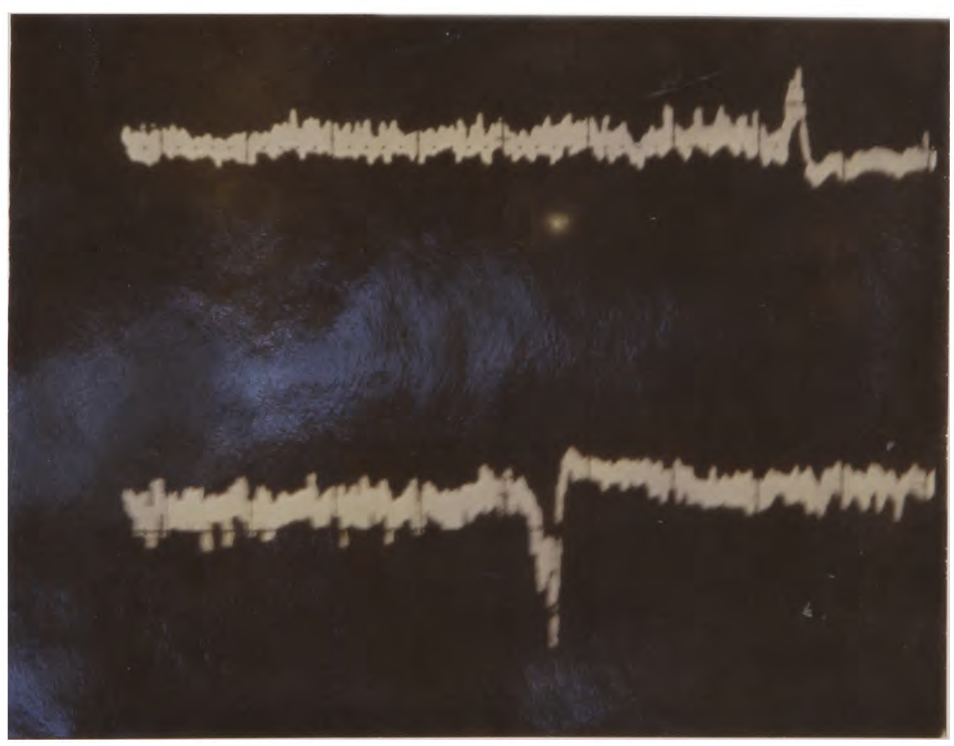

FIG. 5.5 OSCILLOSCOPE TRACE OF AN INJECTION PULSE.

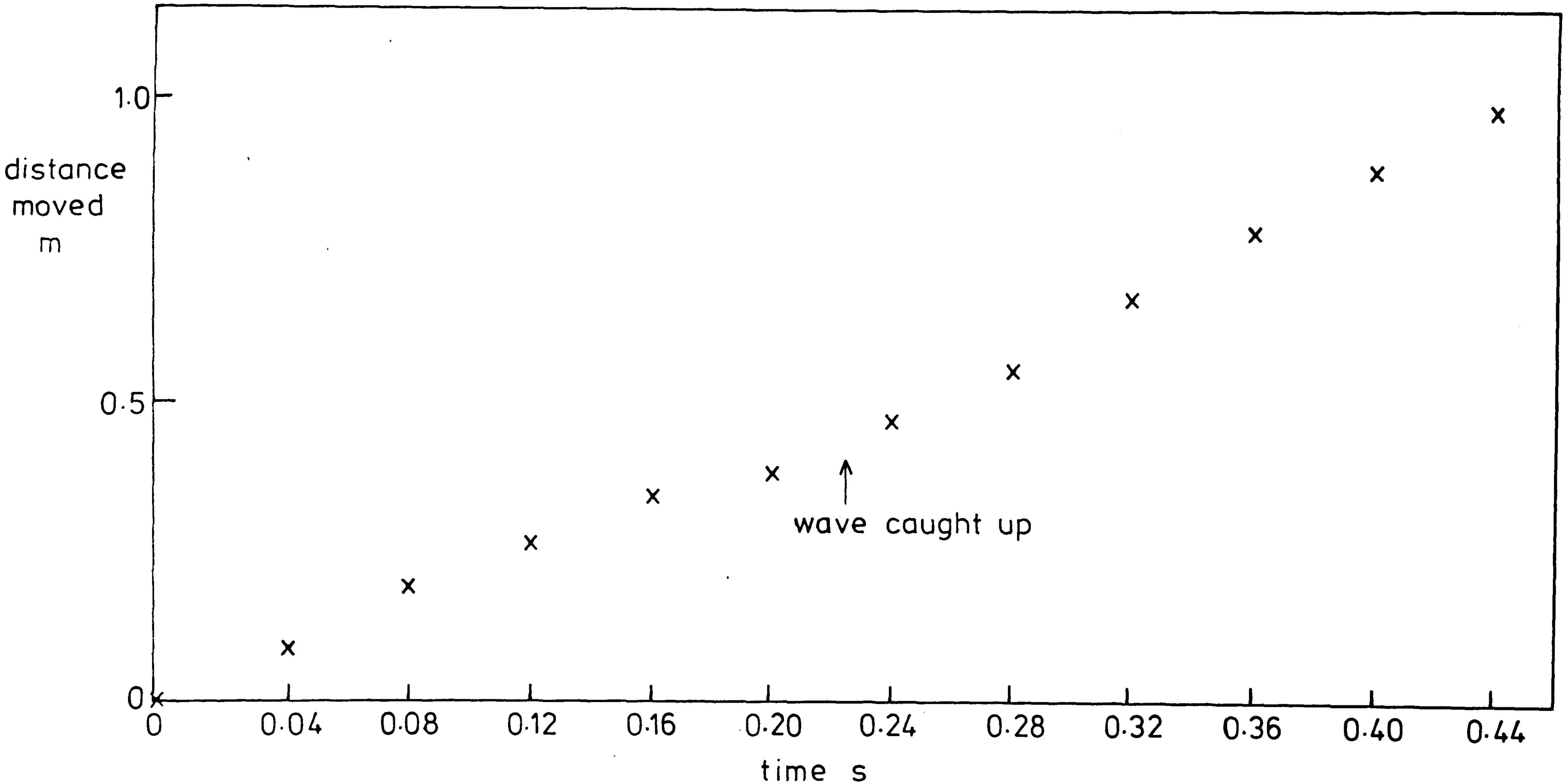

FIG. 5.6 PROGRESS OF AN INJECTED WAVE FROM SINGLE-FRAME OBSERVATIONS.

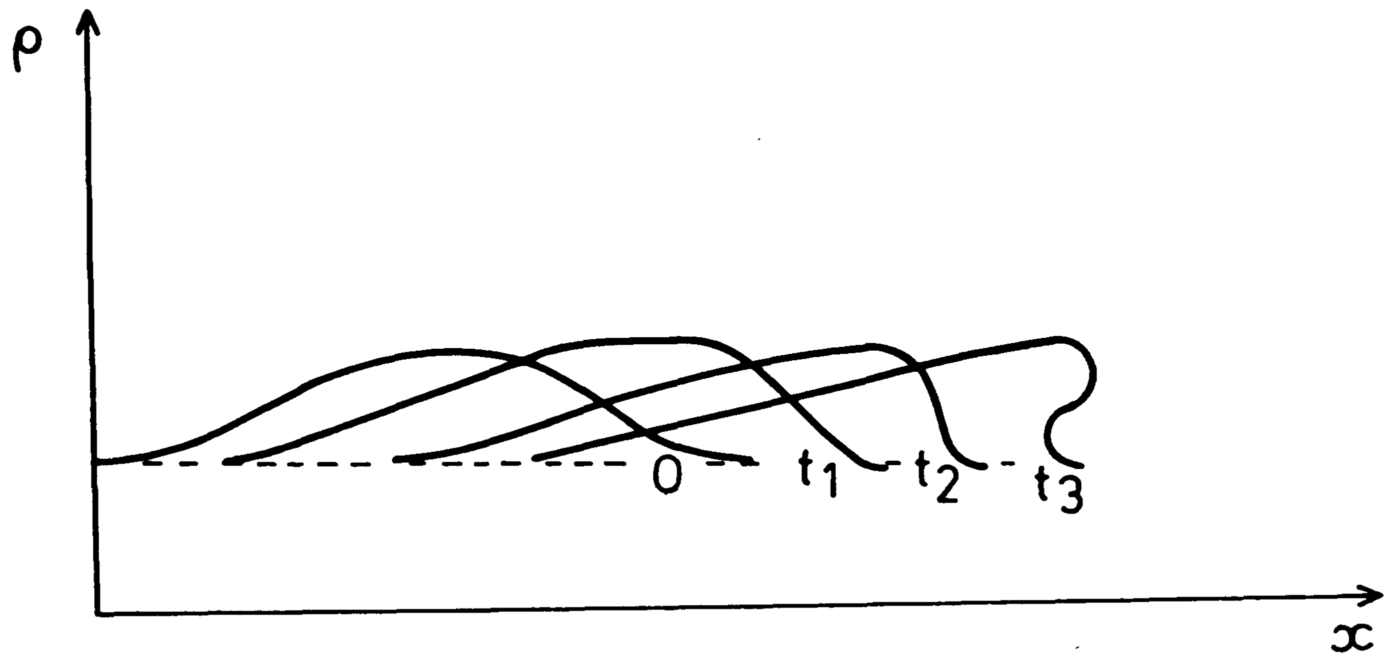

FIG. 6·1 A BREAKING WAVE: SUCCESSIVE PROFILES.

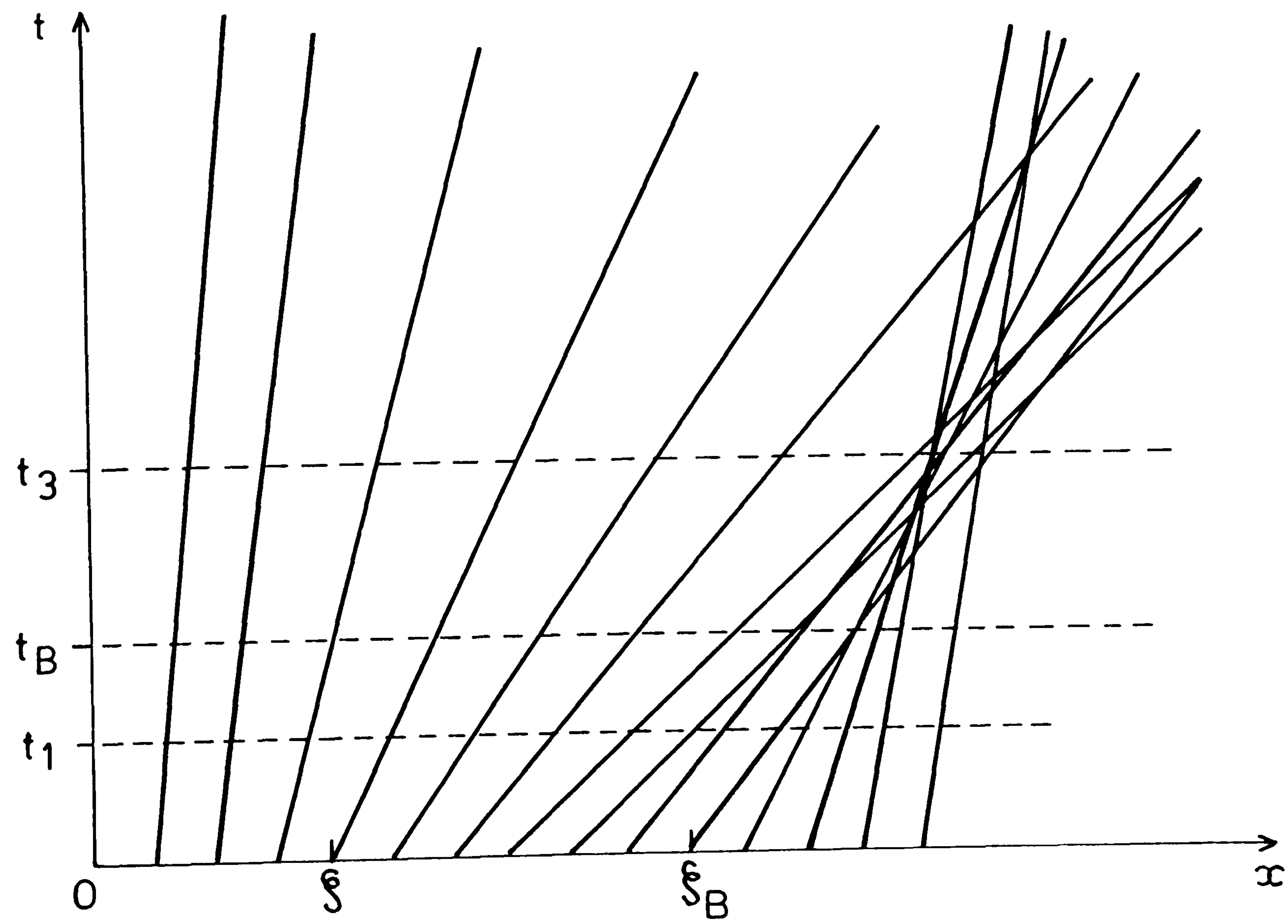

FIG. 6·2 CHARACTERISTIC DIAGRAM CORRESPONDING TO FIG.6·1

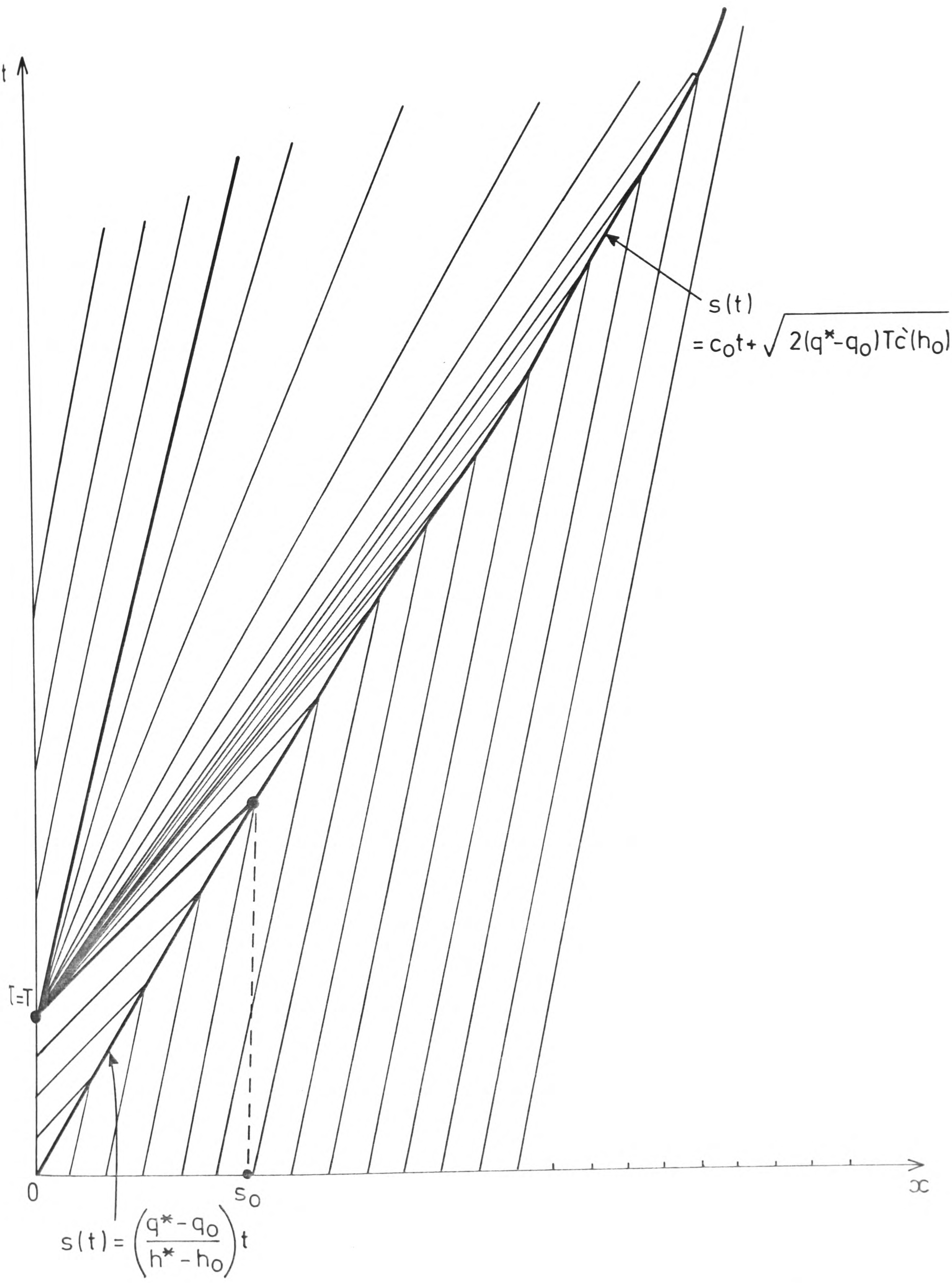

FIG. 6.3 CHARACTERISTIC DIAGRAM FOR INJECTED PULSE.

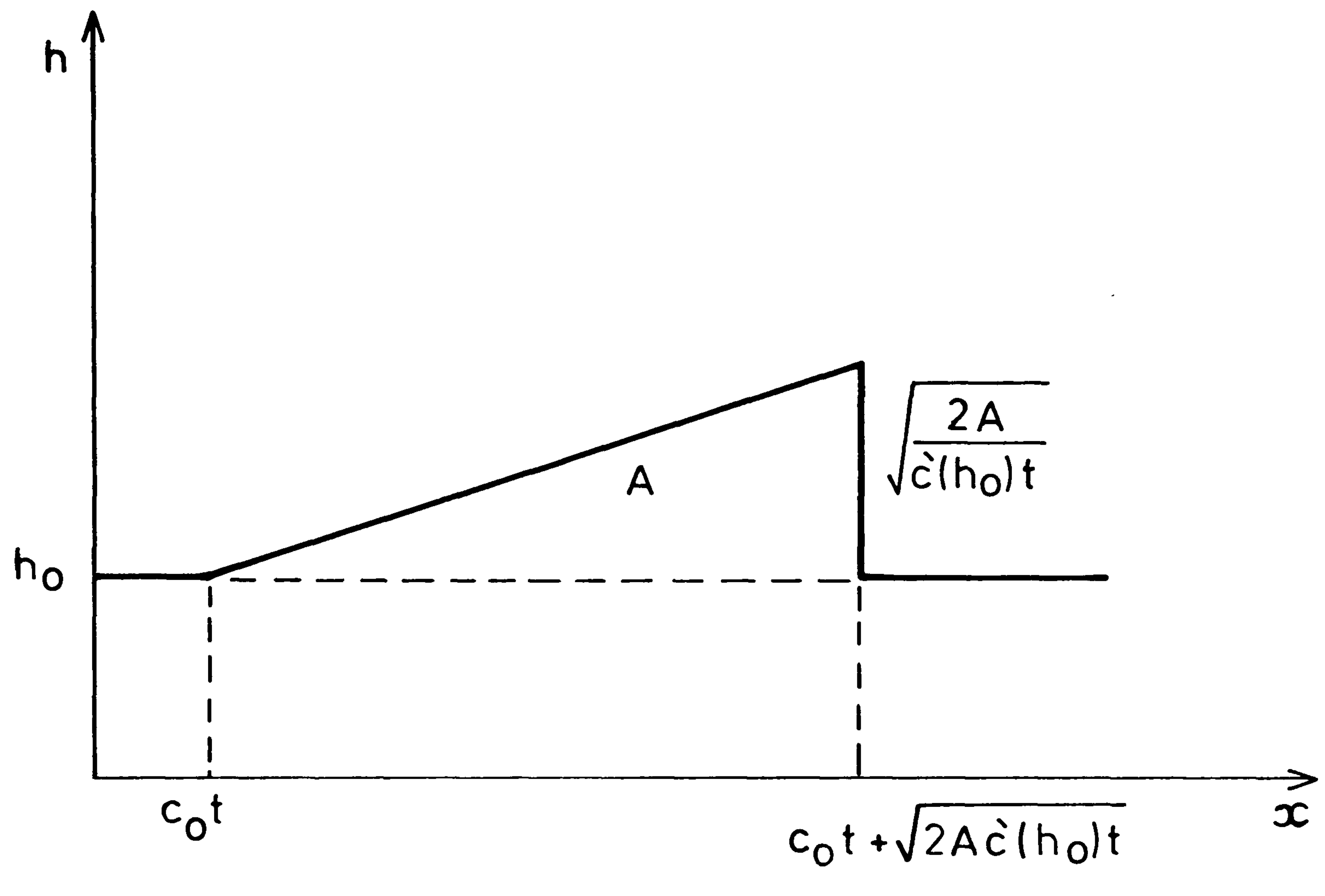

FIG. 6.4 THE ASYMPTOTIC TRIANGULAR WAVE.

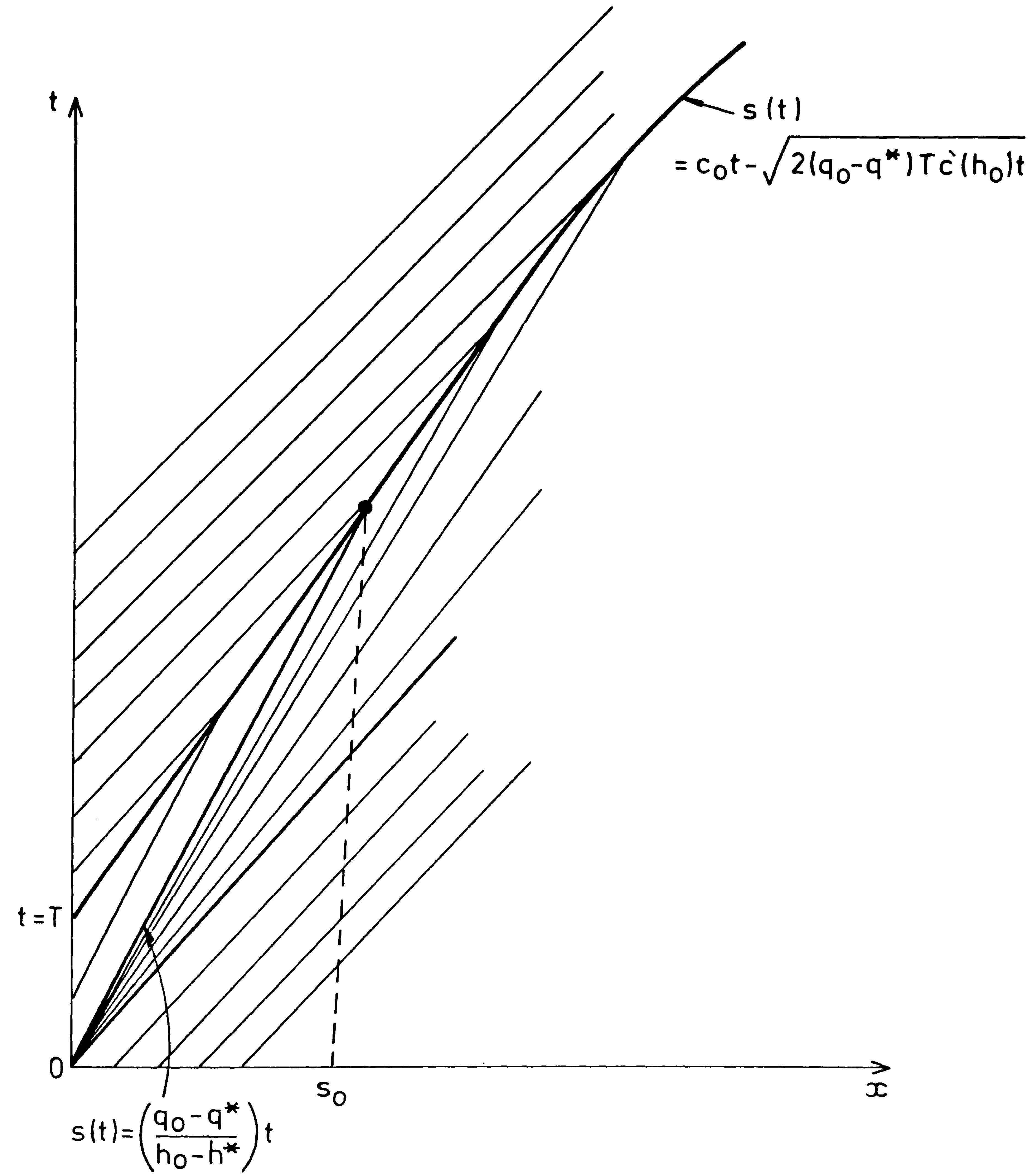

FIG. 6.5 CHARACTERISTIC DIAGRAM FOR 'SUCK' PULSE.

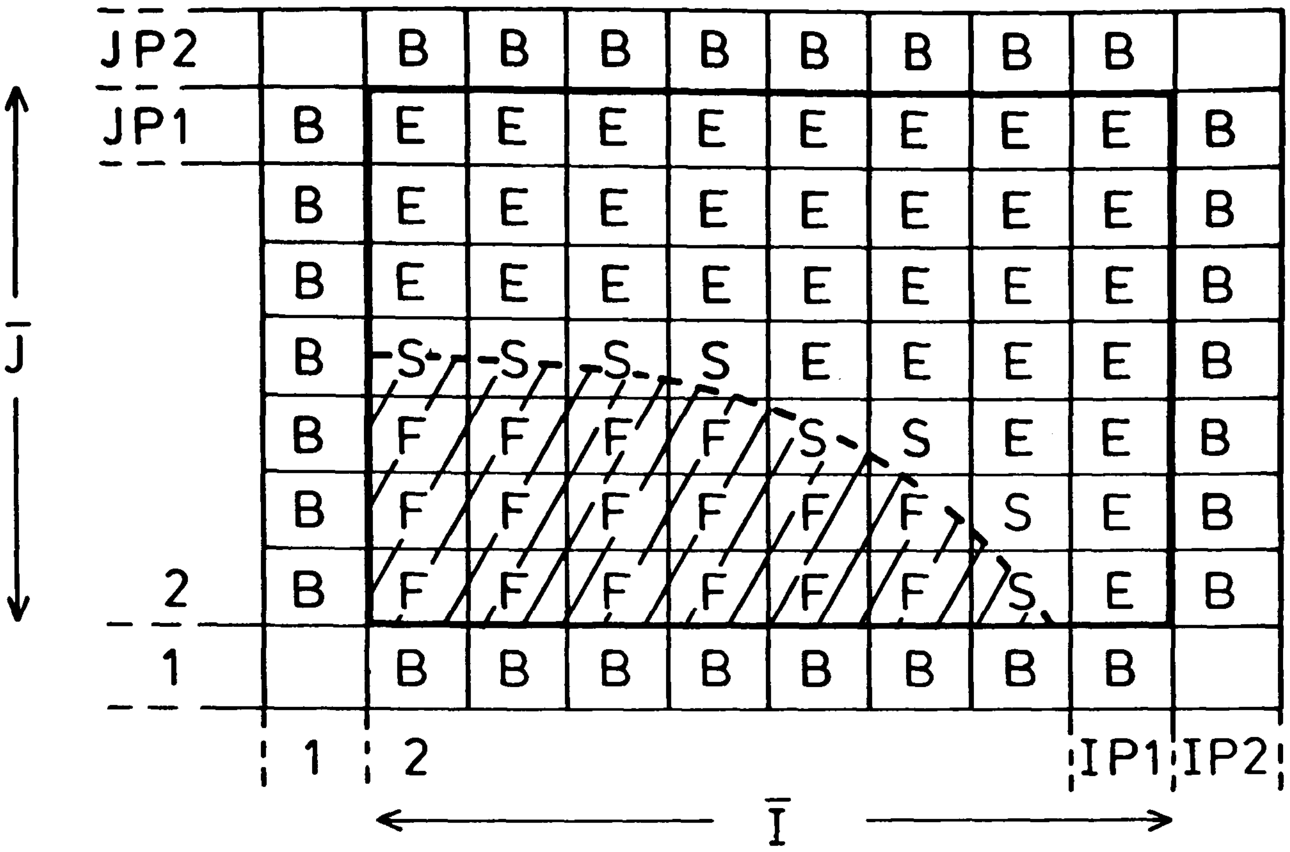

FIG. 7·1 ZUNI COMPUTING MESH.

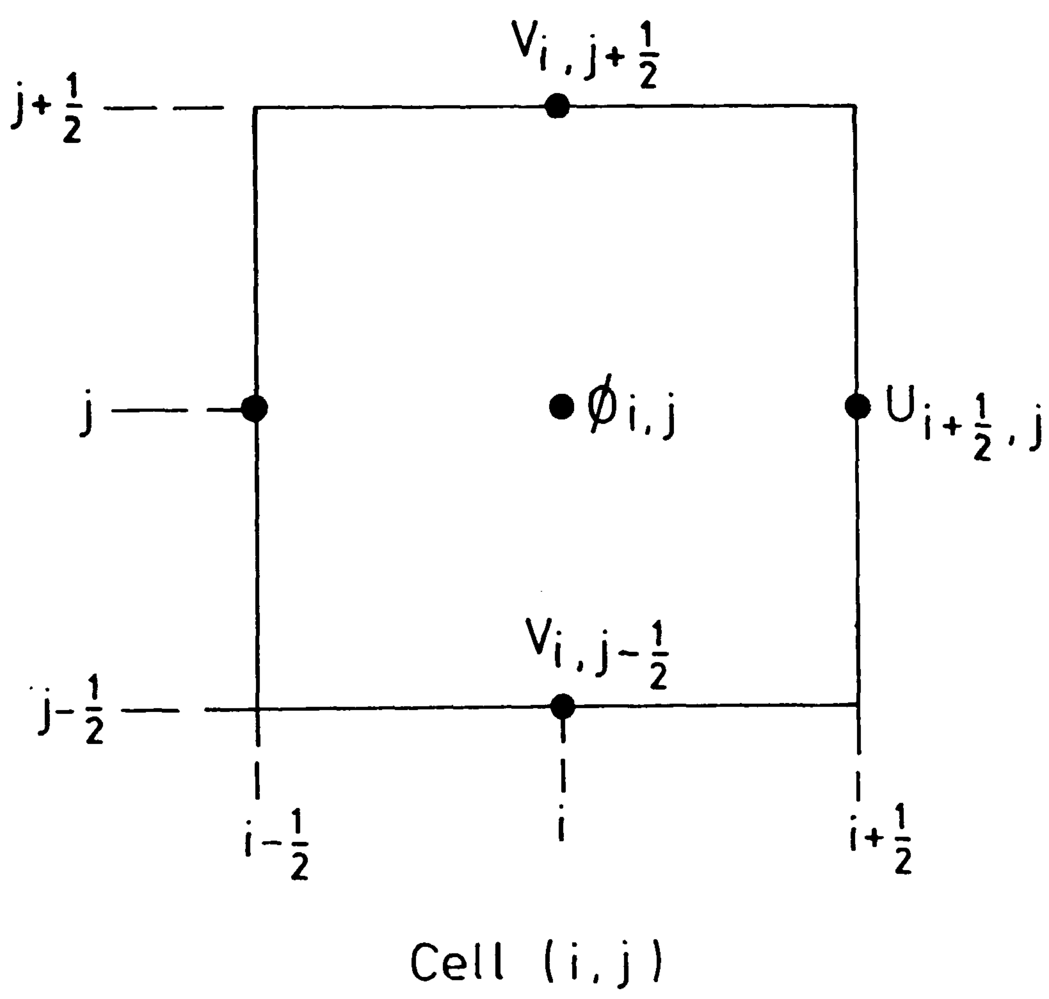

FIG. 7·2 THE LOCATION OF THE CELL VARIABLES IN A SMAC CELL.

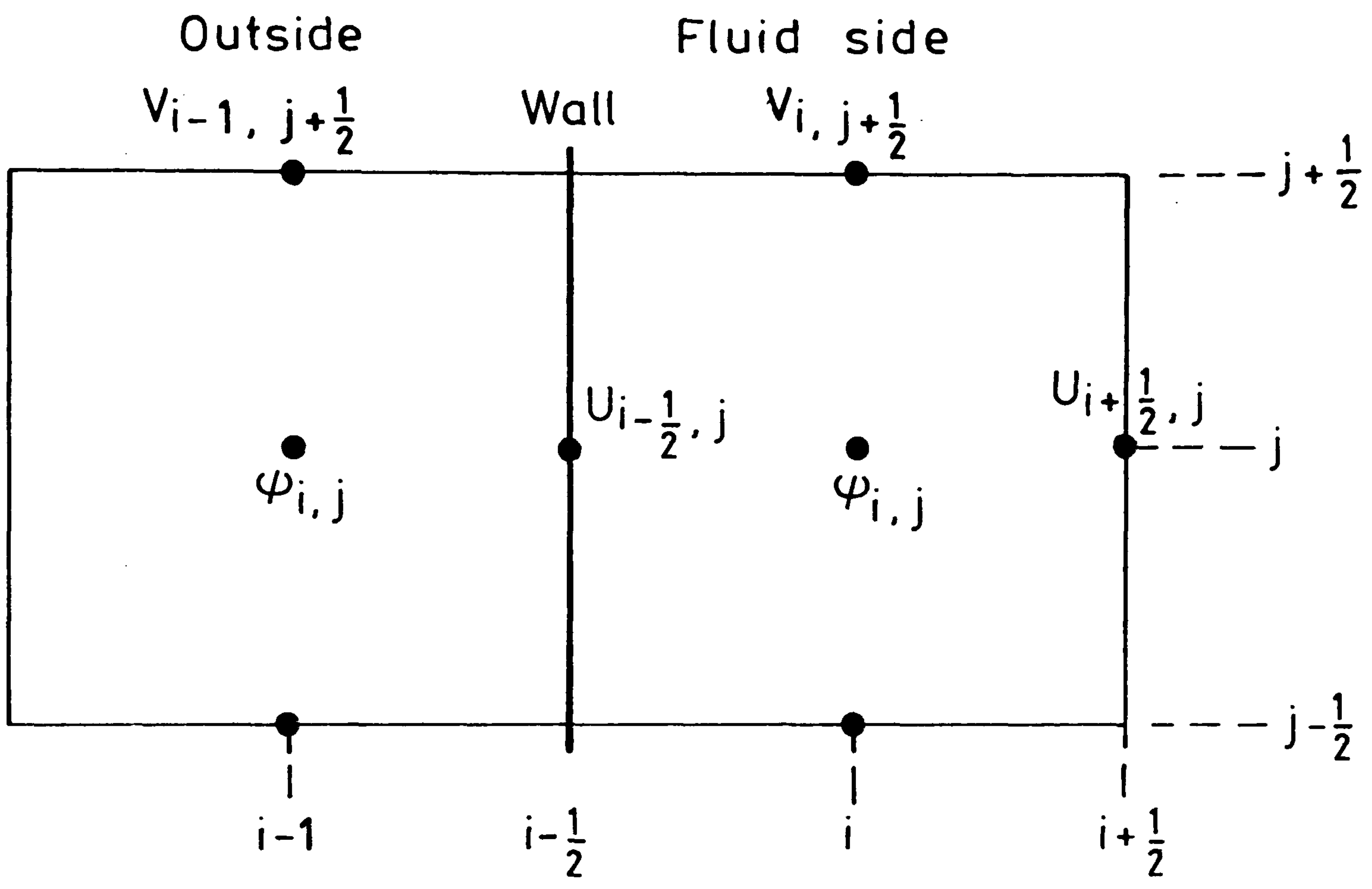

FIG. 7.3 VARIABLE POSITIONS AT A SMAC LEFT WALL.

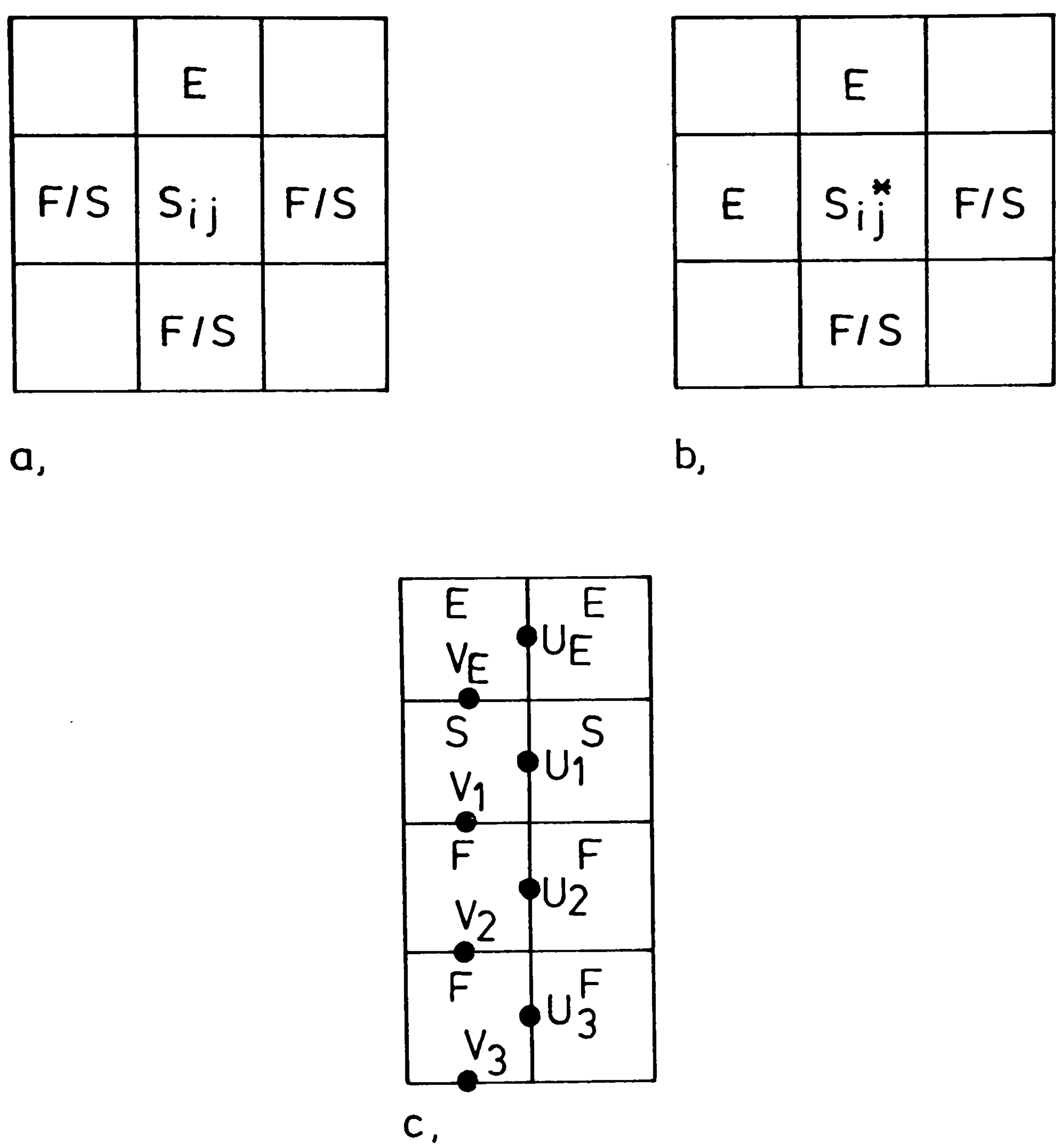

FIG. 7.4 a, b, c SURFACE/EMPTY CELL CONFIGURATIONS

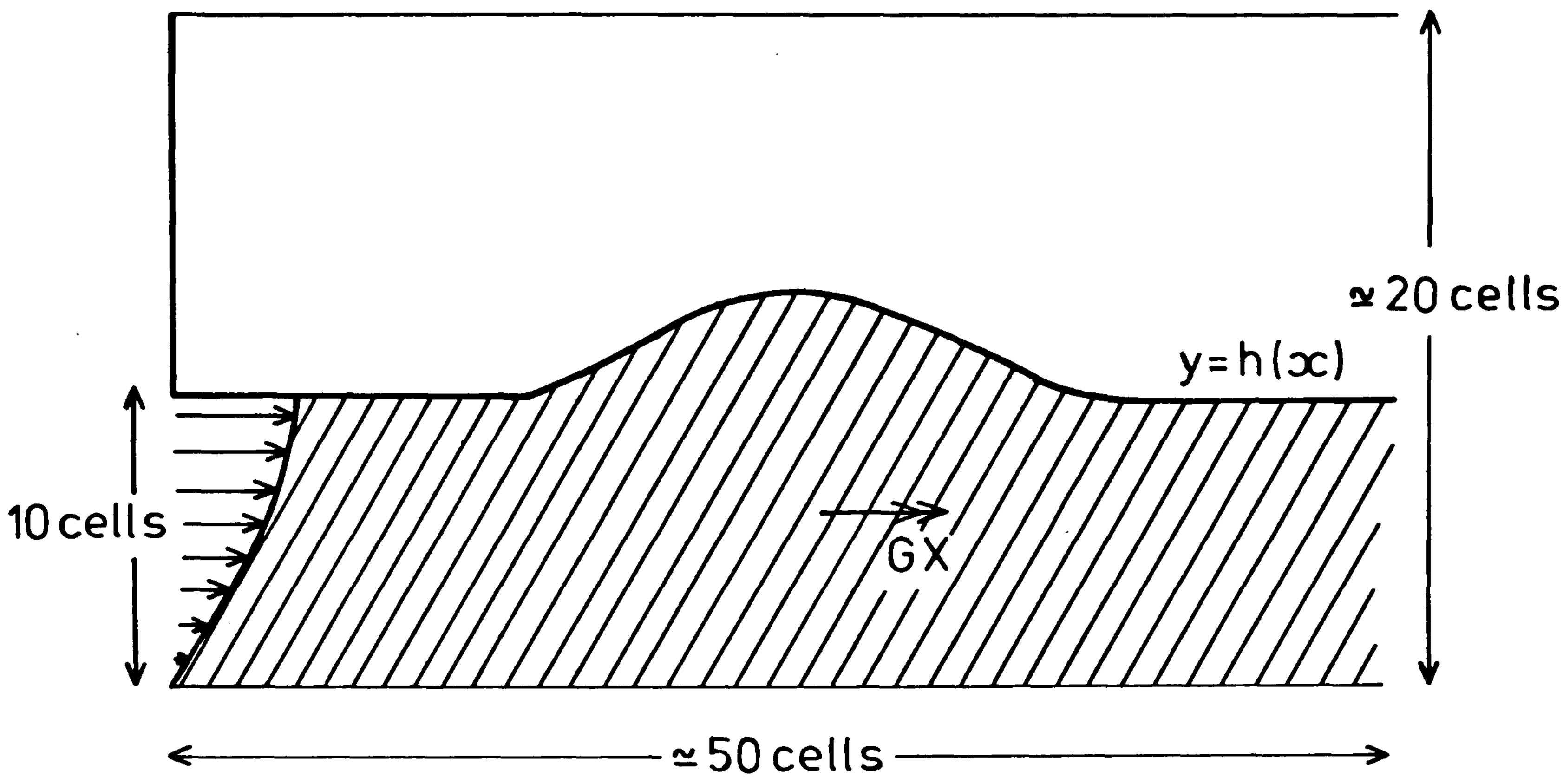

FIG. 7.5 SET-UP FOR SMAC WAVE RUN.

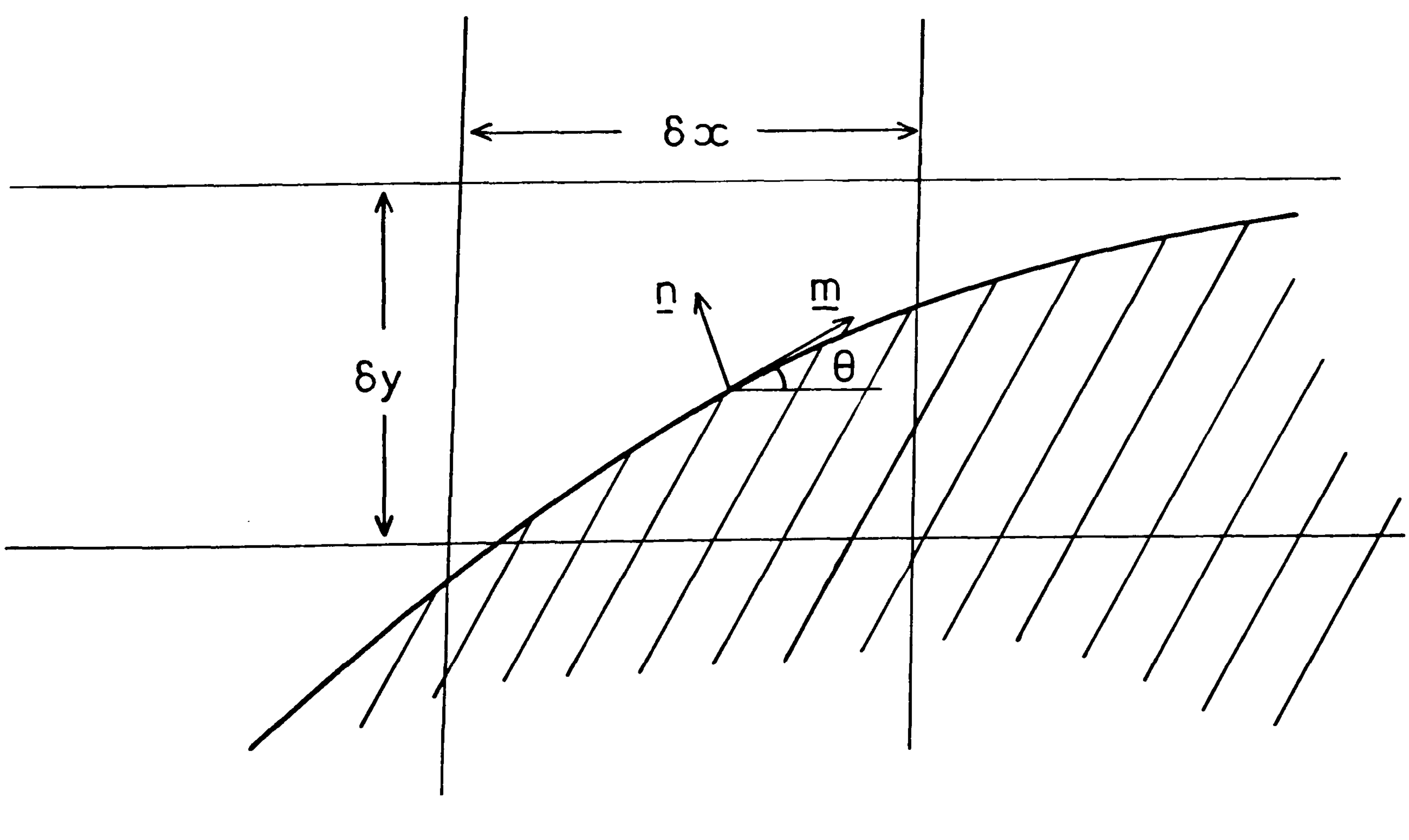

FIG. 7.6 ORIENTATION OF SURFACE IN A CORNER CELL

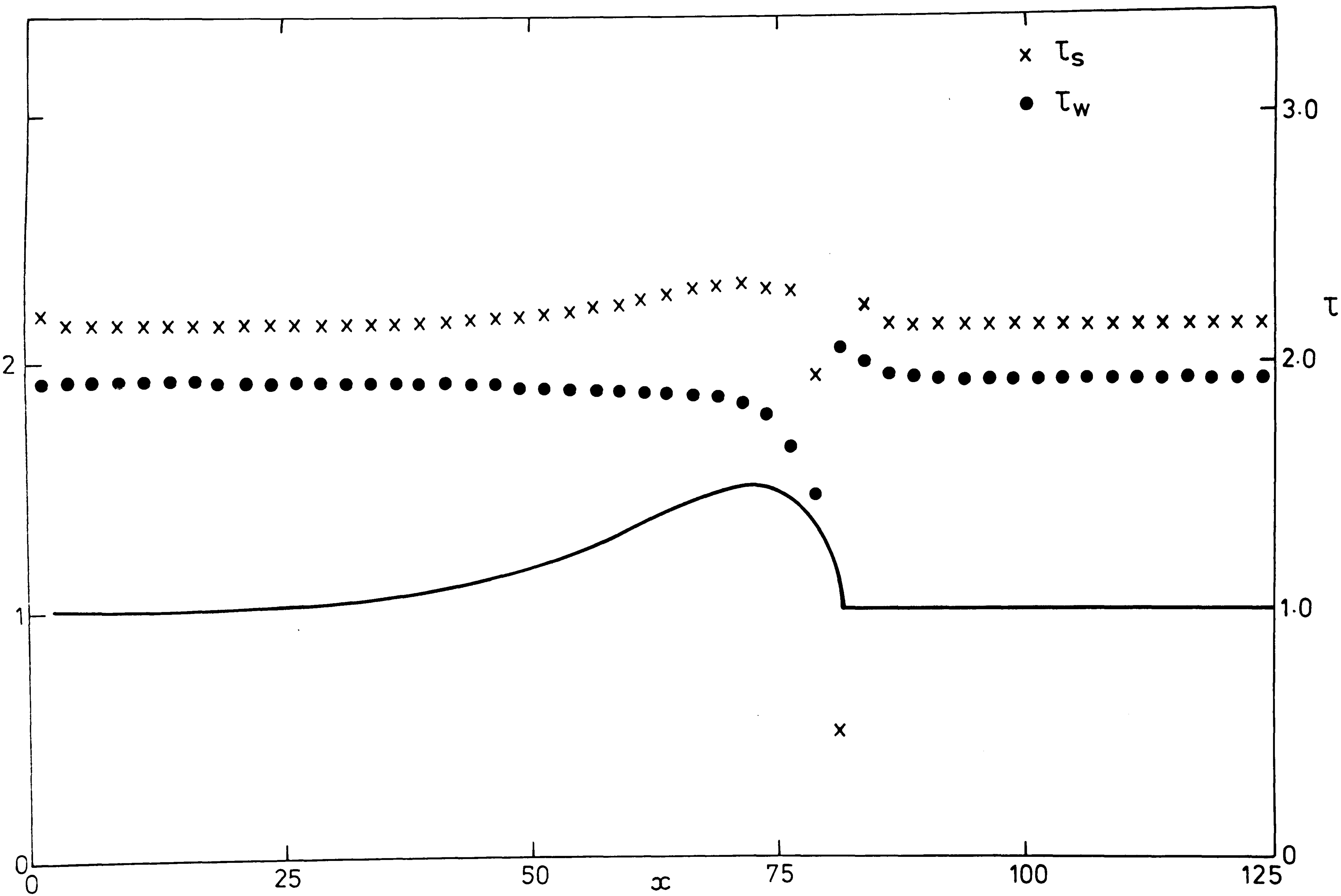

FIG. 7.7 POISSON WAVE $G_G = 63.4\ kgm^{-2}\ s^{-1}$, CONSTANT ROUGHNESS , AFTER 18 CYCLES (t=0.9)

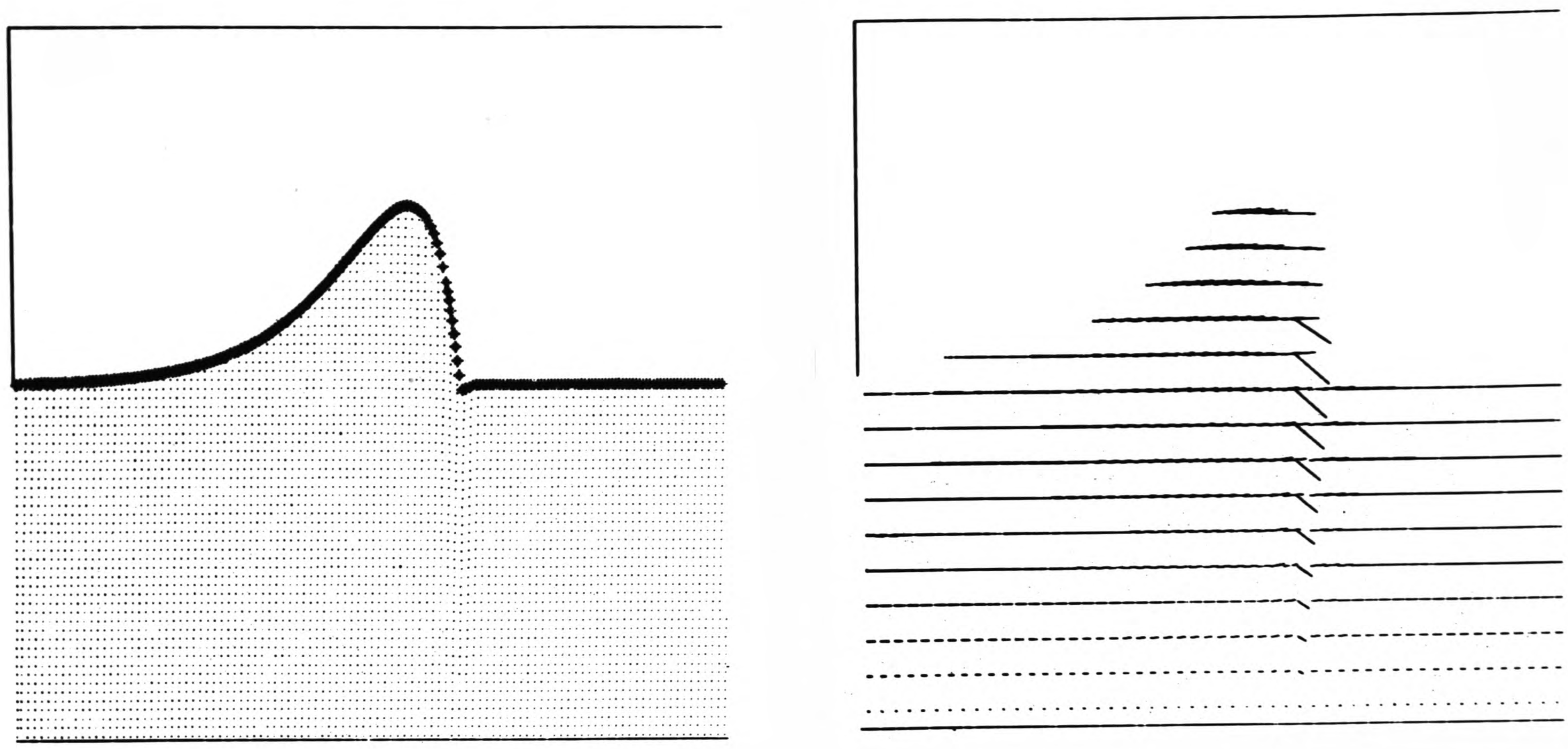

a, t = 0.9 Particle Plot

b, t = 0.9 Cell-Centred Velocity Plot

FIG. 7.8 SMAC PLOT - POISSON WAVE G_G = 63.4 $kgm^{-2}s^{-1}$ CONSTANT ROUGHNESS

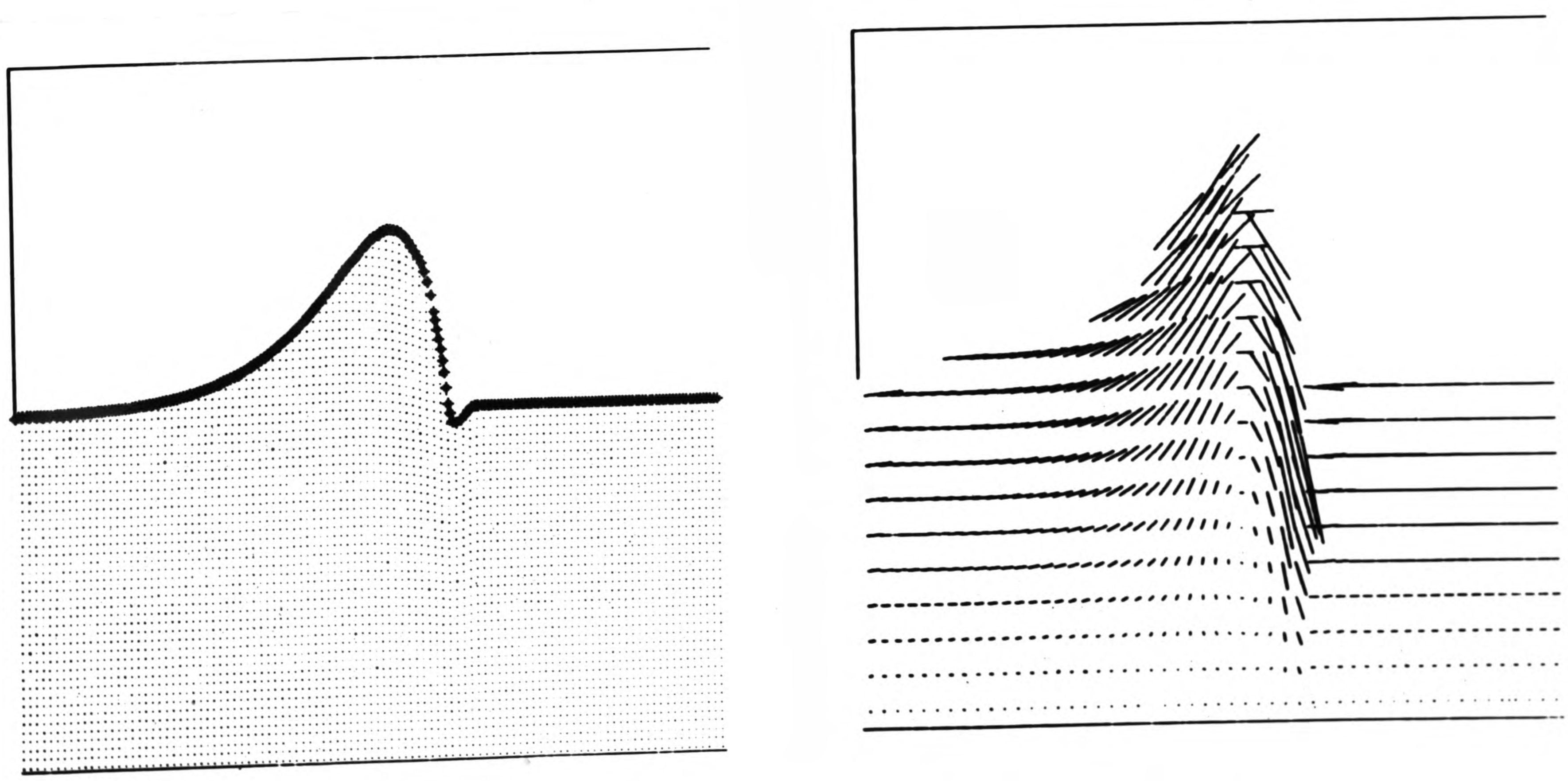

a, t = 0.2 Particle Plot

b, t = 0.2 Cell-Centred Velocity Plot

FIG. 7.9 SMAC PLOT - POISSON WAVE G_G = 31.7 $kgm^{-2}s^{-1}$ CONSTANT ROUGHNESS

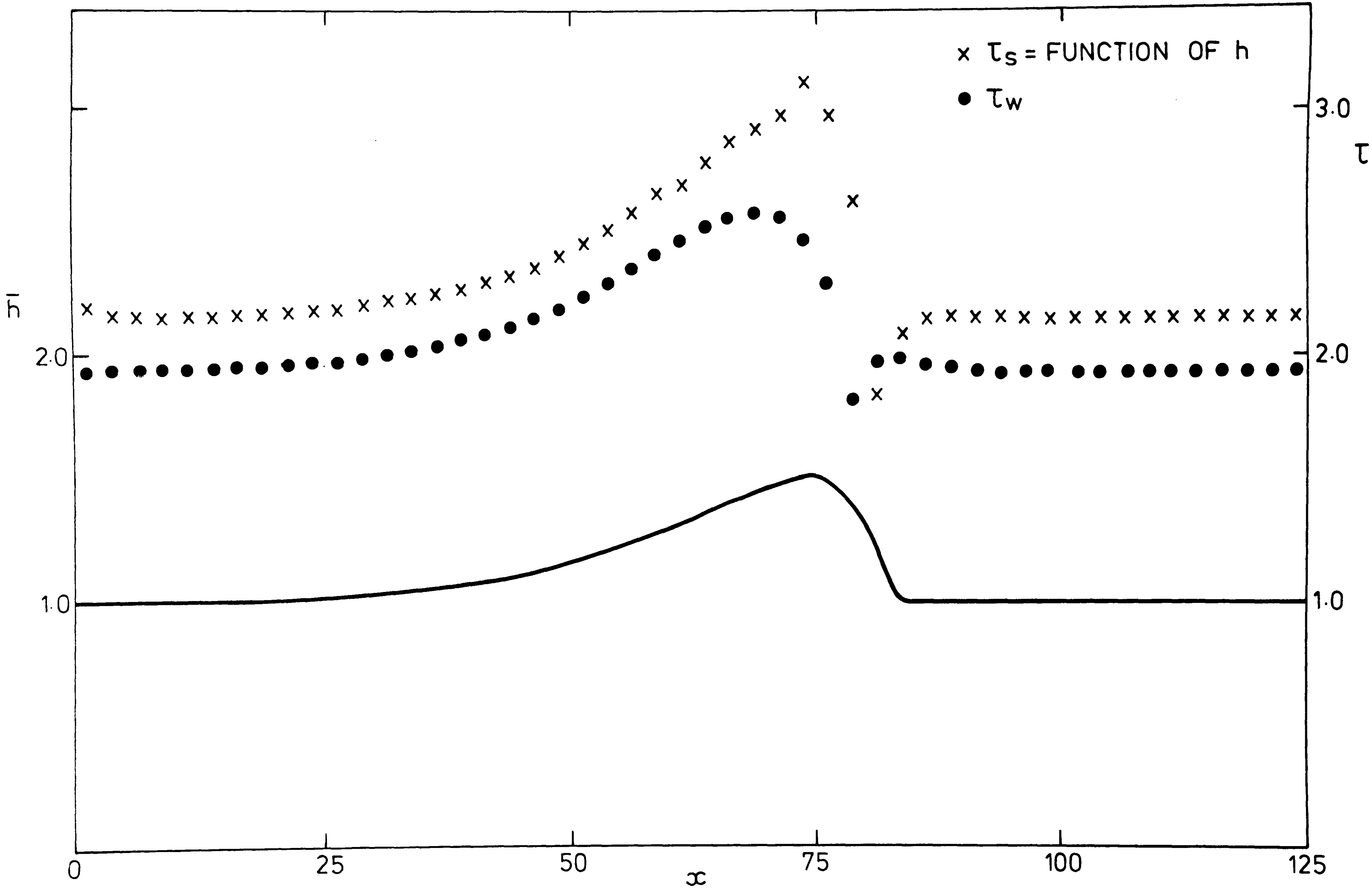

FIG. 7.10 POISSON WAVE $G_G = 63.4\,\mathrm{kg\,m^{-2}\,s^{-1}}$ AFTER 18 CYCLES ($t = 0.9$)

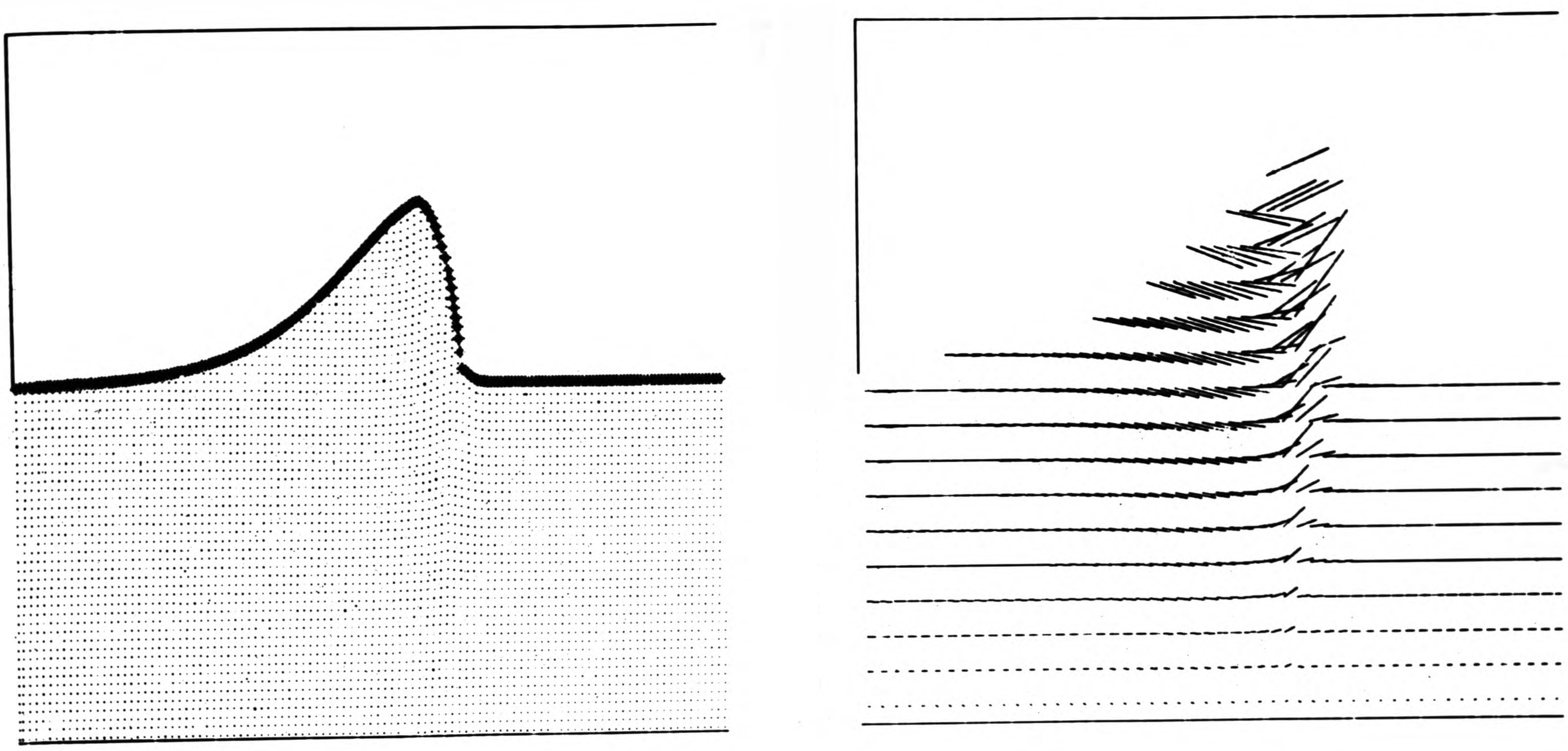

a,t = 0.9 Particle Plot

b,t = 0.9 Cell-Centred Velocity Vector Plot

FIG. 7.11 SMAC PLOT - POISSON WAVE G_G = 63.4 $kgm^{-2}s^{-1}$

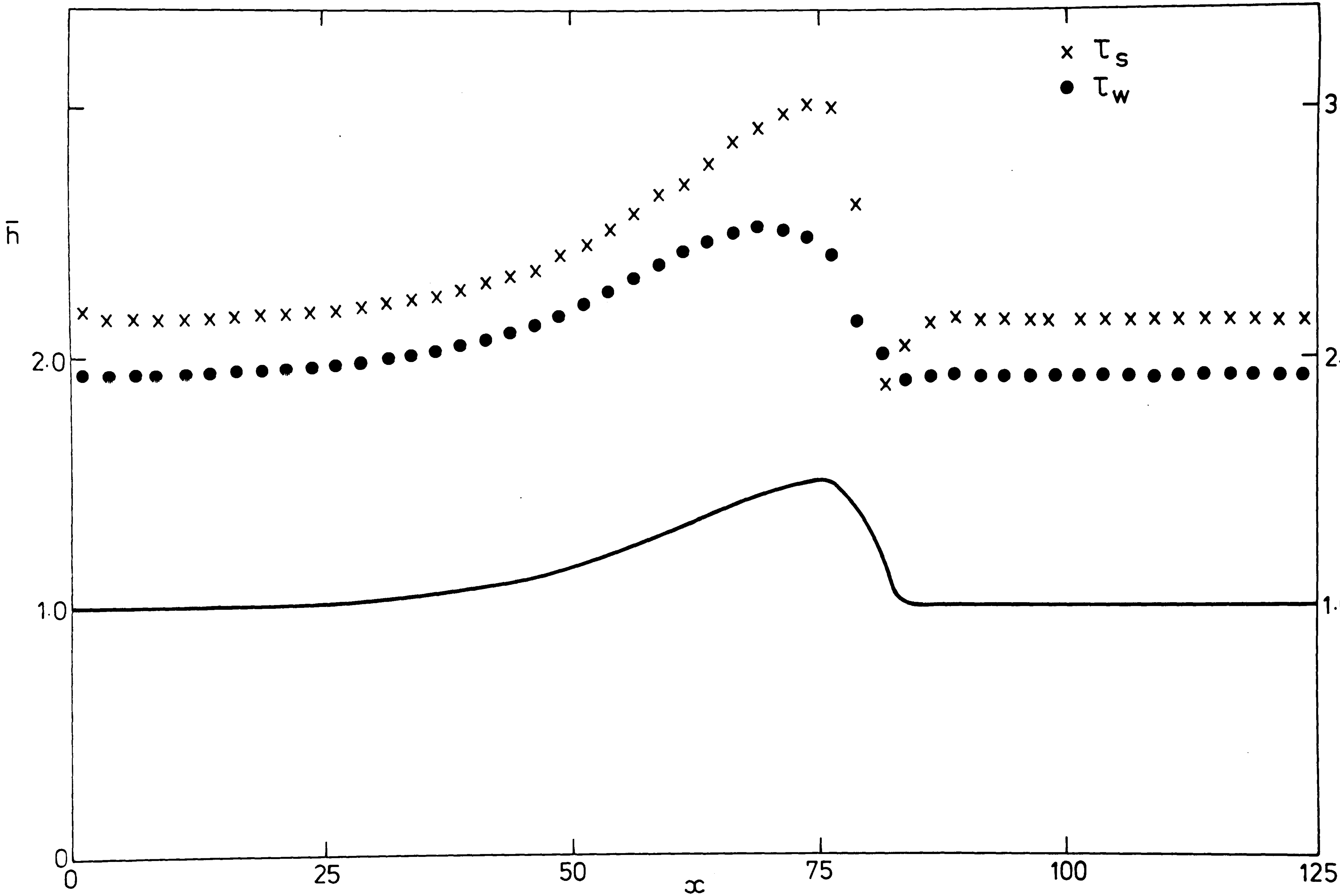

FIG. 7.12 POISSON WAVE $G_G = 63{\cdot}4\,kg\,m^{-2}\,s^{-1}$, AFTER 18 CYCLES ($t=0{\cdot}9$) - NO PRESSURE PERTURBATION.

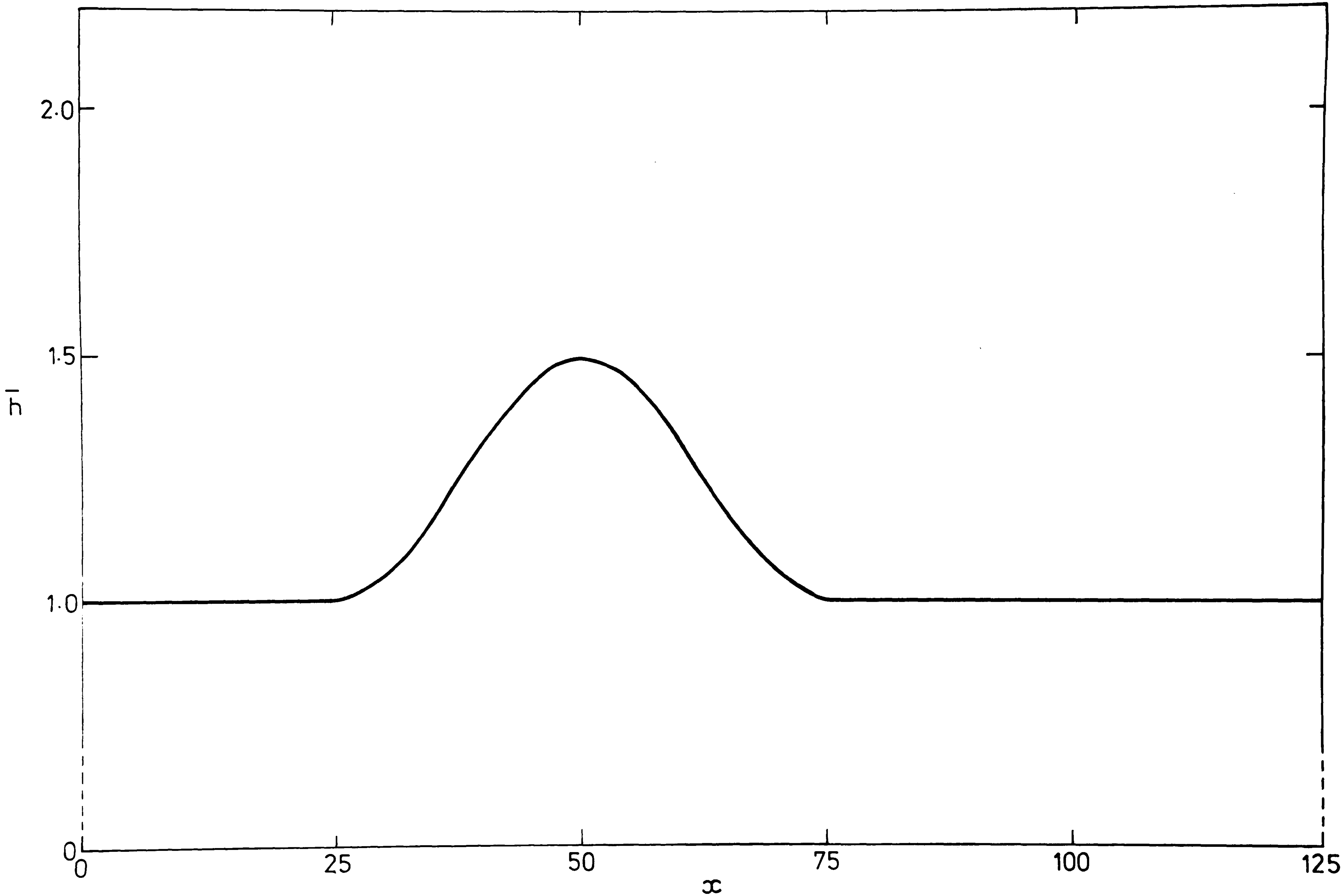

FIG. 7.13 COS WAVE $G_G = 63{\cdot}4\ kgm^{-2}s^{-1}$ a, t = 0

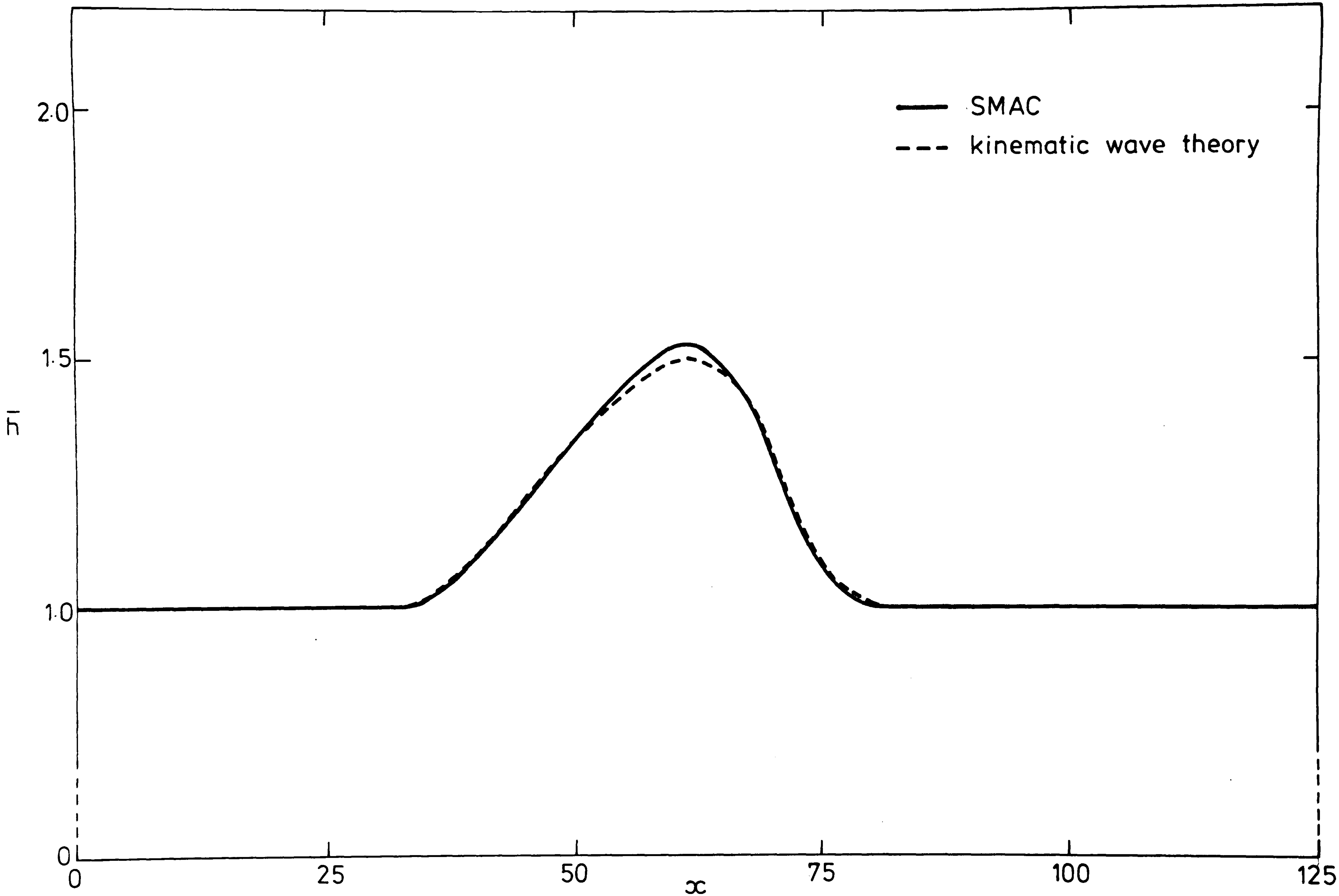

FIG. 7.13b , $t = 0.9$

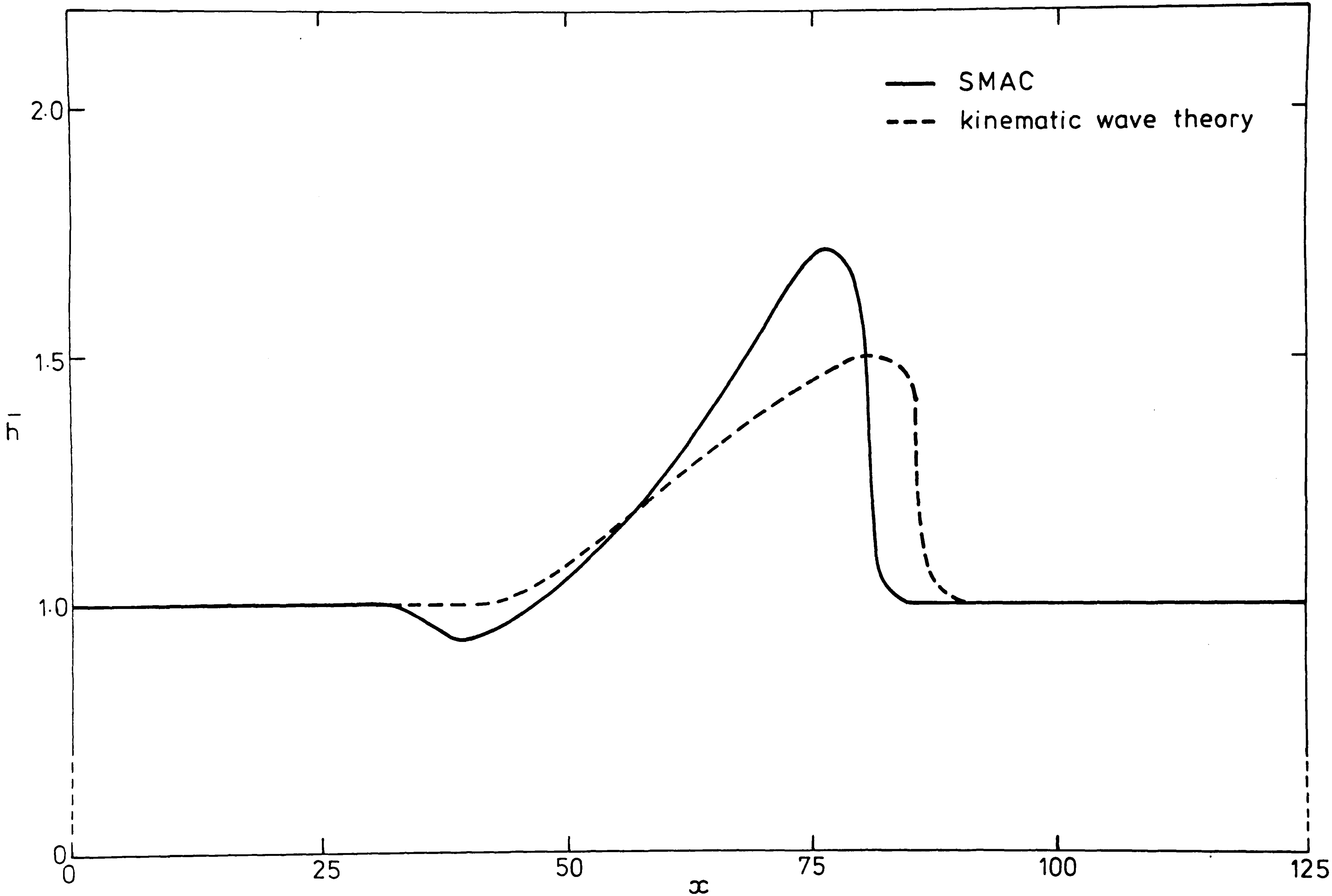

FIG. 7.13c, t = 2.35 - BREAKING

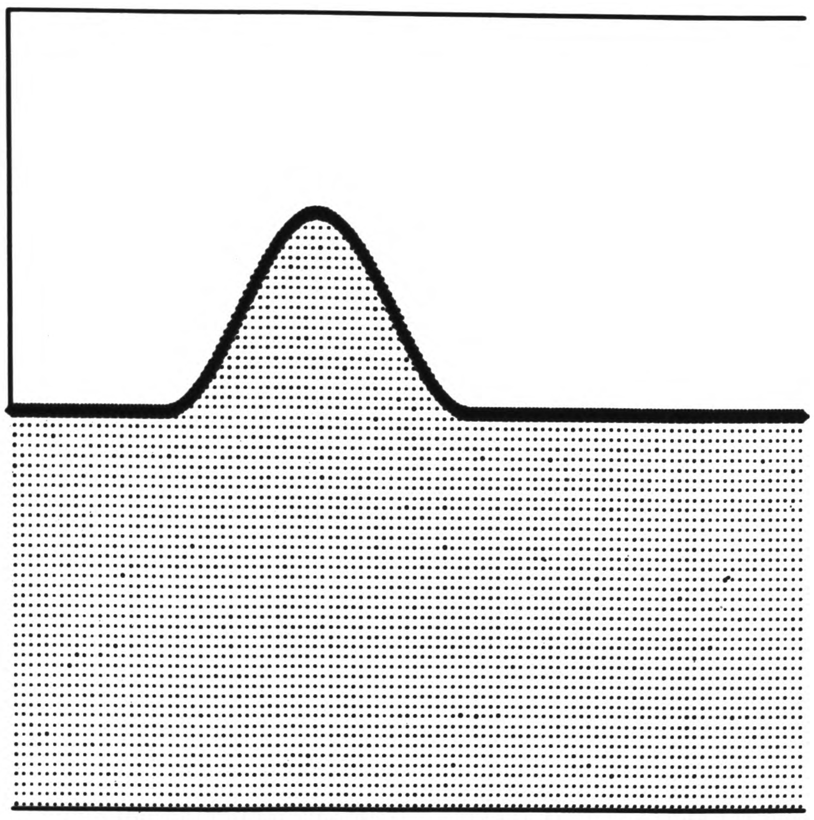

a,t = 0 Particle Plot

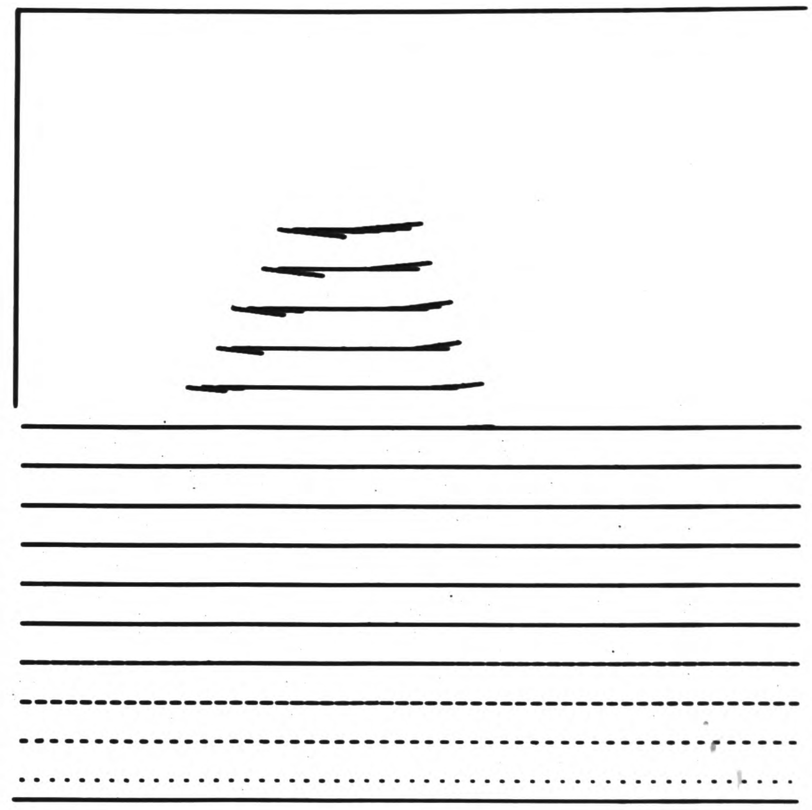

b,t = 0 Cell-Centred Velocity Plot

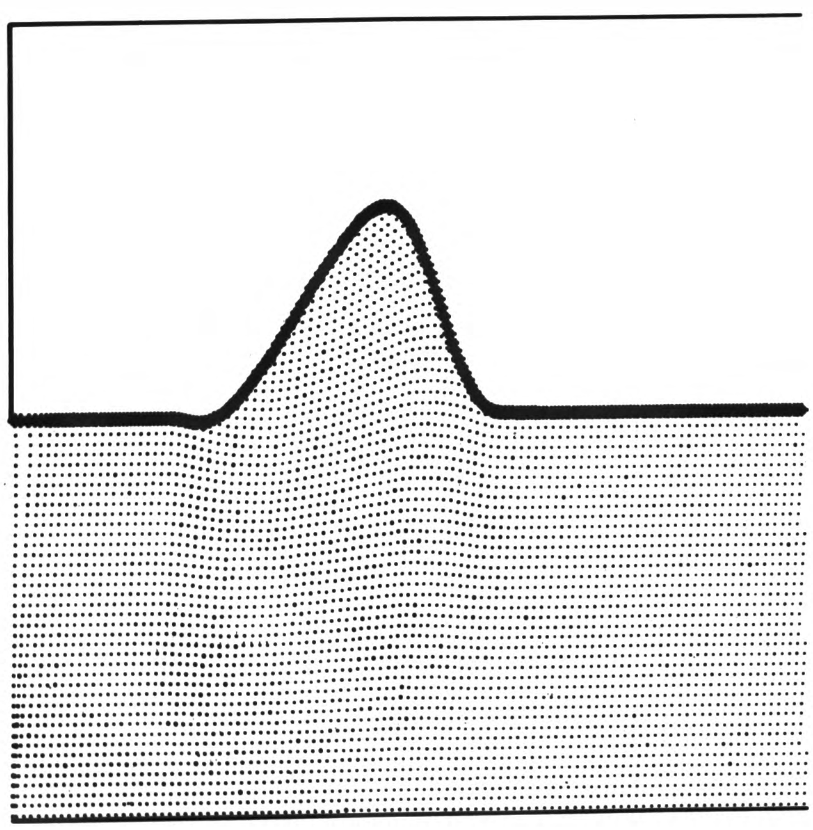

c,t = 0.9 Particle Plot

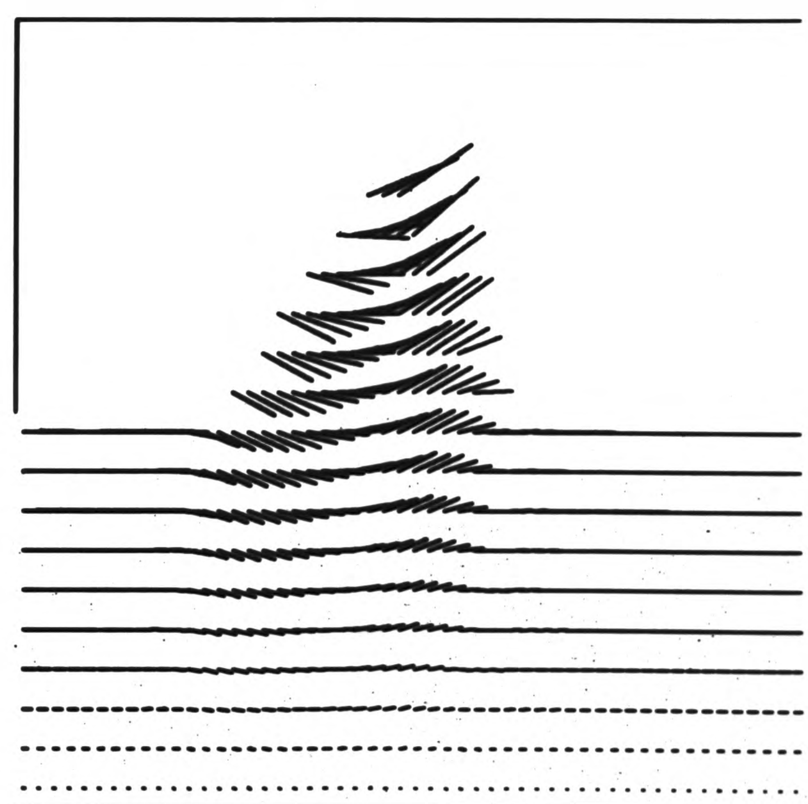

d,t = 0.9 Cell-Centred Velocity Vector Plot

FIG. 7.14 SMAC PLOT - COS WAVE $G_G = 63.4\ kgm^{-2}s^{-1}$

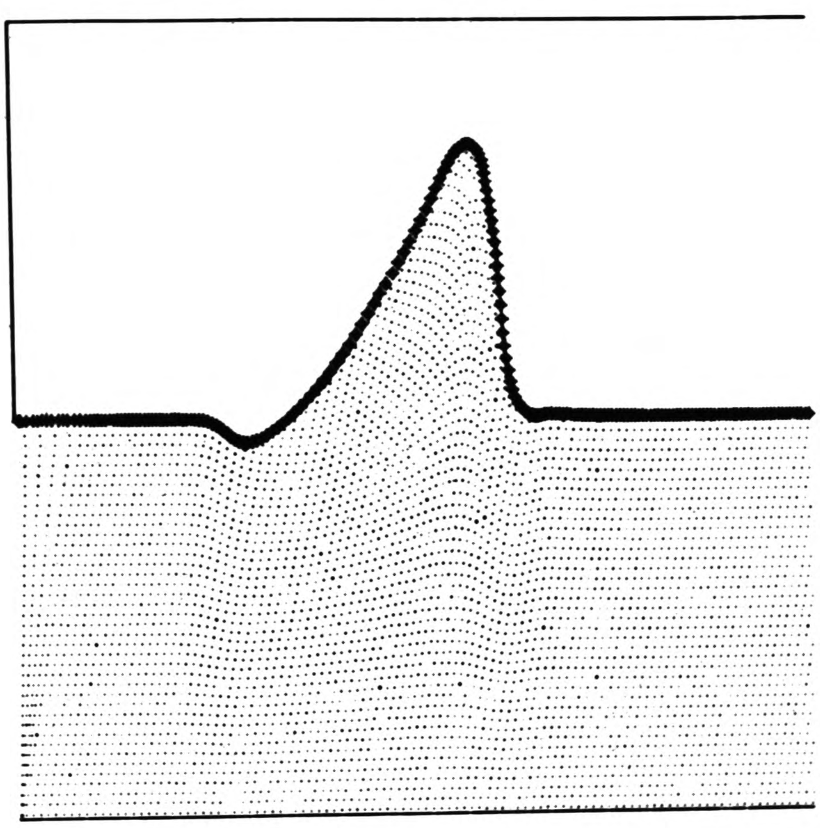

e,t = 2.35 Particle Plot

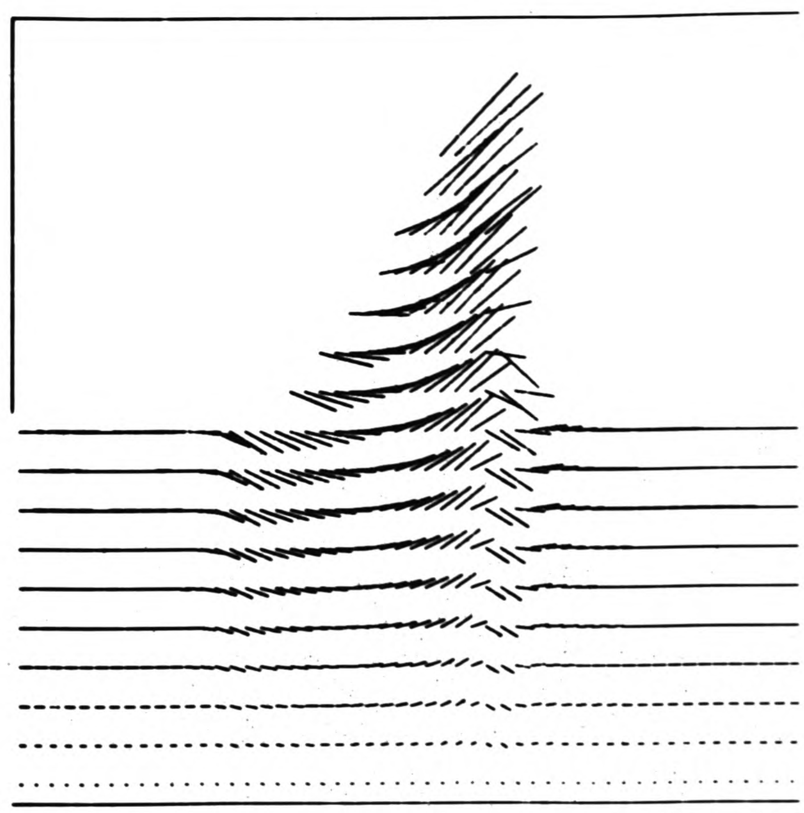

f,t = 2.35 Cell-Centred Velocity Vector Plot

FIG. 7.14 Cont.

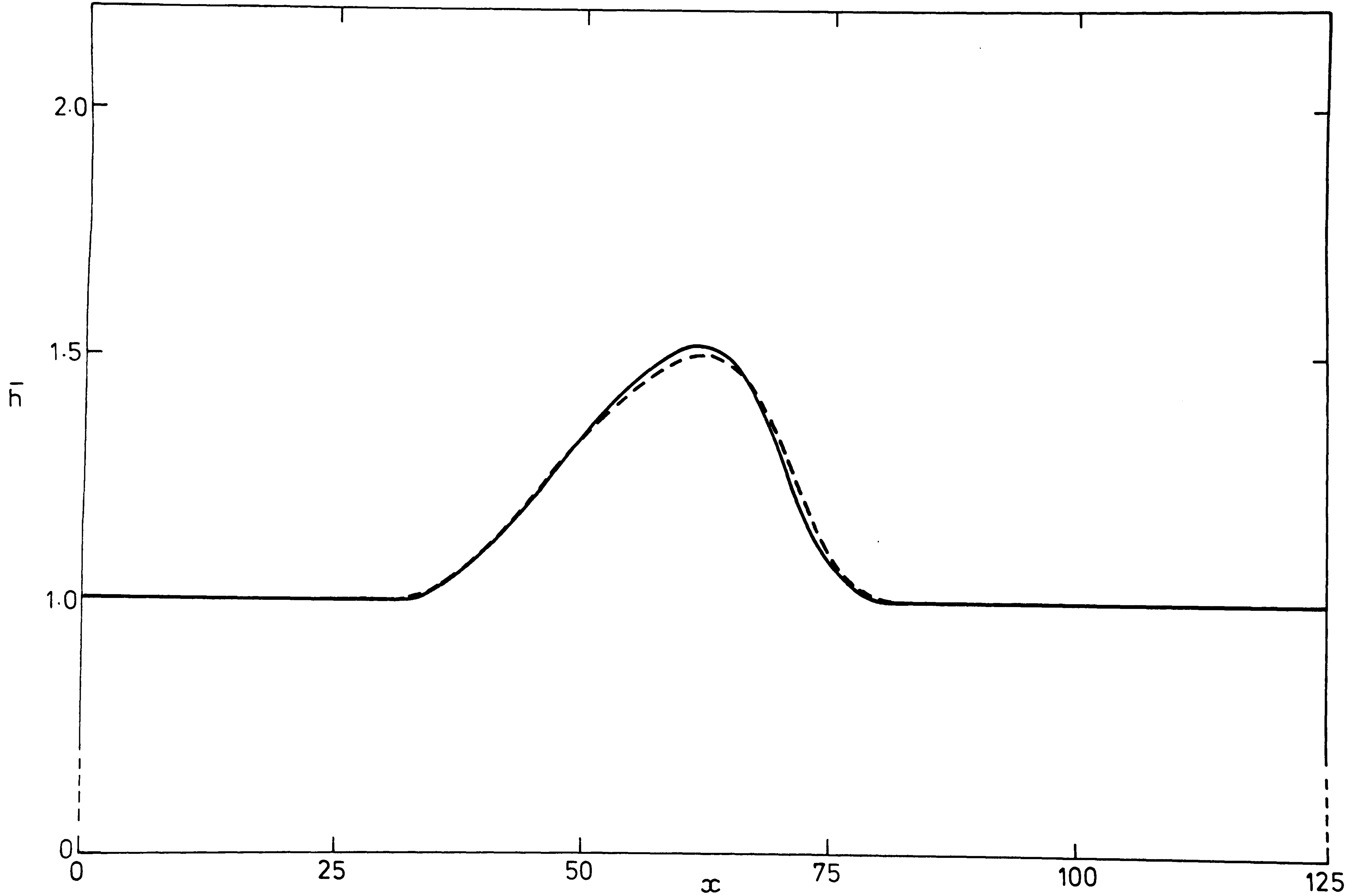

FIG. 7.15 COS WAVE $G_G = 63{\cdot}4\ \mathrm{kg\,m^{-2}\,s^{-1}}$ - NO PERTURBATION STRESSES a, $t = 0{\cdot}9$

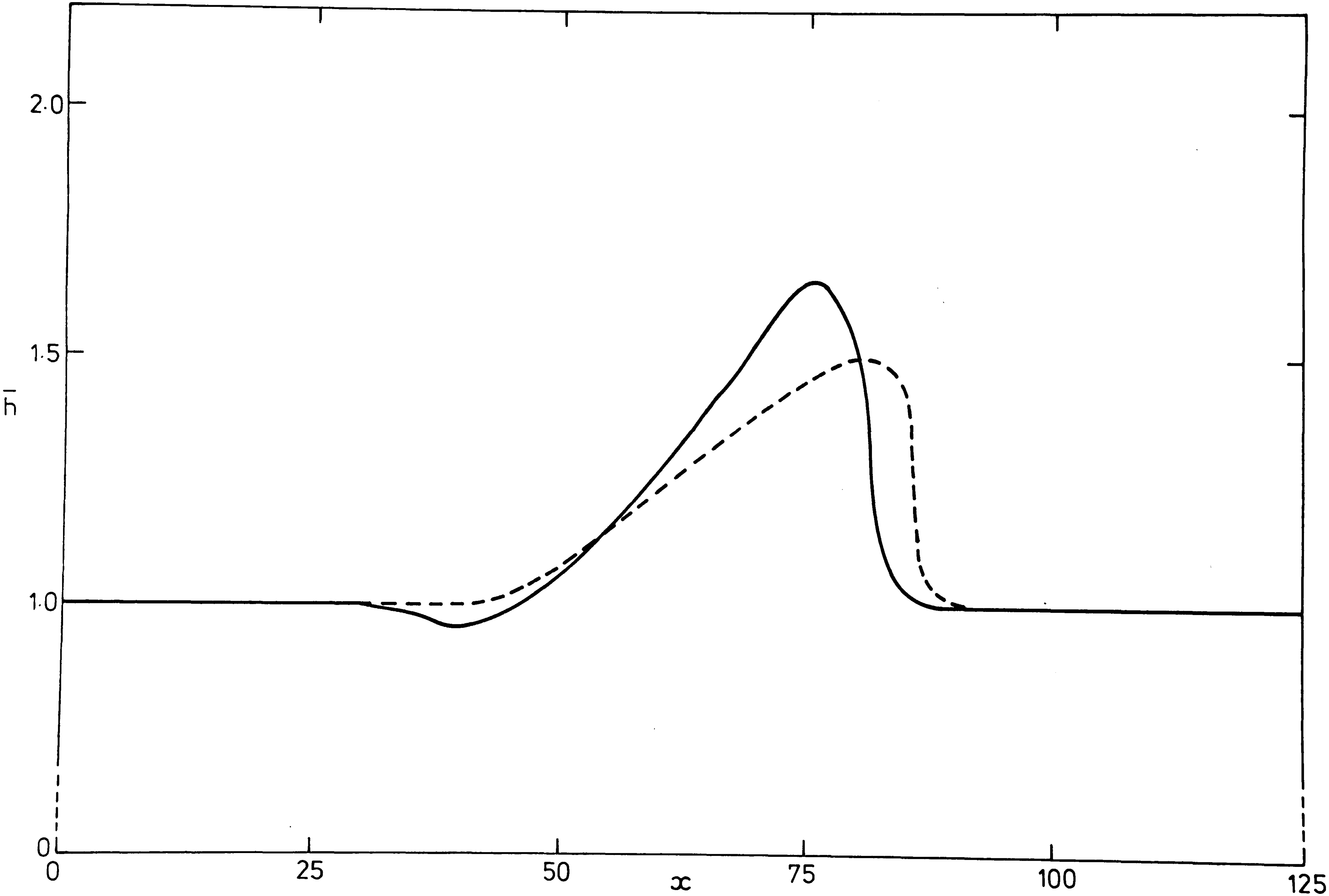

FIG. 7.15 b , $t = 2.35$